On electronic signatures of topological superconductivity

Proefschrift

ter verkrijging van
de graad van Doctor aan de Universiteit Leiden,
op gezag van Rector Magnificus prof. mr. C.J.J.M. Stolker,
volgens besluit van het College voor Promoties
te verdedigen op dinsdag 8 september 2015
klokke 16.15 uur

door

Mathias Diez

geboren te Karlsruhe, Duitsland in 1985

Promotiecommissie

Promotor: Prof. dr. C. W. J. Beenakker
Overige leden: Dr. A. R. Akhmerov (Technische Universiteit Delft)
Dr. V. Cheianov
Prof. dr. E. R. Eliel
Prof. dr. K. E. Schalm

Casimir PhD Series Delft-Leiden 2015-17
ISBN 978-90-8593-225-3

Dit werk maakt deel uit van het onderzoekprogramma van de Stichting voor Fundamenteel Onderzoek der Materie (FOM), die deel uit maakt van de Nederlandse Organisatie voor Wetenschappelijk Onderzoek (NWO).

This work is part of the research programme of the Foundation for Fundamental Research on Matter (FOM), which is part of the Netherlands Organisation for Scientific Research (NWO).

Cover: *Front: Two shells of different species of sea shell indicate chirality. In a topological superconducting nanowire chiral symmetry can protect multiple Majorana bound states. Each adds* $2e^2/h$ *to the Andreev conductance. The swap of electrons (blue) and holes (red) in the two chains hints at the nature of the chiral symmetry; see chapter 3. Back: The butterfly is decorated with the Hall conductance of graphene's moiré superlattice; compare with Fig. 6.3. It is characterized by a series of cloned Dirac cones which can be tuned massless; see chapter 6.*

To my brother.

Contents

Chapter 1

Introduction

1.1 Preface

The characteristic feature of topological insulators and superconductors is the coexistence of a gapped bulk with gapless boundary modes. The gap has a different origin for topological insulators and topological superconductors. Topological insulators have a finite mobility gap that makes them insulators for electrical currents. Their edge or surface states are metallic with a high conductivity, making it relatively easy to detect them by electrical measurements. Topological superconductors, in contrast, are perfect electrical conductors but insulators for thermal currents. Their edge or surface states then allow for heat transport, without any transport of electrical charge. It is difficult to measure the thermal conductance at low temperatures, while at higher temperatures the boundary contribution is obscured by the contribution from phonons. This makes it desirable to search for electrical probes of boundary modes in a superconductor. In this thesis we propose and study such electrical signatures of topological superconductivity.

Key to this issue are two ingredients: symmetries and dimensionality. Of particular interest in this thesis is a type of discrete symmetry, known as *chiral* symmetry. In superconductors it appears as the combination of particle-hole and time-reversal symmetry. Chiral symmetry is a unitary symmetry, like rotation or translation, but unlike these conventional unitary symmetries the chiral symmetry operator is *anti*-commuting, instead of commuting, with the Hamiltonian. This means that the effect of a chiral symmetry cannot be removed by working in a basis where the Hamiltonian is block-diagonal. A chiral symmetry can produce topologically protected surface modes when the spatial dimensionality of the system is odd, in particular, this plays a role in a one-dimensional wire geometry.

In some physical systems the symmetries are broken locally, but restored in an average sense on long length scales. One then enters the field of *statistical* topological insulators or superconductors, which is a major extension of the socalled tenfold way classification of topological states of matter.

This introductory chapter introduces the concepts that will play a central role in chapters 2–5. Chapters 6 and 7 take a different direction, motivated by recent experimental advances in two fields, Van der Waals heterostructures of graphene and complex oxide interfaces.

1.2 Classification of topological states of matter

1.2.1 The “tenfold way”

Depending on symmetries and dimensionality, topological insulators and topological superconductors can be classified in a scheme known as the *“tenfold way”* [7].

Different gapped phases are distinguished by different values of the topological quantum number Q. This is a momentum-space integral over the Brillouin zone of the Hamiltonian $H(\boldsymbol{k})$. It can be an integer $Q \in \mathbb{Z}$ ($Q = \ldots, -2-1, 0, 1, 2, \ldots$) or a parity index $Q \in \mathbb{Z}_2$ ($Q = 0, 1$). A phase is called topologically *non-trivial* when $Q \neq 0$, while the $Q = 0$ state is called topologically trivial.

The number Q is a bulk invariant, because it cannot be changed without closing the bulk gap — the band gap or mobility gap in the case of insulators and the superconducting gap in the case of superconductors. This robustness to smooth deformations is referred to as “topological protection”.

The insensitivity of the bulk invariant against perturbations that do not close the gap immediately implies the presence of gapless boundary modes, simply because the bulk gap must close along the path from the non-trivial bulk to the trivial vacuum state. Moreover, since we are allowed to decrease $|Q|$ in steps of one unit, each step being accompanied by a gap closing, there must be exactly $|Q|$ topologically protected edge modes between the bulk with $Q \neq 0$ and the vacuum with $Q = 0$.

This counting rule $|\textit{bulk invariant}| = \#\textit{edge modes}$ is known as the bulk-boundary correspondence.

To know which values of Q are allowed, we need to identify the fundamental symmetries of the system.

According to Wigner's theorem, in order to preserve probabilities the symmetry operations in quantum mechanics are represented by unitary or anti-unitary transformations of Hilbert space. A unitary U preserves the inner product of two states $|\Psi\rangle$, $|\Phi\rangle$, while an anti-unitary A adds an additional complex conjugation:

$$\langle U\Psi,\, U\Phi\rangle = \langle \Psi,\, \Phi\rangle, \tag{1.1}$$

$$\langle A\Psi,\, A\Phi\rangle = \langle \Psi,\, \Phi\rangle^* = \langle \Phi,\, \Psi\rangle. \tag{1.2}$$

Each symmetry operation can commute or anti-commute with the Hamiltonian H.

An anti-unitary symmetry that commutes with H is called time-reversal symmetry, $\mathcal{T}H = H\mathcal{T}$, while an anti-unitary symmetry that anti-commutes with H is called particle-hole symmetry, $\mathcal{P}H = -H\mathcal{P}$. Wigner's theorem also states that the square of a anti-unitary symmetry equals +1 or −1.

Unitary symmetries that commute with the Hamiltonian, $HU = UH$, can be removed by block-diagonalization, followed by a restriction to a subspace in which U acts as a scalar. This is not possible for unitary symmetries that anti-commute with the Hamiltonian, $\Gamma H = -H\Gamma$. To construct such a chiral symmetry we take the product $\mathcal{PT}$ of particle-hole and time-reversal symmetry, which is a unitary symmetry (being the product of two anti-unitary symmetries) and anti-commutes with the Hamiltonian: $\mathcal{PT}H = \mathcal{P}H\mathcal{T} = -H\mathcal{PT}$.

There is a total of ten ways to combine $\mathcal{T}, \mathcal{P}, \Gamma$, distinguishing $\mathcal{T}^2, \mathcal{P}^2 = \pm 1$, hence the name "tenfold way". In the following we discuss the fundamental symmetries, time-reversal and particle-hole symmetry, in a bit more detail. Because it has a special role and an interesting origin, we dedicate a separate section to chiral symmetry at the end of this chapter.

1.2.2 Time-reversal symmetry

The physical operation of time-reversal causes a reversal of both momentum $\mathcal{T}\boldsymbol{p}\mathcal{T}^{-1} = -\boldsymbol{p}$ and spin (angular momentum) $\mathcal{T}\sigma_i\mathcal{T}^{-1} = -\sigma_i$. The operator that does this is $\mathcal{T} = i\sigma_y\mathcal{K}$, where the spin reversal is expressed by the Pauli-matrix σ_y and $\mathcal{K}$ denotes complex conjugation. [1] This is an anti-unitary operator that squares to -1. For spinless particles, or if H is spin-independent, $\mathcal{T} = \mathcal{K}$ would suffice and $\mathcal{T}$ would square to $+1$.

The eigenvalues of a spin-independent Hamiltonian have a twofold spin-degeneracy, for a trivial reason. One might think that introducing a spin dependence would split the degeneracy, however, this is forbidden by Kramers' theorem if time-reversal symmetry remains unbroken. This so-called Kramers degeneracy appears because each eigenstate Ψ comes with a partner $\mathcal{T}\Psi$ at the same energy E, but orthogonal to Ψ when $\mathcal{T}^2 = -1$.

1.2.3 Particle-hole symmetry

Particle-hole symmetry appears in the context of superconducting systems described by a mean-field Bogoliubov-De Gennes (BdG-) Hamiltonian [19, 44]. It is a consequence of the fermionic exchange statistics and applies to all quadratic (or mean-field) Hamiltonians of the form

$$\mathcal{H} = \sum_{ij} H_{ij} c_i^\dagger c_j + \frac{1}{2} \sum_{ij} \left(\Delta_{ij} c_i^\dagger c_j^\dagger + \Delta_{ij}^* c_i c_j \right). \tag{1.4}$$

The operators $c_i^\dagger$, c_i denote the creation and annihilation of an electron in second quantization. The index i includes spin and spatial degrees of freedom. The anti-commutation relations $\{c_i, c_j\} = \{c_i^\dagger, c_j^\dagger\} = 0$ and $\{c_i, c_j^\dagger\} = \delta_{ij}$ imply that the single-particle Hamiltonian H is Hermitian, while the pair potential Δ is anti-symmetric.

It is convenient to write Eq. (1.4) in matrix form,

$$\mathcal{H} = \frac{1}{2} \hat{C}^\dagger H_{\text{BdG}} \hat{C}, \tag{1.5}$$

where

$$\hat{C} = (c_1, \ldots, c_N, c_1^\dagger, \ldots, c_N^\dagger), \tag{1.6}$$

$$H_{\text{BdG}} = \begin{pmatrix} H_0 & \Delta \\ -\Delta^* & -H_0^* \end{pmatrix}. \tag{1.7}$$

---

[1] Throughout this thesis we will denote the spin-degree of freedom using the Pauli-matrices

$$\sigma_x = \begin{pmatrix} 0 & 1 \\ 1 & 0 \end{pmatrix}, \sigma_y = \begin{pmatrix} 0 & -i \\ i & 0 \end{pmatrix}, \sigma_z = \begin{pmatrix} 1 & 0 \\ 0 & -1 \end{pmatrix} \tag{1.3}$$

and the corresponding matrices τ_x, τ_y, and τ_z for the particle-hole degree of freedom.

class	$\mathcal{T}^2$	$\mathcal{P}^2$	Γ	$d=1$	$d=2$	$d=3$
C	✗	-1	✗	✗	$\mathbb{Z}$	✗
D	✗	$+1$	✗	$\mathbb{Z}_2$	$\mathbb{Z}$	✗
DIII	-1	$+1$	✓	$\mathbb{Z}_2$	$\mathbb{Z}_2$	$\mathbb{Z}$
BDI	$+1$	$+1$	✓	$\mathbb{Z}$	✗	✗

Table 1.1. Classification of topological superconductors according to the tenfold-way. Each symmetry class is characterized by the square (± 1) or absence (✗) of time-reversal $\mathcal{T}$ and particle-hole symmetry $\mathcal{P}$, and the presence (✓) or absence (✗) of a chiral symmetry Γ. Depending on the dimension d superconducting phases in each class are either trivial (✗), or characterized by $\mathbb{Z}_2$ or $\mathbb{Z}$ topological invariant.

In first quantization, the operator H_{BdG} governs the dynamics of the excitations above the superconducting ground state via the Bogoliubov-De Gennes equation

$$H_{\mathrm{BdG}}\Psi(\boldsymbol{r},t) = i\hbar\frac{\partial}{\partial t}\Psi(\boldsymbol{r},t), \tag{1.8}$$

$$\Psi = (\psi_e,\, \psi_h). \tag{1.9}$$

The wave function Ψ describes excitations known as Bogoliubov quasi-particles, formed out of coherent superpositions of electrons (e) and holes (h).

By construction the BdG-Hamiltonian H_{BdG} obeys the particle-hole symmetry

$$H = -\mathcal{P}H\mathcal{P}^{-1} = -\tau_x H^* \tau_x, \tag{1.10}$$

where the Pauli matrix τ_x swaps $\psi_e \leftrightarrow \psi_h$. Each eigenfunction Ψ of H at energy E has a copy $\tau_x\Psi$ at energy $-E$.

The anti-unitary operator $\mathcal{P} = \tau_x\mathcal{K}$ squares to $+1$. In the case of a spin-independent H, it is possible to construct an alternative particle-hole symmetry operator that squares to -1.

1.3 Topological superconductors

Topological superconductors are the non-trivial phases of superconductors described by a mean-field BdG-Hamiltonian of the form (1.7) that obey a particle-hole symmetry $\mathcal{P}$. This symmetry allows for exotic quasi-particle excitations (Majorana modes) that are unique to topological superconductors.

Table 1.1 shows a rich set of possible non-trivial phases in one, two, and three dimensions. So we might expect a large variety of topological superconductors in Nature or at least in the lab. Unfortunately, most commonly occurring superconductors are spin-singlet superconductors, obey time-reversal symmetry, and have negligible spin-orbit interactions, which makes them topologically trivial. One candidate material with spin-triplet pairing is strontium ruthenate [83, 100].

An alternative and promising route is to use the superconducting proximity effect to induce spin-triplet pairing in a semiconductor with strong spin-orbit coupling. Such hybrid systems include semiconductor nanowires [98, 117, 109, 47, 43], Shiba bound states in magnetic atoms [39, 110, 111], or topological insulators [61, 62] — all with induced spin-triplet superconductivity by proximity to a conventional spin-singlet superconductor.

1.3.1 Chiral *p*-wave superconductor

A spin-triplet superconductor with two-dimensional $p_x \pm ip_y$ orbital symmetry is called a chiral p-wave superconductor [177, 130]. It's mean-field BdG-Hamiltonian reads

$$H_{p-\text{wave}} = \left(\frac{\boldsymbol{p}^2}{2m_{\text{eff}}} - \mu\right)\tau_z + \Delta_0(p_x\tau_x - p_y\tau_y.) \tag{1.11}$$

The Pauli matrices $\tau_{0,x,y,z}$ (0 for the identity) act on the particle-hole degree of freedom. The normal part is a parabolic dispersion with momentum $\boldsymbol{p} = -i\partial_{\boldsymbol{r}}$, effective mass m_{eff} and chemical potential μ. The pair potential Δ_0 pairs electrons of opposite momenta, but equal spin. In the simplest case we may ignore the spin (or more precisely only consider the spin band closest to the Fermi level). For a given Fermi momentum p_F (set by the chemical potential μ for $\Delta_0 = 0$) the pair potential has a fixed amplitude $\Delta_0 p_F$, while its phase $\phi = \arctan(p_y/p_x)$ winds by 2π following the angle of the in-plane momentum.

The Hamiltonian (1.11) anti-commutes with the particle-hole symmetry operator $\mathcal{P} = \tau_x\mathcal{K}$, which squares to $+1$ and places the chiral p-wave superconductor in symmetry class D of the tenfold way. More general

Hamiltonians in this symmetry class have the form

$$H(\boldsymbol{k}) = h_x(\boldsymbol{k})\tau_x + h_y(\boldsymbol{k})\tau_y + h_z(\boldsymbol{k})\tau_z, \tag{1.12}$$

with $\boldsymbol{p} = \hbar\boldsymbol{k}$. Particle-hole symmetry excludes a term $\propto \tau_0$ and requires

$$h_{x,y}(-\boldsymbol{k}) = -h_{x,y}(\boldsymbol{k}), \quad h_z(-\boldsymbol{k}) = h_z(\boldsymbol{k}). \tag{1.13}$$

We can define the normalized Bloch vector $\hat{h}(\boldsymbol{k}) = \boldsymbol{h}(\boldsymbol{k})/|\boldsymbol{h}(\boldsymbol{k})|$, where $\boldsymbol{h} = (h_x, h_y, h_z)$. The $\mathbb{Z}$-topological invariant n is the Chern number

$$n = \frac{1}{4\pi}\int d^2k\, (\partial_{k_x}\hat{h} \times \partial_{k_y}\hat{h}) \cdot \hat{h}. \tag{1.14}$$

Returning to the model Hamiltonian (1.11), we find two topologically distinct phases. For $\mu < 0$ the Bloch vector only visits the south pole while for $\mu > 0$ it visits both the north and south pole covering a full solid angle on the Bloch sphere. The first phase is topologically trivial (we can tune Δ_0 to zero without closing the gap). The second is topologically non-trivial so we expect to see gapless edge modes.

1.3.2 Majorana edge modes

The simplest possible case where we expect to see such topological edge modes is a domain wall $\mu = -\mu_0$ for $y < 0$ and $\mu = \mu_0$ for $y > 0$. All eigenstates of the Bogoliubov-De Gennes equation (1.8) are then plane waves in the x-direction. To find the edge modes, we need to solve the corresponding eigenvalue problem in real space ($\hbar = 1$):

$$\begin{pmatrix} -\mu(y) & -i\Delta_0(\partial_y - k_x) \\ -i\Delta_0(\partial_y + k_x) & \mu(y) \end{pmatrix} \cdot \begin{pmatrix} \phi_e(y) \\ \phi_h(y) \end{pmatrix} = E \begin{pmatrix} \phi_e(y) \\ \phi_h(y) \end{pmatrix}, \tag{1.15}$$

where

$$\Psi(\boldsymbol{r}, t) = \begin{pmatrix} \phi_e(y) \\ \phi_h(y) \end{pmatrix} e^{i(k_x x - Et)}. \tag{1.16}$$

We choose $\Delta_0 > 0$ and for simplicity are focusing on small momenta $p^2/2m_{\text{eff}} \ll |\mu|$ so that we can ignore the p^2 term. Sorting terms dependent and independent of y we find

$$\begin{aligned} E\phi_e - i\Delta_0 k_x \phi_h &= -\mu(y)\phi_e - i\Delta_0 \frac{\partial \phi_h}{\partial y}, \\ E\phi_h + i\Delta_0 k_x \phi_e &= \mu(y) - i\Delta_0 \frac{\partial \phi_e}{\partial y}. \end{aligned} \tag{1.17}$$

This set of first order equations can be decoupled using the ansatz $\phi_h = \pm i\phi_e$

$$\begin{aligned}(E \pm \Delta_0 k_x)\phi_e &= -\mu(y)\phi_e \pm \Delta_0 \frac{\partial \phi_e}{\partial y},\\ (E \pm \Delta_0 k_x)\phi_h &= \mu(y)\phi_h \mp \Delta_0 \frac{\partial \phi_h}{\partial y}.\end{aligned} \tag{1.18}$$

Both can be solved by

$$E = \mp\Delta_0 k_x \quad \text{and} \quad \Psi \propto \begin{pmatrix} e^{\mp i\pi/4} \\ e^{\pm i\pi/4} \end{pmatrix} e^{\pm \frac{\mu_0}{\Delta_0}|y|} e^{i(k_x x - Et)}. \tag{1.19}$$

Notice that depending on the sign of μ_0 only one of the two solutions is normalizable. At positive energies and for $\mu_0 > 0$ ($y > 0$ non-trivial) we only get a right-moving mode $k_x > 0$, while for $\mu_0 < 0$ ($y < 0$ non-trivial) we only find a left-moving mode. In other words the edge mode is unidirectional or chiral (because it circulates the edge of a topological phase with a fixed handedness). Right or left moving, in both cases the edge mode is a coherent superposition of electron and hole with equal weight. We have chosen the overall phase factor of Ψ such that we have $\phi_h = \phi_e^*$. This means that the corresponding edge-mode field

$$\hat{\Psi}(\boldsymbol{r}, t) = \int \frac{dk_x}{2\pi} (\phi_e c_{k_x} + \phi_h c_{k_x}^\dagger) e^{i(k_x x - Et)} \tag{1.20}$$

is self-adjoint $[\hat{\Psi}(\boldsymbol{r}, t)]^\dagger = \hat{\Psi}(\boldsymbol{r}, t)$ (up to a phase factor). It is a coherent superposition of electron and hole excitations of equal weight, so it is charge-neutral [130, 158]. In reference to the Italian physicist Ettore Majorana, who found a charge neutral, real solution to the Dirac equation [101], such modes are called *Majorana* modes.

A pair of domain walls, as in the strip of p-wave superconductor shown in Fig. 1.1, supports counterpropagating modes at opposite edges. The chirality prevents backscattering, if the edges are sufficiently far apart that they are uncoupled. As a consequence, if we contact the strip from the left and the right we would see ballistic, quantized transmission along the edge even in the presence of disorder. This quantization refers to the thermal conductance, measured when the strip is contacted with two thermal baths at temperatures T_0 (left) and $T_0 + \delta T$ (right). The ratio of the transmitted heat current I_{th} across the strip and the applied temperature difference

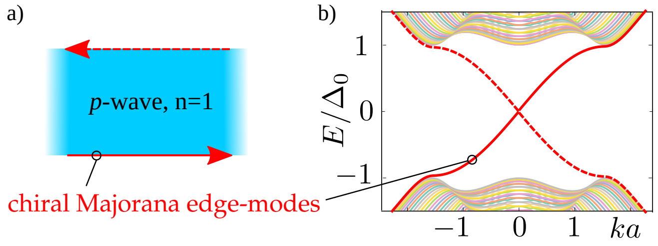

Figure 1.1. a) An infinite strip of a p-wave superconductor in the non-trivial phase (Chern number $n = 1$) supports chiral Majorana edge modes propagating in opposite directions at the top and the bottom edge. b) The corresponding spectrum as a function of the momentum k along the strip calculated by discretizing Hamiltonian (1.11) in the topological phase on a strip of width $W = 25a$ and lattice constant a.

δT yields a thermal conductance $G_{\text{th}} = nG_0^{\text{th}}$, where $G_0^{\text{th}} = \pi^2 k_{\text{B}}^2 T_0/6h$ and n is the number of chiral Majorana edge modes [130, 150, 160]. In analogy to the chiral electronic edge modes of the quantum Hall effect one speaks of the *thermal* quantum Hall effect.

Because of their charge neutrality the electrical conductance of the Majorana edge modes is zero. Electrical detection is still possible if one measures the time-dependent current fluctuations (shot noise) [2].

1.4 Chiral symmetry

One last symmetry is still missing to complete our discussion of fundamental symmetries in the tenfold-way, chiral symmetry. It is the symmetry that determines whether a topological superconductor or insulator *can* have N rather than just one protected edge mode.

In even spatial dimensions absence of chiral symmetry is a necessary condition for a $\mathbb{Z}$ topological invariant. Indeed, in table 1.1 we find that both in class D and class C two dimensional superconductors can have non-trival $\mathbb{Z}$-invariant. The invariant is the familiar Chern number of Eq. (1.14). Adding one of the two possible time-reversal symmetries, or in other words chiral symmetry, constrains the Chern number to $n = 0$. In the case of the helical $\boldsymbol{p}$-wave superconductor in class DIII (see chapter 3) this reduces the classification to $\mathbb{Z}_2$, while in class BDI all two-dimensional systems are topologically trivial.

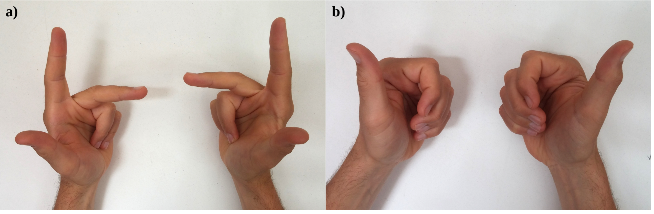

Figure 1.2. Both chirality and chiral symmetry derive from the Greek word $\chi\varepsilon\acute{\iota}\rho$ for hand. In physics we use the word as a reference to the two choices of orientation (a) or of rotation (b).

In odd spatial dimensions the opposite is true. Here, chiral symmetry introduces a new integer topological invariant, called the winding number. It allows for phases with more than one topological edge-mode. In superconductors chiral-symmetry always occurs in combination with both particle-hole and time-reversal symmetry. Again, the presence of these additional symmetry can force the winding number to be zero and render the topological classification according to chiral symmetry ineffective.

Before we return to the obvious question of when does chiral symmetry produce non-trivial topological superconducting phases, it is worth to have a look into the history of chiral symmetry. At least I found that it is quiet interesting. It also helped me to resolve some of the confusion that can arise when concepts originally from one field of physics are brought to a new context where they usually keep their name but often have quiet different meanings. Chiral symmetry is such an example. Readers who are only interested in its role in topological insulators and superconductors may skip ahead to section 1.4.3

1.4.1 Chiral symmetry in relativistic quantum field theories

Chiral symmetry, like chirality, derives from the Greek word $\chi\varepsilon\acute{\iota}\rho$ for hand. Its name originates from particle physics, more specifically relativistic quantum field theories. The roots of chiral symmetry go back to Dirac's formulation of a relativistic quantum mechanical wave-equation. In its covariant form and in natural units ($\hbar$, $c = 1$) the Dirac equation reads

$$i\gamma^{\mu}\partial_{\mu}\psi - m\psi = 0. \tag{1.21}$$

It describes free spin-1/2 fermions, such as electrons and quarks in $3+1$ space-time dimensions. The wave function Ψ is a four component Dirac-spinor that in the case of electrons is interpreted as a superposition of spin-up and down electrons and positrons, or more generally both mater and antimatter. The repeated index $\mu = 0, 1, 2, 3$ implies a summation of all dimensions of space-time, ∂_0 denotes the time derivative ∂_t and the remaining the spatial derivatives (∂_x, ∂_y, ∂_y). The four gamma matrices γ^0 ,γ^1, γ^2, γ^3 obey the fundamental anti-commutation relations

$$\{\gamma^\mu, \gamma^\nu\} = 2\eta^{\mu\nu}, \tag{1.22}$$

where $\eta^{\mu\nu} = (1, -1, -1, -1)$ is the metric signature of the four-dimensional Minkowski space. Only γ_0 is hermitian, the three others are anti-hermitian.

In $3+1$ spacetime dimensions there is another special matrix

$$\gamma_5 = i\gamma^0\gamma^1\gamma^2\gamma^3. \tag{1.23}$$

It is both hermitian and unitary, $(\gamma_5)^\dagger = \gamma_5$ and $(\gamma_5)^2 = 1$. Finally, it is odd under a spatial inversion, also called parity transformation P, $[(t, x, y, z) \rightarrow (t, -x, -y, -z)]$

$$P\gamma_5 P = -\gamma_5. \tag{1.24}$$

Since γ_5 anti-commutes with all four original gamma matrices, it also anti-commutes with the Dirac operator $\partial_\mu\gamma^\mu$. In the case of massless fermions ($m = 0$) this implies that eigenfunctions of the Dirac equation are simultaneous eigenfunctions of γ_5

$$0 = \gamma_5 i\partial_\mu\gamma^\mu\psi = -i\partial_\mu\gamma^\mu(\gamma_5\psi). \tag{1.25}$$

Such eigenfunctions $\gamma_5\psi_L = -\psi_L$ and $\gamma_5\psi_R = \psi_R$ are called chiral or Weyl fermions. As left and right handed partners they transform into each other under spatial inversion ($\gamma_5 P\psi_R = -P\gamma_5\psi_R = -P\psi_R$).

In the modern interpretation provided by quantum field theories the Dirac equation is understood in second quantization. The equations of motion of the Dirac field $\Psi(x^\mu)$ follows from the variation of an action with a Lagrangian density

$$\mathcal{L} = i\overline{\Psi}\gamma^\mu\partial_\mu\Psi - m\overline{\Psi}\Psi, \tag{1.26}$$

where $\overline{\Psi} = \Psi^\dagger\gamma_0$. The fermions couple to an additional bosonic gauge field A_μ following the principle of minimal coupling. In the case of electrons and positrons the gauge field corresponds to the electromagnetic field, for quarks to gluons the force carrier of quantum chromodynamics (QCD). For massless fermions this promotes the anti-commutation of the Dirac operator with the matrix γ_5 to a continuous gauge-symmetry $e^{i\theta\gamma_5}$ of the Lagrangian, called chiral symmetry.

1.4.2 Chiral random matrix theory

While the last section gives an answer to the question “why is chiral symmetry called chiral symmetry”, the reader may wonder about its connection to the tenfold way of topological insulators and superconductors. Chiral symmetry was added to the classification of topologically distinct Hamiltonian ensembles by Shuryak and Verbaarschot [155].

Verbaarschot studied the QCD vacuum using the tool of random matrix theory and coined the term chiral random matrix theory [175, 176]. By a Wick rotation ($it/\hbar \to \beta = 1/k_{\mathrm{B}}T$) one can rotate the QCD action from Minkowski (t, x, y, z) to Euclidean (β, x, y, z) space. The QCD partition function can then be expressed as the expectation value (a functional integral in Euclidean space) of the fermion determinant,

$$Z^{\mathrm{QCD}} = \left\langle \prod_f det(\mathcal{D} + m_f) \right\rangle . \tag{1.27}$$

$\mathcal{D}$ is the Dirac operator in Euclidean space, the product is over all quark flavors with mass m_f, and the average is taken over all configurations of the gauge field A_μ. If we consider the simplest possible problem the QCD vacuum in a box βL^3, we can write the Dirac operator as an (infinite) matrix in the basis of chiral fermions $\psi_{R/L}$. Since the Dirac operator still anti-commutes with (the Euclidean) matrix γ_5, we have $\langle \overline{\psi}_{R,m} | \mathcal{D} | \psi_{L,n} \rangle = 0 = \langle \overline{\psi}_{L,m} | \mathcal{D} | \psi_{R,n} \rangle$ for all quark flavors and modes n, m. Thus the chiral symmetry together with the fact that $\mathcal{D}$ is anti-Hermitian allows us to write the Dirac operator as block off-diagonal matrix,

$$\mathcal{D} = \begin{pmatrix} 0 & iW \\ iW^\dagger & 0 \end{pmatrix} . \tag{1.28}$$

Following the core idea of random matrix theory (RMT) we can hope to extract some essential features of the complex QCD vacuum even if we completely randomize interactions and abstract from all the space-time structure of the Dirac operator (including the fact that it lives in a box βL^3). We may simply choose all matrix elements of W from a random Gaussian distribution. The fermion determinant, and thus the partition function can be obtained from the eigenvalues of $\mathcal{D}$. In other words the random matrix problem reduces to finding the eigenvalue distribution $P(\{\lambda_n\})$ of the eigenvalue equation

$$\mathcal{D}\psi_n = i\lambda_n\psi_n, \tag{1.29}$$

where $\mathcal{D}$ is a anti-Hermitian, block off-diagonal matrix with Gaussian elements. A problem that can in fact be solved exactly.

We only need to divide by i, replace $\mathcal{D}$ by H, λ by E and the above problem is perfectly suitable to describe the random energy level distribution $P(\{E_n\})$ of a quantum dot with an arbitrary anti-commuting unitary Γ, $\Gamma H_{\mathrm{dot}} = -H_{\mathrm{dot}}\Gamma$.

1.4.3 Chiral symmetry in the tenfold way

In the context of topological insulators and superconductors chiral symmetry is simply defined by a unitary symmetry Γ that anti-commutes with the Hamiltonian $\Gamma H = -H\Gamma$. We have already learned that product $\mathcal{PT}$ of the two anti-unitary symmetries time-reversal and particle-hole is such a chiral symmetry. Unlike in the context of particle physics, this condensed matter definition of chiral symmetry has no obvious connection to geometry or handedness.[2]

Because it anti-commutes with the Hamiltonian, similar to particle-hole symmetry, chiral symmetry also implies a symmetry of the energy spectrum around zero. For every eigenstate $H|\psi_n\rangle = E_n|\psi_n\rangle$ there is partner state $\Gamma|\psi_n\rangle$ with energy $-E_n$, $H\Gamma|\psi_n\rangle = -\Gamma H|\psi_n\rangle = -E_n\Gamma|\psi_n\rangle$. There is, however, an important difference. Because it is unitary chiral symmetry does not invert the momentum. It implies $-E_n(k) = E_{n'}(k)$ rather than $-E_n(k) = E_{n'}(-k)$.

We are interested, in the case where H is both gapped and has no additional (commuting) unitary-symmetries. It follows that Γ^2 must be equal to the identity, since it commutes with H. We can thus choose the basis where $\Gamma = \mathrm{diag}(1,\ldots,1,-1,\ldots,-1)$, with equal occurrences

---

[2] The nomenclature can be particularly confusing since chiral, or chirality are also frequently used in the context of topological insulators and superconductors. Both the quantum Hall effect and the two dimensional $\boldsymbol{p}$-wave superconductor have chiral edge-modes. Neither of the two phases obeys an anti-commuting chiral symmetry.

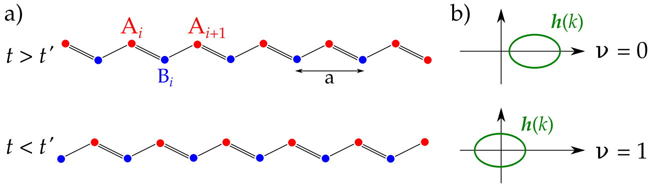

Figure 1.3. SSH model: a) sublattices and dimerization of the SSH tight-binding chain in the trivial (top) and non-trivial (bottom) phase. b) corresponding winding of the Bloch Hamiltonian vector $\boldsymbol{h}(k)$ in sublattice τ-space as k from $-\pi$ to π.

$\#1 = \#(-1)$. [3] In this basis H is block off-diagonal

$$H = \begin{pmatrix} 0 & H_{AB} \\ H_{AB}^{\dagger} & 0 \end{pmatrix}, \Psi = \begin{pmatrix} \psi_A \\ \psi_B \end{pmatrix}. \tag{1.30}$$

As we can see systems with chiral symmetry experience an implicit grading. We can group the degrees of freedom into A and B. H only couples A to B (and B to A) but not A to A or B to B. Such a grouping naturally arises in the tight-binding Hamiltonian of certain bipartite lattices. Not only in this context chiral symmetry is therefore often synonymously referred to as sublattice symmetry.

The simplest example of a chiral topological insulator with such a bipartite sublattice is the one dimensional Su-Schrieffer-Heeger model (SSH model) of polyacetalene [74]. As shown in Fig. 1.3a) it is a chain of sites A and B with alternating hoppings t and t',

$$H_{\mathrm{SSH}} = \sum_i t c_{i,\mathrm{A}}^{\dagger} c_{i,\mathrm{B}} + t' c_{i+1,\mathrm{A}}^{\dagger} c_{i,\mathrm{B}} + \mathrm{h.c.}, \tag{1.31}$$

where h.c. denotes the Hermitian conjugate hoppings. The difference $\Delta t = t - t'$ characterizes the amount of dimerization of the chain. There are two gapped phases, $\Delta t > 0$ and $\Delta t < 0$. In order to expose the topological distinction we switch to momentum space and group the two sublattices like in Eq. (1.30)

$$H = \sum_k \left(c_{k,\mathrm{A}}^{\dagger}, c_{i,\mathrm{B}}^{\dagger} \right) \begin{pmatrix} 0 & t + t'e^{-ika} \\ t + t'e^{ika} & 0 \end{pmatrix} \begin{pmatrix} c_{k,\mathrm{A}} \\ c_{i,\mathrm{B}} \end{pmatrix}. \tag{1.32}$$

---

[3] The case $\nu = \#1 - \#(-1) \neq 0$ gives rise to ν zero modes implying that H cannot be gapped.

If we further introduce Pauli matrices $\mu_{0,x,y,z}$ for the A,B-sublattice grading, we can write the Bloch Hamiltonian in the simple form

$$h(k) = (t + t' \cos ka)\mu_x + t \sin ka \, \mu_y. \tag{1.33}$$

The chiral symmetry $\Gamma = \mu_z$ forbids the terms proportional two μ_0 and μ_z and confines $\boldsymbol{h}(k) = (h_x, h_y, 0)$ two the xy-plane. This produces a topological classification of one-dimensional Hamiltonians distinct by their winding number around the origin

$$\nu = \frac{1}{2\pi i} \int_{-\pi}^{\pi} dk \, \frac{\partial}{\partial k} \log \det \, h(k). \tag{1.34}$$

This $\nu \in \mathbb{Z}$ topological invariant is characteristic for chiral topological insulators and superconductors. A similar winding number can be defined in the presence of chiral symmetry in all odd spatial dimensions. In class AIII where no other symmetry obstructs the formation of a $\nu \neq 0$ phase, this means that for all odd dimensions there are $\mathbb{Z}$ topological phases. Even dimensions in class AIII are simply connected, in other words topologically trivial. In contrast, the chern number (1.14) is defined only in even spatial dimensions.

Back to the SSH model, $t > t'$ is topologically trivial, $\nu = 0$, while $t < t'$ encloses the origin with $\nu = 1$ (for $t, t' > 0$), see Fig. 1.3b). As is easy to see in the limit $t \to 0$, there is a zero energy state at each end of finite chain. For nonzero t these states extend over some range ξ into the bulk of the system but are still exponentially localized at the ends as long as $\xi \ll L$. The case $t = t'$ corresponds to a topological phase transition where the bulk gap closes and end states extend over the complete chain, $\xi \to \infty$.

Not only is the SSH model a very simple example of a non-trivial chiral topological insulator, it also exposes the weak point of many chiral symmetry phases. As any symmetry protected topological phase, the phase distinction disappears once we break the symmetry. The Achilles' heel of many chiral models is that degrees of freedom exchanged by the chiral symmetry are particular to the model and not fundamentally related. For example if we want to gap out the zero-energy states on one of the ends of the SSH chain in the non-trivial phase all we need to do is attach another site.

1.4.4 Chiral symmetry in topological superconductors

Amongst the rich table of topological insulators and superconductors, one dimensional topological superconductors with $\mathcal{P}^2 = 1$ are of particular interest because they host so called Majorana bound states at their end. Majorana bound states are the zero-dimensional variant of the Majorana edge modes. These charge neutral self-adjoint localized zero energy quasi-particle excitations obey the characteristic properties

$$\gamma_i^\dagger = \gamma_i, \quad \{\gamma_i, \gamma_j\} = \delta_{ij} \tag{1.35}$$

of the creation and annihilation operators of a Majorana mode. Majorana bound states always come in pairs, at least one at each end of system or phase. Two Majoranas form a fermionic quasi-particle excitation $c^\dagger = \gamma_1 + i\gamma_2$. However, as long as they are well separated particle-hole symmetry pins them to zero-energy and protects there self-adjointness. The fact that in such a system one can define a non-local fermion whose two states, empty or occupied, both belong to the ground state manifold of the system has deep implications. Although sometimes referred to as Majorana fermions, Majorana bound states are not fermions, but the simplest example of non-abelian quasi-particles. An adiabatic exchange of two Majorana bound states corresponds to a unitary transformation on the (two-fold) degenerate ground state manifold, not just and overall phase factor ±1 like in the abelian cases of bosons and fermions.

The natural number of protected Majoranas is two, or one per end. This the situation in class D, with just particle-hole symmetry and $\mathcal{P}^2 = 1$. The famous Kitaev-chain [90], the superconducting analogon of the SSH model, is an example of a class D system, that can support a single Majorana at each end. The one dimensional p-wave superconductor (Eq. (1.11) with $p_y = 0$) is another. Two Majoranas at one end are not protected by particle-hole symmetry, combined they form a local fermion that can be pushed away form zero energy. This property is expressed by the topological invariant, which counts the number of topologically protected zero energy end states. In class D it is $\mathbb{Z}_2$. It seems clear that we need a chiral symmetry if we want multiple Majoranas. The tenfold way offers two options. Class DIII with the spinful time-reversal symmetry introduces Kramers degeneracy. However, this does not really improve our counting. A single Kramers pair of Majorana bound states is still protected, but the combination $\mathcal{P}^2 = 1$, $\mathcal{T}^2 = -1$ only allows $\nu = 0$ for the chiral invariant. Pairs of Kramers pairs can still be lifted. The topological classification remains $\mathbb{Z}_2$. Chiral symmetry in combination with $\mathcal{T}^2 = 1$ on the other hand promotes a class D system to class BDI. In one dimensional systems this combination does not obstruct chiral symmetry. It is characterized by an integer topological invariant $\nu \in \mathbb{Z}$, and allows for any number $N = |\nu|$ of protected Majorana bound states per end.

Quiet surprisingly, as we will study in more detail in chapter 2, one of the most prominent experimental candidate systems for hosting Majorana bound states possesses an approximate chiral symmetry. The system in mind is a semiconducting nanowire with proximity induced superconductivity (see Fig. 1.4 and Fig. 1.5a). Originally proposed in 2010 by Lutchyn, Sau, & Das Sarma [98] and by Oreg, Refael & von Oppen [117] it was the first system to show strong indications for the realization of a one-dimensional topological superconductor in 2012 [109, 47, 43]. Strong spin-orbit coupling in the wire, together with an external magnetic field, break both time-reversal and spin-rotation symmetry. The wire is contacted by an s-wave bulk superconductor which induces superconducting pairing in the wire via the proximity effect. Together, both effects place the wire in symmetry class D. However, as argued by Tewari and Sau [166] in the limit of a nanowire with a width W much narrower than the characteristic length scale $l_{\mathrm{SO}} = \hbar^2(m_{\mathrm{eff}}\alpha_{\mathrm{SO}})^{-1}$, where α_{SO} is the amplitude of Rashba spin-orbit coupling and m_{eff} the effective mass of the band dispersion, an additional chiral symmetry emerges.

In this narrow wire limit the quasi one-dimensional Bogoliubov-De Gennes Hamiltonian is given by

$$H_{\mathrm{BDI}} = \left(\frac{\boldsymbol{p}^2}{2m_{\mathrm{eff}}} + U(\boldsymbol{r}) - \mu\right)\tau_z + V_{\mathrm{Z}}\sigma_x\tau_z + \frac{\alpha_{\mathrm{SO}}}{\hbar}p_x\sigma_y\tau_z + \Delta\sigma_y\tau_y, \tag{1.36}$$

with particle-hole symmetry $\mathcal{P} = \tau_x\mathcal{K}$, chiral symmetry $\Gamma = \tau_x$ and a fake time-reversal symmetry $\mathcal{T}^* = \mathcal{K}$. The nanowire is placed along the x-direction. The potential $U(\boldsymbol{r})$ combines confinement in y- and z-direction as well as electrostatic disorder. The true time-reversal $\sigma_y\mathcal{K}$ of the fermions is broken by the magnetic field B. It is applied along the direction of the wire and induces a Zeeman splitting $V_Z = g_{\mathrm{eff}}\mu_{\mathrm{B}}B$.[4] The proximity effect gives rise to an effective s-wave pair-potential with amplitude Δ. Rashba spin-orbit coupling yields an effective spin-orbit field

---

[4] Possibly important chiral symmetry breaking effects of the orbital part of the magnetic field are currently investigated by B. Nijholt, Master student at Kavli Institute of Nanoscience Delft.

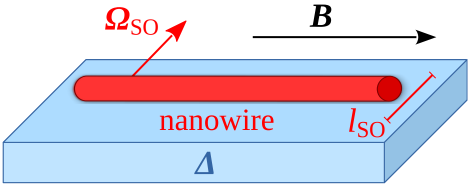

Figure 1.4. A semiconductor nanowire (red) on top of a s-wave superconductor (blue) can be tuned into a topological superconducting phase with a Majorana bound state at each end. If the spin-orbit length l_{SO} is larger than the wire width an additional chiral symmetry promotes the wire from class D to class BDI and allows for multiple Majorana's at each end.

$\Omega_y(p_x) = \alpha_{\mathrm{SO}} p_x/\hbar$ in plane with the substrate but perpendicular to the direction of the wire (and the magnetic field). In general the Rashba effect has a second component $\Omega_x(p_y)$, this introduces another spin-orbit term $\alpha_{\mathrm{SO}} h^{-1} p_y \sigma_x \tau_0$ which commutes with τ_x, breaks the chiral symmetry and brings the wire back to class D. However, the finite width of the wire confines the momentum p_y and limits the transversal spin-orbit interaction. In chapter 2 we show that for a small number of transversal modes this chiral symmetry is effectively unbroken for $W \lesssim l_{\mathrm{SO}}/2$. All of the three original Majorana nanowire experiments were indeed in this regime.

If we compare the chiral nanowire of Hamiltonian (1.36) with the SSH model from the previous section there is a noteworthy and experimentally relevant difference. In the SSH model the chiral symmetry is a sublattice symmetry tied to the bipartite structure of the chain. As we have already mentioned this is the Achilles' heel of the topological phases in the SSH chain. Its chiral symmetry would be broken if we attached a lead without this lattice symmetry to measure the transport signatures of the phase or equally if the chain is exposed to (uncorrelated) electro static disorder in the on-site-energies of A and B. It could be detrimental if the same happened to our chiral nanowire. Fortunately, at least in the two just mentioned scenarios we are safe.

Due to the intimate relation between the number of Majorana's $|Q|$ and the zero bias-voltage resonant Andreev conductance $G \geq 2e^2|Q|/h$ (see chapter 2) the effectively unbroken chiral symmetry, allowing for $|Q| > 1$, has direct observable consequences.

1.5 This thesis

1.5.1 Chapter 2

Motivated by the effective chiral symmetry in topological, superconducting nanowires pointed out by Tewari and Sau [166], we study Andreev refection in symmetry class BDI in chapter 2. We show how the associated topological quantum number $Q \in \mathbb{Z}$ can be expressed as the trace of the Andreev reflection block $Q = \mathrm{Tr}\, r_{\mathrm{he}}$ of the scattering matrix at the end of the nanowire when it is contacted by a metallic lead. This simple link allows us to constrain the electrical conductance G of the wire. We derive $G = (2e^2/h)|Q|$ for $|Q| = N, N-1$, and more generally provide a Q-dependent upper and lower bound on G. We calculate the probability distribution $P(G)$ for chaotic scattering, in the circular ensemble of random-matrix theory, to obtain the Q-dependence of weak localization and mesoscopic conductance fluctuations. Finally we investigate the effects of chiral symmetry breaking by spin-orbit coupling of the transverse momentum (causing a class BDI-to-D crossover), in a model of a disordered semiconductor nanowire with induced superconductivity. For wire widths less than the spin-orbit coupling length, we find that it is effectively unbroken. The conductance as a function of chemical potential as a result can show a sequence of $2e^2/h$ steps — insensitive to disorder.

1.5.2 Chapter 3

In this chapter we step from one to two dimensional topological superconductors. The protected edge states are in this case one dimensional propagating modes rather than zero dimensional bound states. Their edge modes fall in three distinct classes, chiral Dirac modes in the case of spin-triplet d-wave superconductivity or chiral and helical Majorana modes for spin-singlet p-wave symmetry. All are charge-neutral modes. Here we propose a geometry similar to the one shown in Fig. 1.5c) where it is possible to detect and distinguish these edge modes electrically. For this purpose we calculate the Andreev conductance of a superconducting ring interrupted by a flux-biased Josephson junction. The presence of the topological edge modes produces h/e-periodic magnetoconductance oscillations of amplitude $\simeq (e^2/h)N^{-1/2}$, measured via an N-mode point contact at the inner or outer perimeter of the grounded ring. For Dirac modes the oscillations in the two contacts are independent, while for an

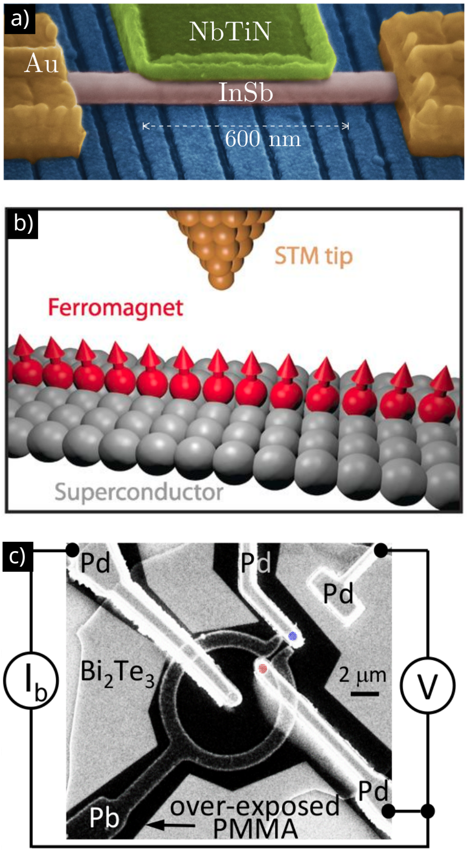

Figure 1.5. Experimental platforms of topological superconductivity: a) scanning electron microscope (SEM) image of InSb nanowire akin to Fig. 1.4 probed by Au contacts. Superconductivity is induced by proximity to a NbTiN superconductor. First signatures of Majorana bound states have been measured in a similar device by Mourik et al. [109]; b) a chain of magnetic atoms (red) on top of a superconductor which can be probed by a scanning tunneling microscope (STM); Evidence of Majorana end states has been by reported Nadj-Perge et al. [111]; c) a superconducting ring of Pd on the surface of the three-dimensional topological insulator Bi_2Te_3 probed by several leads in a corbino geometry. Measurements in support of topological superconductivity in this device have been reported by Pang et al. [120]. [a) image provided by V. Mourik, b) from Ref. [111], c) from Ref. [120]]

unpaired Majorana mode they are phase locked by a topological phase transition at the Josephson junction.

1.5.3 Chapter 4

In this first out of two chapters on statistical topological superconductors we again study two-dimensional superconductors spin-triplet p-wave pairing. An anisotropic version of the p-wave superconductor could be realized by weakly coupled arrays nanowires or chains of magnetic atoms on the surface of a superconductor, see Fig. 1.5. The previously studied isotropic phases support chiral or helical Majorana edge modes with a quantized (length L-independent) thermal conductance. Sufficiently strong anisotropy removes both chirality and helicity. In the clean limit this makes the system a weak topological superconductor and doubles the edge conductance. Disorder turns it into a statistical topological insulator and imposes a super-Ohmic $1/\sqrt{L}$ decay of the conductance. We explain the absence of localization in the framework of the Kitaev Hamiltonian, contrasting the edge modes of the two-dimensional system with the one-dimensional Kitaev chain. While the disordered Kitaev chain has a log-normal conductance distribution peaked at an exponentially small value, the Kitaev edge has a bimodal distribution with a second peak near the conductance quantum. Shot noise provides an alternative, purely electrical method of detection of these charge-neutral edge modes.

1.5.4 Chapter 5

Fulga, van Heck, Edge and Akhmerov [68] demonstrated how – as in the previous chapter – an in the strong sense trivial phase could be promoted to a statistical topological insulator in the presence of disorder owing to an average symmetry of the disorder ensemble. In this chapter we show how such statistical topological phases also persist in the presence of already non-trivial strong phases. More generally, we extend the single-particle topological classification of insulators and superconductors to include systems in which disorder preserves average reflection symmetry. We show that the topological group structure of bulk Hamiltonians and topological defects is exponentially extended when this additional condition is met, and examine some of its physical consequences. Those include localization-delocalization transitions between topological phases with the same boundary conductance, as well as gapless topological de-

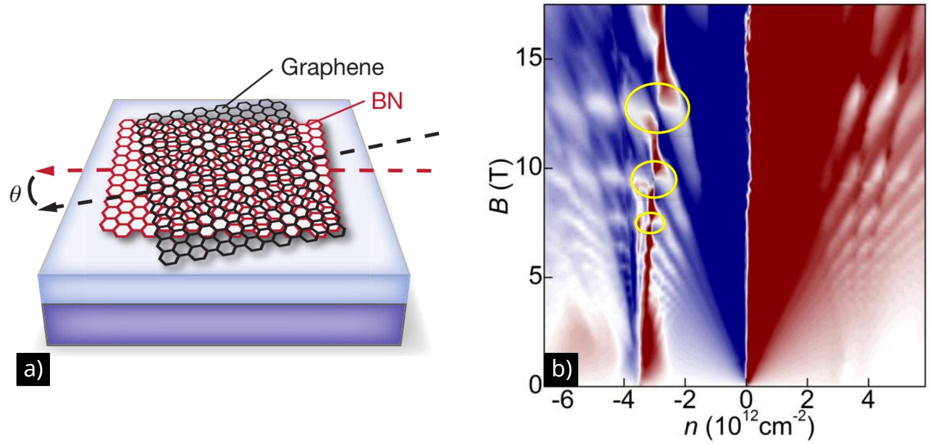

Figure 1.6. Hofstadter's butterfly in graphene: a) Cartoon of graphene on hexagonal boron nitride (BN) [from Dean et al. [45]]. The emergent moiré superlattice can be tuned by varying the alignment angle θ between the native lattices of the two materials; b) cloning of Dirac points in the Hall conductivity of graphene's moiré superlattice [from Ponomarenko et al. [124]]. Yellow circles highlight a series of *gapped* cloned Dirac points. In chapter 6 we propose a way to close them by varying θ.

fects stabilized by average reflection symmetry. We examine this extended classification of statistical topological phases in two concrete examples. The first one is an extension of the anisotropic p-wave superconductor from the previous chapter belonging to symmetry class D. The extended classification gives rise to a new defect, the Kitaev domain wall, at the interface between two phases with the same strong, but different weak indices. Like its edge-mode partner the Kitaev domain wall is detectable via characteristic $1/\sqrt{L}$ decay of the electrical shot noise along the 1d defect. The second example, a three dimensional superconductor with weak weak-phases in class DIII, demonstrates the dimensional hierarchy of extended classification.

1.5.5 Chapter 6

In this chapter we leave the topic of topological superconductors. Instead we study the conductance signatures of a special topological phase transition of a different type, namely in the quantum Hall effect. More specifically we examine the fractal quantum Hall effect of a periodic lattice known has Hofstadter butterfly [75], see Fig. 1.6. Long admired for its beauty, but almost regarded as a problem of mathematical physics the butterfly has recently been spotted in transport experiments on the Van der Waals superlattice of graphene on hexagonal boron nitride [124, 45, 78]. While requiring 1000 T for the native graphene unit cell, the large size of the moiré superlattice, sketched in Fig. 1.6b), makes magnetic fluxes on the order of e^2/h per unit cell experimentally accessible. A central theme of the experiments is the emergence of finite magnetic field Dirac fermions. The fractal spectrum of magnetic minibands, induced by the moiré superlattice of graphene on an hexagonal crystal substrate, is known to exhibit gapped Dirac cones. We show that the gap can be closed by slightly misaligning the substrate, producing a hierarchy of conical singularities (Dirac points) in the band structure at rational values $\Phi = (p/q)(h/e)$ of the magnetic flux per supercell. Each Dirac point signals a switch of the topological quantum number in the connected component of the quantum Hall phase diagram. Here, when the Dirac cones become gapless, we encounter yet another chiral symmetry, that of the two-dimensional Dirac Hamiltonian

$$H = p_x\sigma_x + p_y\sigma_y. \tag{1.37}$$

It anti-commutes with the third Pauli-matrix σ_z, signifying the absence of a mass $m\sigma_z$. Model calculations reveal the scale invariant conductivity $\sigma = 2qe^2/\pi h$ and Klein tunneling associated with the massless, chiral Dirac fermions of Hamiltonian (1.37) at these connectivity switches.

1.5.6 Chapter 7

The work presented in this final chapter is a direct result of collaboration with Andrea Caviglia's group in Delft that works on transport experiments in complex oxides, in this particular case the mobile electron system at the $LaAlO_3/SrTiO_3$ interface. Fig. 1.7 shows the system. Although there are indications of unconventional [132], possibly even topological superconductivity [55, 113], we focus on one of its (in comparison) high temperature signatures. As we can see in Fig. 1.7c) the two-dimensional electron system is unusually sensitive to the application of an in-plane magnetic field. Following extensive low-temperature experiments this giant negative magnetoresistance (dropping by more than 70%) has been attributed

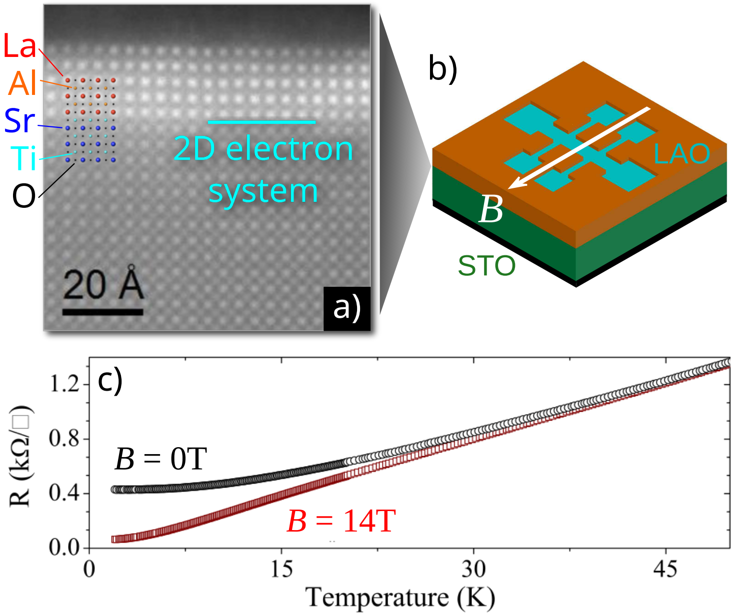

Figure 1.7. $LaAlO_3/SrTiO_3$ interface: a) scanning transmission electron micrograph of the atomically sharp interface between the two complex oxides. A two-dimensional system of mobile electrons (2DES) lives at the interface of the two insulators; c) temperature dependent sheet resistance R of the 2DES measured in a Hall bar under an in-plane magnetic field B (b). At low temperatures the sheet resistance is almost an order of magnitude smaller for a 14 T in-plane field when compared to its zero field value [a) adapted from Ref. [132], c) from Ref. [15]]. This giant drop of resistance has been attributed to Kondo physics [81, 137]. In chapter 7 we propose a semiclassical alternative.

to a magnetic-field induced transition between interacting phases of conduction electrons with Kondo-screened magnetic impurities [81, 137]. In this chapter we present experiments performed in Delft over a broad temperature range. These show the persistence of the magnetoresistance up to the 20 K range — indicative of a single-particle mechanism. Motivated by a striking correspondence between the temperature and carrier density dependence of our magnetoresistance measurements we propose an alternative explanation. Working in the framework of semiclassical Boltzmann transport theory we demonstrate that the combination of spin-orbit coupling and scattering from finite-range impurities can explain the observed magnitude of the negative magnetoresistance, as well as the temperature and electron density dependence.

Chapter 2

Andreev reflection from a topological superconductor with chiral symmetry

2.1 Introduction

The classification of topological states of matter, the socalled “ten-fold way” [7], has five topologically nontrivial symmetry classes in each dimensionality [138]. For a one-dimensional wire geometry, two of these five describe a topological superconductor and the other three a topological insulator. Each symmetry class has a topological quantum number Q that counts the number of protected bound states at the end of the wire. These end states are of particular interest in the topological superconductors, because they are pinned at zero excitation energy by electron-hole symmetry and are a condensed matter realization of Majorana fermions [6, 13]. Signatures of Majorana zero-modes have been reported in conductance measurements on InSb and InAs nanowires, deposited on a superconducting substrate [109, 47, 43].

A key distinction between superconducting and insulating wires is that $Q \in \mathbb{Z}_2$ is a parity index in a topological superconductor, while all integer values $Q \in \mathbb{Z}$ can appear in a topological insulator. In other words, while there can be any number of protected end states in an insulating wire, pairs of Majorana zero-modes have no topological protection. The symmetry that prevents the pairwise annihilation of end states in an insulating wire is a socalled chiral symmetry of the Hamiltonian: $H \mapsto -H$ upon exchange

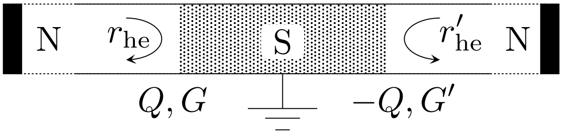

Figure 2.1. Superconducting wire (S) connected at both ends to a normal metal reservoir (N). The current I flowing from the normal metal (at voltage V) into the grounded superconductor gives the conductance $G = I/V$ of the NS junction. The wire is assumed to be sufficiently long that there is negligible transmission from one end to the other. Chiral symmetry then produces a topologically protected quantum number $Q \in \mathbb{Z}$. Both $G = (2e^2/h)\mathrm{Tr}\, r_{\rm he} r_{\rm he}^\dagger$ and $Q = \mathrm{Tr}\, r_{\rm he}$ are determined by the Andreev reflection matrix $r_{\rm he}$ of the junction. While the NS junctions at the two ends of the wire can have independently varying conductances G and G', the topological quantum numbers are related by $Q' = -Q$.

$\alpha \leftrightarrow \beta$ of an internal degree of freedom, typically a sublattice index.

In an interesting recent development, Tewari and Sau [166] have argued (motivated by Ref. [115]) that an approximate chiral symmetry may stabilize pairs of Majorana zero-modes in a sufficiently narrow nanowire. The symmetry $H \mapsto -H$ when e $\leftrightarrow$ h involves the exchange of electron and hole indices e,h.[1]. It is distinct from electron-hole symmetry, which involves a complex conjugation $H \mapsto -H^*$ and is a fundamental symmetry of the problem. The combination of chiral symmetry and electron-hole symmetry promotes the superconductor from symmetry class D to symmetry class BDI, extending the range of allowed values of Q from $\mathbb{Z}_2$ to $\mathbb{Z}$.

In this paper we investigate the consequences of chiral symmetry for the electrical conductance of the superconducting nanowire, attached at the end to a normal metal contact. (See Fig. 2.1.) The conductance G is determined by the matrix $r_{\rm he}$ of Andreev reflection amplitudes (from e to h, at the Fermi level),

$$G = \frac{2e^2}{h}\mathrm{Tr}\, r_{\rm he} r_{\rm he}^\dagger, \tag{2.1}$$

at low bias voltages and low temperatures and assuming that there is no transmission from one end of the wire to the other end. We will show that the topological quantum number $Q \in \mathbb{Z}$ in the presence of chiral

---

[1] A different type of chiral symmetry, which does not exchange electron and hole degrees of freedom, appears for two-dimensional superconductors, see for example Cheng et. al. [36]

symmetry is directly related to the Andreev reflection matrix,

$$Q = \mathrm{Tr}\, r_{\mathrm{he}}. \tag{2.2}$$

The intimate relation between transport and topology expressed by these two equations allows us to make specific predictions for the Q-dependence of G.

The outline of the paper is as follows. In the next section we derive Eq. (2.2) from the general scattering formulation of one-dimensional topological invariants [65], and obtain model-independent results for the relation between G and Q. More specific results are obtained in Sec. 2.3 using random-matrix theory [12],[2] under the assumption of chaotic scattering at the NS interface. Then in Sec. 2.4 we numerically study a microscopic model of a superconducting nanowire [98, 117], to test our analytical predictions in the presence of a realistic amount of chiral symmetry breaking. We conclude in Sec. 4.6.

2.2 Relation between conductance and topological quantum number

In a translationally invariant superconducting wire with chiral symmetry, the topological quantum number Q can be extracted from the Bogoliubov-de Gennes Hamiltonian as a winding number in the one-dimensional Brillouin zone [166]. In order to make contact with transport measurements, we describe here an alternative scattering formulation for a finite disordered wire (adapted from Ref. [65]), that expresses Q as the trace of the Andreev reflection matrix from one of the ends of the wire. The electrical conductance G can then be related to Q by an inequality.

2.2.1 Trace formula for the topological quantum number

The scattering problem is defined by connecting the N-mode superconducting wire (S) to a normal metal reservoir (N). The $2N \times 2N$ reflection matrix $r(E)$ relates the incident and reflected amplitudes of electron (e) and hole (h) excitations at energy E. It has a block structure of $N \times N$

---

[2] When comparing results, note that the definition of G_0 used in this reference differs by a factor of two from the one used here.

submatrices,

$$r = \begin{pmatrix} r_{\text{ee}} & r_{\text{eh}} \\ r_{\text{he}} & r_{\text{hh}} \end{pmatrix}, \quad \tau_x = \begin{pmatrix} 0 & 1 \\ 1 & 0 \end{pmatrix}, \tag{2.3}$$

where we have also introduced a Pauli matrix τ_x acting on the electron-hole degree of freedom.

We assume that both time-reversal symmetry and spin-rotation symmetry are broken, respectively, by a magnetic field and spin-orbit coupling. Electron-hole symmetry and chiral symmetry are expressed by

$$\tau_x r(-E)\tau_x = \begin{cases} r^*(E) & \text{(e-h symmetry)}, \\ r^\dagger(E) & \text{(chiral symmetry)}. \end{cases} \tag{2.4}$$

Taken together, the two symmetries imply that $r(E) = r^T(E)$ is a symmetric matrix. For spinless particles, this would be a time-reversal symmetry, but the true time-reversal symmetry also involves a spin-flip.

In what follows we consider the reflection matrix at the Fermi level ($E = 0$). The symmetry relations (2.4) then take the form

$$r_{\text{ee}} = r_{\text{hh}}^* = r_{\text{ee}}^T, \quad r_{\text{he}} = r_{\text{eh}}^* = r_{\text{he}}^\dagger. \tag{2.5}$$

These symmetries place the wire in universality class BDI, with topological quantum number determined [65] by the sign of the eigenvalues of the Hermitian matrix $\tau_x r$. This can be written as a trace if we assume that the wire is sufficiently long that we can neglect transmission of quasiparticles from one end to the other. The reflection matrix is then unitary, $rr^\dagger = 1$. The matrix product $\tau_x r$ is both unitary and Hermitian, with eigenvalues ± 1. The topological quantum number $Q \in \{-N, \ldots, -1, 0, 1, \ldots N\}$ is given by the trace

$$Q = \tfrac{1}{2}\,\mathrm{Tr}\,\tau_x r = \mathrm{Tr}\, r_{\text{he}}. \tag{2.6}$$

All of this is for one end of the wire. The other end has its own reflection matrix r', with topological quantum number $Q' = \frac{1}{2}\mathrm{Tr}\,\tau_x r'$. Unitarity with chiral symmetry relates r and r' via the transmission matrix t,

$$S = \begin{pmatrix} r & t \\ t^T & r' \end{pmatrix}, \quad (\tau_x S)^2 = 1,$$

$$\Rightarrow (\tau_x r)(\tau_x t) = -(\tau_x t)(\tau_x r'). \tag{2.7}$$

If we allow for an infinitesimally small transmission for all modes through the wire, so that t is invertible, this implies that $\mathrm{Tr}\,\tau_x r = -\mathrm{Tr}\,\tau_x r'$, hence $Q' = -Q$.

The sign of the topological quantum number at the two ends of the wire can be interchanged by a change of basis of the scattering matrix, $S \mapsto \tau_z S \tau_z$, so the sign of Q by itself has no physical significance — only relative signs matter.

2.2.2 Conductance inequality

In the most general case, the Andreev reflection eigenvalues $R_n \in [0,1]$ are defined as the eigenvalues of the Hermitian matrix product $r_{\mathrm{he}} r_{\mathrm{he}}^\dagger$. Because of chiral symmetry, the matrix r_{he} is itself Hermitian, with eigenvalues $\rho_n \in [-1,1]$ and $R_n = \rho_n^2$. These numbers determine the linear response conductance G of the NS junction,

$$G = G_0 \sum_{n=1}^{N} R_n, \quad G_0 = 2e^2/h. \tag{2.8}$$

The factor of 2 in the definition of the conductance quantum G_0 is not due to spin (which is included in the sum over n), but accounts for the fact that charge is added to the superconductor as charge-$2e$ Cooper pairs.

The Andreev reflection eigenvalues R_n different from $0, 1$ are twofold degenerate (Béri degeneracy) [16, 186]. The eigenvalues ρ_n are not degenerate, but another pairwise relation applies. Consider an eigenvalue ρ of r_{he} with eigenvector ψ. It follows from the symmetry relations (2.5), together with unitarity of r, that $r_{\mathrm{he}} r_{\mathrm{hh}} \psi^* = (r_{\mathrm{eh}} r_{\mathrm{ee}} \psi)^* = -(r_{\mathrm{ee}} r_{\mathrm{he}} \psi)^* = -\rho\, r_{\mathrm{hh}} \psi^*$. So $-\rho$ is also an eigenvalue of r_{he}, unless $r_{\mathrm{hh}} \psi^* = 0$. This is not possible, again because of unitarity, if $|\rho| < 1$. If also $\rho \neq 0$, the pair $\rho, -\rho$ is distinct.

So we see that the ρ_n's different from $0, \pm 1$ come in pairs $\pm\rho$ of opposite sign. They cannot contribute to the topological quantum number $Q = \sum_n \rho_n$, only the ρ_n's equal to ± 1 can contribute (because $|Q|$ of them can come unpaired). Since each $|\rho_n| = 1$ contributes an amount G_0 to the conductance, we arrive at the lower bound

$$G/G_0 \geq |Q|. \tag{2.9}$$

The upper bound for G/G_0 is trivially N, the number of modes, but this can be sharpened if $N - |Q|$ is an odd integer. There must then be an unpaired $\rho_n = 0$, leading to the upper bound

$$G/G_0 \leq \min(N, N + (-1)^{N-|Q|}). \tag{2.10}$$

For $N = 1$ these inequalities imply $G/G_0 = |Q|$, but for $N > 1$ there is no one-to-one relationship between G and $|Q|$.

Because the sign of Q does not enter, the same inequalities constrain the conductances G and G' of the NS junctions at both ends of the wire (since $Q' = -Q$). Otherwise, the two conductances can vary independently.

Both inequalities (2.9) and (2.10), derived here for symmetry class BDI with $|Q| = 0, 1, 2, \ldots N$, apply as well to symmetry class D with $Q = 0, 1$ — essentially because the Béri degeneracy is operative there as well [186].

2.3 Conductance distribution for chaotic scattering

A statistical relation between conductance and topological quantum number can be obtained if we consider an ensemble of disordered wires and ask for the Q-dependence of the probability distribution $P(G)$. For chaotic scattering at the NS junction we can calculate the distribution from a circular ensemble of random-matrix theory. Such a calculation was performed in Ref. [12] for a superconductor without chiral symmetry (symmetry class D). Here we follow that approach in the chiral orthogonal ensemble of symmetry class BDI.

The assumption of chaotic scattering requires a separation of time scales $\tau_{\text{dwell}} \gg \tau_{\text{mixing}}$, meaning that a quasiparticle dwells long enough at the NS interface for all available scattering channels to be fully mixed. Conceptually, this can be realized by confining the particles near the NS interface in a ballistic quantum dot [12]. In the next section we consider a microscopic model of a disordered NS interface with comparable dwell time and mixing time, but as we will see, the conductance distributions from the circular ensemble are still quite representative.

2.3.1 Distribution of Andreev reflection eigenvalues

We start from the polar decomposition of the reflection matrix in class BDI,

$$r = \begin{pmatrix} U & 0 \\ 0 & U^* \end{pmatrix} \begin{pmatrix} \Gamma & \Lambda \\ \Lambda^T & \Gamma \end{pmatrix} \begin{pmatrix} U^T & 0 \\ 0 & U^\dagger \end{pmatrix}. \tag{2.11}$$

The matrix U is an $N \times N$ unitary matrix and the $N \times N$ matrices Γ, Λ are defined by

$$\Gamma = \bigoplus_{m=1}^{M} \begin{pmatrix} \cos\alpha_m & 0 \\ 0 & \cos\alpha_m \end{pmatrix} \oplus \emptyset_{|Q|} \oplus \mathbb{1}_\zeta, \tag{2.12a}$$

$$\Lambda = \pm \bigoplus_{m=1}^{M} \begin{pmatrix} 0 & -i\sin\alpha_m \\ i\sin\alpha_m & 0 \end{pmatrix} \oplus \mathbb{1}_{|Q|} \oplus \emptyset_\zeta. \tag{2.12b}$$

The ± sign refers to the sign of Q. (For $Q = 0$ the sign can be chosen arbitrarily.) The symbols $\mathbb{1}_n, \emptyset_n$ denote, respectively, an $n \times n$ unit matrix or null matrix. We have defined $\zeta = 0$ if the difference $N - |Q|$ is even and $\zeta = 1$ if $N - |Q|$ is odd. The $M = (N - |Q| - \zeta)/2$ angles α_m are in the interval $-\pi/2 < \alpha_r \leq \pi/2$.

The Andreev reflection matrix $r_{\rm he} = (U\Lambda U^\dagger)^T$ has eigenvalues $\rho_n = \sin\alpha_n$ ($n = 1, 2, \ldots M$), $\rho_n = -\sin\alpha_n$ ($n = M+1, M+2, \ldots 2M$), $\rho_n = 1$ ($n = 2M+1, 2M+2, \ldots 2M+|Q|$), and additionally $\rho_N = 0$ if $N - |Q|$ is odd — all of which is consistent with the general considerations of Sec. 2.2.2.

From the polar decomposition we obtain the invariant (Haar) measure $\mu(r) = r^\dagger dr$ that defines the uniform probability distribution in the circular ensemble, $P(r)d\mu(r) = d\mu(r)$. Upon integration over the independent degrees of freedom in the unitary matrix U we obtain the distribution $P(\alpha_1, \alpha_2, \ldots \alpha_M)$ of the angular variables. A change of variables then gives the distribution $P(R_1, R_2, \ldots R_M)$ of the twofold degenerate Andreev reflection eigenvalues $R_n = \sin^2\alpha_n$. Details of this calculation are given in App. 2.6.1. The result is

$$P(\{R_n\}) \propto \prod_{m=1}^{M} {R_m}^{\zeta-1/2}(1-R_m)^{|Q|} \prod_{i<j=1}^{M} (R_i - R_j)^2. \tag{2.13}$$

The M twofold degenerate eigenvalues repel each other quadratically; furthermore, they are repelled with exponent $|Q|$ from the $|Q|$ eigenvalues pinned at unity. While the probability of finding a small reflection eigenvalue is enhanced for $N-|Q|$ even ($\zeta=0$), the eigenvalue $R_N=0$ pinned at zero for $N-|Q|$ odd ($\zeta=1$) produces a square root repulsion.

2.3.2 Dependence of conductance distribution on the topological quantum number

Integration over the probability distribution (2.13) of the Andreev reflection eigenvalues gives the distribution $P(g)$ of the dimensionless electrical conductance

$$g \equiv G/G_0 = |Q| + 2\sum_{m=1}^{M} R_m. \tag{2.14}$$

The first term $|Q|$ is the quantized contribution from the topologically protected eigenvalues, and the factor of two in front of the sum accounts for the Béri degeneracy of the M eigenvalues without topological protection.

The conductance distribution is only nonzero in the interval

$$|Q| \leq g \leq \min(N, N+(-1)^{N-|Q|}), \tag{2.15}$$

see Sec. 2.2.2. It is a trivial delta function, $P(g)=\delta(g-|Q|)$, when $|Q|=N, N-1$. Explicit results for small values of N are

$$N=1: \ P(g)=\delta(g-|Q|), \tag{2.16a}$$

$$N=2: \ P(g)=\begin{cases}\delta(g-|Q|) & \text{if } |Q|=1,2,\\ (8g)^{-1/2} & \text{if } |Q|=0,\end{cases} \tag{2.16b}$$

$$N=3: \ P(g)=\begin{cases}\delta(g-|Q|) & \text{if } |Q|=2,3,\\ \frac{3}{16}\sqrt{2}(3-g)(g-1)^{-1/2}\theta(g-1) & \text{if } |Q|=1,\\ \frac{3}{8}(2g)^{1/2}\theta(2-g) & \text{if } |Q|=0,\end{cases} \tag{2.16c}$$

$$N=4: \ P(g)=\begin{cases}\delta(g-|Q|) & \text{if } |Q|=3,4,\\ \frac{15}{128}\sqrt{2}(4-g)^2(g-2)^{-1/2}\theta(g-2) & \text{if } |Q|=2,\\ \frac{15}{32}\sqrt{2}(3-g)(g-1)^{1/2}\theta(g-1)\theta(3-g) & \text{if } |Q|=1,\\ \frac{45}{512}\pi g^2-\frac{45}{128}\Big[\sqrt{2}(4-g)\sqrt{g-2} & \\ \qquad +g^2\arctan\sqrt{\tfrac{1}{2}(g-2)}\Big]\theta(g-2) & \text{if } |Q|=0.\end{cases} \tag{2.16d}$$

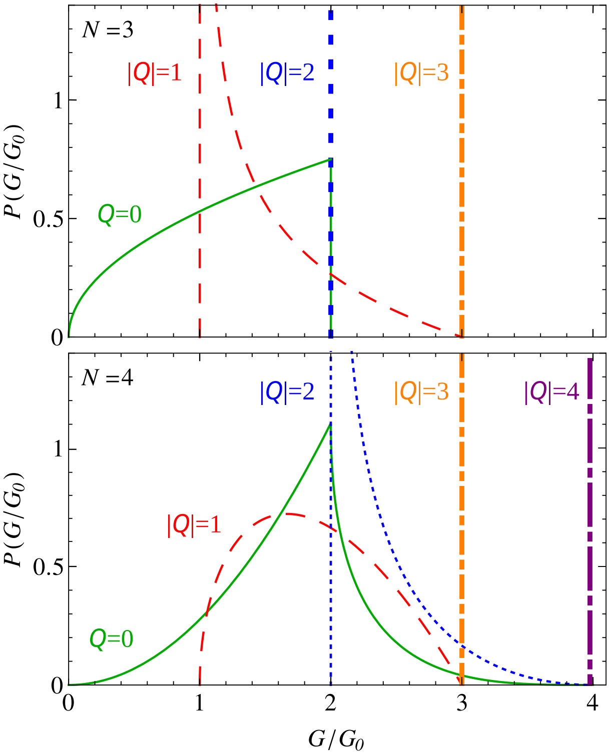

Figure 2.2. Probability distribution of the conductance for chaotic scattering in symmetry class BDI. The distributions are plotted from Eq. (2.16) for $N = 3, 4$ modes and different values of the topological quantum number Q. Thick vertical lines indicate a δ-function distribution.

The step function $\theta(x)$ (equal to 0 for $x < 0$ and 1 for $x > 0$) is used to indicate the nontrivial upper and lower bounds of the conductance. (The trivial bounds $0 \leq g \leq N$ are not indicated explicitly.) The distributions for $N = 3, 4$ are plotted in Fig. 2.2.

The first two moments of the conductance can be calculated in closed form for any value of N, Q, using known formulas for Selberg integrals [146]. (Alternatively, one can directly integrate over the BDI circular ensemble, see App. 2.6.2.) We find

$$\langle G/G_0\rangle = \frac{N(N-1)+Q^2}{2N-1}, \tag{2.17}$$

$$\mathrm{Var}\,(G/G_0) = \frac{4(N^2-Q^2)(N^2-Q^2-2N+1)}{(2N-1)^2(2N+1)(2N-3)}, \tag{2.18}$$

For $N\to\infty$ at fixed $|Q|$, this reduces to

$$\langle G/G_0\rangle = \frac{N}{2}-\frac{1}{4}+\frac{Q^2-1/4}{2N}+\mathcal{O}(N^{-2}), \tag{2.19}$$

$$\mathrm{Var}\,(G/G_0) = \frac{1}{4}-\frac{Q^2-1/4}{2N^2}+\mathcal{O}(N^{-3}). \tag{2.20}$$

The reduction of the average conductance below the classical value $NG_0/2 = Ne^2/h$ is a weak localization effect, produced by the chiral symmetry in class BDI. (It is absent for the class-D circular ensemble [7, 12].) The variance of the conductance in the large-N limit, $\mathrm{Var}\,G \to (e^2/h)^2$, is twice as large as without chiral symmetry.

A fundamental effect of chiral symmetry is that the Q-dependence of moments of the conductance is perturbative in $1/N$. In the class-D circular ensemble, in contrast, the p-th moment of the conductance is strictly independent of the topological quantum number for $N > p$, so topological signatures cannot be studied in perturbation theory [12].

2.4 Results for a microscopic model

We study a model Hamiltonian of a disordered two-dimensional semiconductor nanowire with induced superconductivity [98, 117],

$$\begin{aligned} H = {} & \left(\frac{|\boldsymbol{p}|^2}{2m_{\mathrm{eff}}}+U(\boldsymbol{r})-\mu\right)\tau_z + V_Z\sigma_x\tau_z \\ & + \frac{\alpha_{\mathrm{so}}}{\hbar}(p_x\sigma_y\tau_z - p_y\sigma_x) + \Delta_0\sigma_y\tau_y. \end{aligned} \tag{2.21}$$

This Bogoliubov-de Gennes Hamiltonian contains the single-particle kinetic energy $(p_x^2+p_y^2)/2m_{\mathrm{eff}}$, electrostatic disorder potential $U(x,y)$, chemical potential μ, Zeeman energy V_{Z}, Rashba spin-orbit coupling constant α_{so}, and s-wave pairing potential Δ_0. The Pauli matrices σ_i, τ_i act on the spin and electron-hole degree of freedom, respectively. The two-dimensional wire has width W in the y-direction and extends along the x-direction (parallel to the Zeeman field). We define the spin-orbit coupling length $l_{\rm so} = \hbar^2 (m_{\rm eff}\alpha_{\rm so})^{-1}$ and confinement energy $E_W = \hbar^2 (2m_{\rm eff}W^2)^{-1}$.

2.4.1 Mechanisms for chiral symmetry breaking

Electron-hole symmetry and chiral symmetry,

$$\tau_x H \tau_x = \begin{cases} -H^* & \text{(e-h symmetry)}, \\ -H & \text{(chiral symmetry)}, \end{cases} \tag{2.22}$$

together require that H is real. While the electron-hole symmetry is an exact symmetry of the Hamiltonian (2.21), the chiral symmetry is broken by the spin-orbit term $p_y\sigma_x$ associated with transverse motion [166].

To quantify the stability of multiple zero-energy states, we follow Ref. [147] and make a unitary transformation $H \mapsto \mathcal{U}^\dagger H \mathcal{U} \equiv H'$ with $\mathcal{U} = \exp(i\sigma_x\tau_z\, y/l_{\rm so})$. The transformed Hamiltonian,

$$\begin{aligned} H' = {} & \left(\frac{|\boldsymbol{p}|^2}{2m_{\rm eff}} + U - \frac{\alpha_{\rm so}}{2l_{\rm so}} - \mu\right)\tau_z + V_Z\sigma_x\tau_z + \Delta_0\sigma_y\tau_y \\ & + \frac{\alpha_{\rm so}}{\hbar}p_x[\cos(2y/l_{\rm so})\sigma_y\tau_z + \sin(2y/l_{\rm so})\sigma_z], \end{aligned} \tag{2.23}$$

no longer contains p_y and breaks chiral symmetry through the final term $\propto p_x\sigma_z$. For $W \ll l_{\rm so}$ this term produces a splitting δE of pairs of zero-energy states of order $(W/l_{\rm so})E_{\rm gap}$, with $E_{\rm gap} \propto \alpha_{\rm so}$ the induced superconducting gap. This simple estimate is an upper bound on the splitting, even smaller splittings have been found in Refs. [88, 125, 134]. We typically find in our numerical simulations that $\delta E \lesssim 0.05\, E_{\rm gap}$ for $W \lesssim l_{\rm so}$.

There are other methods to break chiral symmetry. An externally controllable method is to tilt the magnetic field so that it acquires a nonzero component in the y-direction, in the plane of the substrate but perpendicular to the axis of the nanowire [165], The orbital effect of a magnetic field (Lorentz force) also breaks chiral symmetry, but this is expected to be small compared to the Zeeman effect on the spin. Subband-mixing by a disorder potential or a position-dependent pairing term preserve chiral symmetry. This leaves spin-orbit coupling of transverse momentum as the most significant intrinsic mechanism for chiral symmetry breaking and we will focus on it in the simulations. We find a transition from symmetry class D ($Q \in \mathbb{Z}_2$) to class BDI ($Q \in \mathbb{Z}$) if W drops below $l_{\rm so}$.

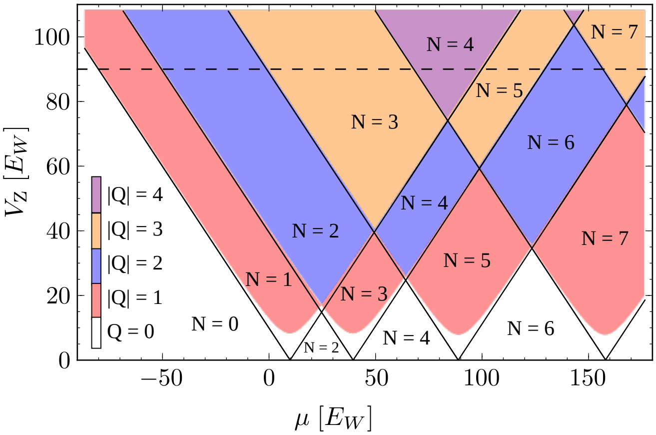

Figure 2.3. Topological phase diagram of the Hamiltonian (2.21) without disorder ($U \equiv 0$) and without any chiral symmetry breaking ($\alpha p_y \sigma_x \equiv 0$, symmetry class BDI). The colored regions give the value of the topological quantum number Q in the superconducting state ($\Delta_0 = 8E_W$), while the black lines separate regions with different number of propagating modes N in the normal state ($\Delta_0 = 0$). The topological phase boundaries are independent of E_{so}. The blue line is referred to in Fig. 2.4.

All these considerations apply to noninteracting quasiparticles. Interactions have the effect of restricting Q to $\mathbb{Z}_8$, so chiral symmetry can stabilize at most 8 zero-modes at each end of the wire [54, 99]. For $N \leq 8$ we expect the universal class BDI results (in particular the conductance quantization) to be unaffected by interactions.

2.4.2 Class BDI phase diagram

For an infinite clean wire with exact chiral symmetry, Fig. 2.3 shows the phases with different topological quantum number $Q \in \mathbb{Z}$ as a function of Zeeman energy and chemical potential. (A similar phase diagram is given in Ref. [165].) The phase boundaries are determined from the Hamiltonian (2.21) by setting $\alpha p_y \sigma_x \equiv 0$, $U \equiv 0$, and demanding that the excitation gap vanishes. This happens at

$$\begin{aligned} &p_x = 0, \quad p_y = p_n = n\pi\hbar/W, \quad n = 1, 2, \dots N, \\ &V_Z^2 = \Delta_0^2 + (\mu - p_n^2/2m_{\text{eff}})^2, \end{aligned} \tag{2.24}$$

with N the number of propagating modes in the normal state ($\Delta_0 = 0$).

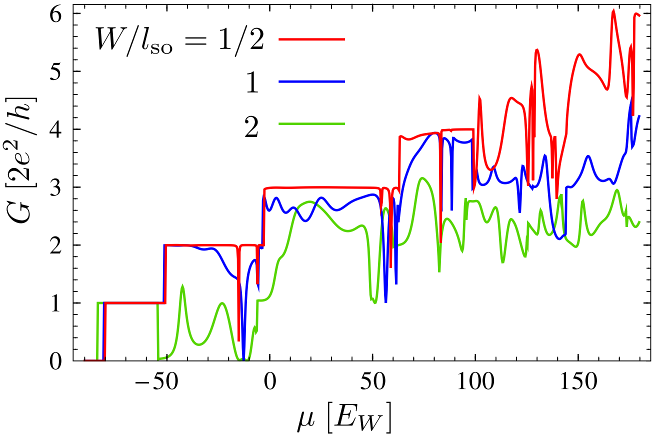

Figure 2.4. Conductance of a disordered NS junction, calculated numerically from the model Hamiltonian (2.21). The chemical potential μ is increased at constant $V_{\mathrm{Z}} = 90\,E_W$, $\Delta_0 = 8E_W$ (dashed line in the BDI phase diagram of Fig. 2.3), for three different values of the spin-orbit coupling length l_{so}. Each curve is for a single disorder realization (of strength $U_0 = 180\,E_W$). The conductance quantization at $2, 3, 4 \times 2e^2/h$ is lost by chiral symmetry breaking as W becomes larger than l_{so}.

If one follows the sequence of Q, N values with increasing μ at constant V_{Z}, one sees that $|Q|$ remains equal to $N \geq 1$ for a range of chemical potentials $(\mu - \pi^2 E_W)^2 \lesssim V_{\mathrm{Z}}^2$. For example, the sequence along the dashed line is $(|Q|, N) = (1,1), (2,2), (3,3), (4,4), \ldots$. In view of the inequality (2.9), this implies a sequence of $2e^2/h$ conductance steps. The first quantized conductance plateau emerges when the Zeeman energy exceeds the superconducting gap ($V_Z > \Delta_0$). Additional plateaus form at fields, for which the Zeeman energy becomes larger than the subband splitting. More specifically, the n-th conductance plateau appears for $V_Z^2 = \Delta_0^2 + E_W^2 \pi^4 (n^2 - 1)^2/4$ ($n = 1, 2, 3, \ldots$).

2.4.3 Conductance quantization

To demonstrate the conductance quantization we attach a clean normal-metal lead at $x = 0$ to the disordered superconducting wire. For $x < 0$ we thus set $\Delta_0 = 0$ and $U = 0$. The Andreev reflection matrix is calculated numerically by discretizing the Hamiltonian on a square lattice (lattice constant $a = W/20$). Disorder is realized by an electrostatic potential $U(x, y)$ that varies randomly from site to site for $x > 0$, distributed uniformly in the interval $(-U_0, U_0)$.

The results in Fig. 2.4 clearly show the expected behavior: For $W = l_{\rm so}/2$ the conductance increases in a sequence of quantized steps, insensitive to disorder, as long as $|Q| \in \{N, N-1\}$. The quantization at $|Q| \geq 2$ is lost for $W = 2l_{\rm so}$ because of chiral symmetry breaking. The very first step $G = 2e^2/h$ is common to both symmetry classes D and BDI, so it persists.

2.4.4 Conductance distribution

For $|Q| \leq N-2$ there is no conductance quantization, but we can still search for the Q-dependence in the statistical distribution of the conductance. In Fig. 2.5 we show the distribution function for $N = 4$, $|Q| = 0, 1, 2$, calculated by averaging the results of the numerical simulation over disorder realizations. The parameters used are listed in the caption. The values of the Fermi energy (μ_N in the normal region and μ_S in the superconducting region) were chosen in order to be far from boundaries where Q or N changes.

We found that the conductance distributions depend sensitively on the disorder strength, demonstrating that the scattering at the NS interface is diffusive rather than chaotic. This is as expected, since chaotic scattering requires a confined geometry (for example, a quantum dot), to fully mix the scattering channels. Still, by adjusting the disorder strength U_0 a quite good agreement could be obtained with the distribution from the class BDI circular ensemble calculated in Sec. 2.3.2. Since this is a single fit parameter for an entire distribution function, we find the agreement with the circular ensemble quite satisfactory.

2.5 Conclusion

In conclusion, we have developed a scattering theory for superconducting nanowires with chiral symmetry (symmetry class BDI), relating the electrical conductance G to the topological quantum number $Q \in \mathbb{Z}$. In a closed system $|Q|$ counts the number of Majorana zero-modes at the end of the wire, but in our open system these end states have broadened into a continuum with other nontopological states. Still, the value of $|Q|$ manifests itself in the conductance as a quantization $G = |Q| \times 2e^2/h$ over a range of chemical potentials (see Fig. 2.4).

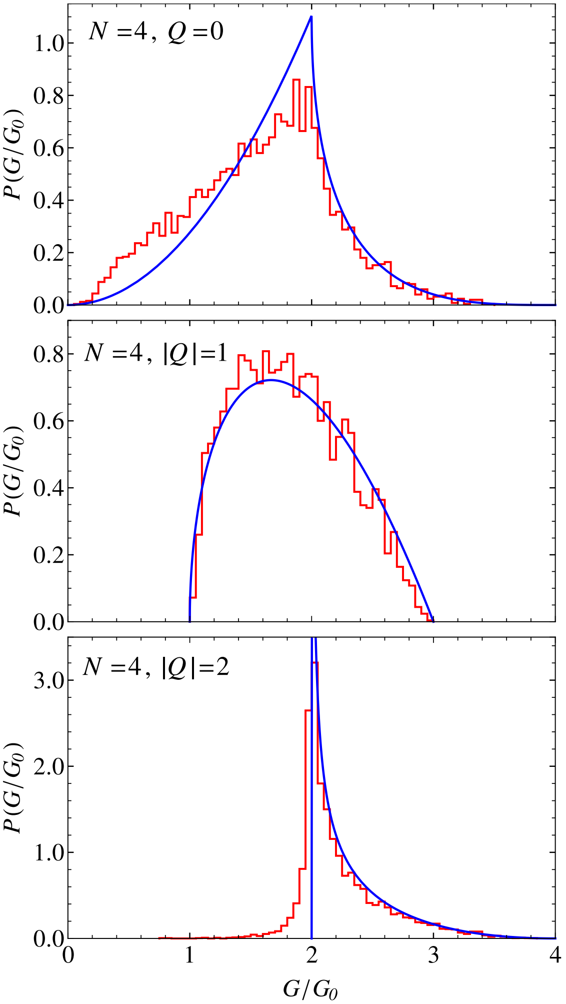

Figure 2.5. Red histograms: probability distribution of the conductance of the NS junction, calculated from the model Hamiltonian (2.21) in an ensemble of disorder realizations. Each panel has the same number of modes $N = 4$ in the normal region and a different topological quantum number $|Q| = 0, 1, 2$ in the superconductor. The blue curves are the corresponding distributions in the class BDI circular ensemble, given by Eq. (2.16d). Each panel has the same value of $l_{\text{so}} = 2W$ and $\Delta_0 = 8E_W$. The other energy scales (in units of E_W) are as follows: $\boldsymbol{Q = 0}$: $\mu_N = \mu_S = 64$, $V_{\text{Z}} = 14$, $U_0 = 180$; $\boldsymbol{|Q| = 1}$: $\mu_N = 64$, $\mu_S = 88$, $V_{\text{Z}} = 14$, $U_0 = 180$; $\boldsymbol{|Q| = 2}$: $\mu_N = \mu_S = 64$, $V_{\text{Z}} = 34$, $U_0 = 140$.

More generally, even when G is not quantized, the conductance distribution is sensitive to the value of $|Q|$, as we calculated in the circular ensemble of random-matrix theory (see Fig. 2.5). Comparison with Ref. [12], where the conductance distribution was calculated in the absence of chiral symmetry (symmetry class D with $Q \in \mathbb{Z}_2$), shows that chiral symmetry manifests itself even when $|Q| \leq 1$ — so even if there is not more than a single Majorana zero-mode.

The chiral symmetry is an approximate symmetry (unlike the fundamental electron-hole symmetry), requiring in particular a wire width W below the spin-orbit coupling length $l_{\rm so}$. Our model calculations in Fig. 2.4 show that chiral symmetry is lost for $W \gtrsim 2l_{\rm so}$ and well preserved for $W \lesssim l_{\rm so}/2$. Existing experiments [109, 47, 43] on InAs and InSb nanowires typically have $l_{\rm so} \simeq 200\,{\rm nm}$ and $W \simeq 100\,{\rm nm}$. These are therefore in the chiral regime and can support more than a single zero-mode at each end, once the Zeeman energy becomes comparable to the subband spacing.

2.6 Appendix

2.6.1 Calculation of the Andreev reflection eigenvalue distribution in the BDI circular ensemble

In this Appendix we derive the probability distribution $P(\{R_m\})$ of the Béri degenerate Andreev reflection eigenvalues $R_1, \ldots, R_M$ in the circular ensemble of symmetry class BDI (circular chiral orthogonal ensemble). The calculation follows the standard procedure of random-matrix theory [58], and is technically similar to the calculation for symmetry class D (circular real ensemble) presented in Ref. [12].

The probability distribution $P(\{R_m\})$ is determined by the invariant (Haar) measure $d\mu(r) = r^\dagger dr = \delta r$, which for a given topological quantum number Q characterizes the uniform distribution of scattering matrices in the circular ensemble subject to the symmetry constraints of Eq. (2.5). Since any scattering matrix in the ensemble can be decomposed according to Eq. (2.11), i.e. parameterized in terms of the angles α_m, we can transform the invariant measure into $d\mu(r) = J \prod_i dp_i \prod_m d\alpha_m$. The p_i's denote the degrees of freedom of the matrix of eigenvectors U and J is the Jacobian of the transformation. From this expression the distribution of the angles α_m follows via integration over the p_i's. Up to a normalization constant we have

$$P(\{\alpha_m\}) \propto \int J \prod_i dp_i \,. \tag{2.25}$$

The polar decomposition in Eq. (2.11) is not unique. As in Ref. [12] the redundant degrees of freedom can be removed by restricting the independent parameters p_i in the matrix of eigenvectors U. The total number of degrees of freedom furthermore depends on N as well as on Q. This is best seen if one considers the reflection matrix $\tilde{r}$ in a basis where it is a real orthogonal and symmetric matrix, of the form

$$\tilde{r} = O \begin{pmatrix} \mathbb{1}_{N+Q} & 0 \\ 0 & -\mathbb{1}_{N-Q} \end{pmatrix} O^T, \tag{2.26}$$

with O a $2N \times 2\mathrm{N}$ real orthogonal matrix. In this basis the topological quantum number is given by $Q = \frac{1}{2} \operatorname{Tr} \tilde{r}$. The upper-left and lower-right blocks do not change under an additional orthogonal transformation $O'_{N+Q} \oplus O''_{N-Q}$. Group division readily gives the total number of degrees of freedom: $\dim O(2N) - \dim O(N+Q) - \dim O(N-Q) = N^2 - Q^2$.

Since there are M angular parameters α_m, there must be $N^2 - Q^2 - M$ independent degrees of freedom p_i in the matrix of eigenvectors U.

In order to obtain the probability distribution from Eq. (2.25) we need the Jacobian J. It can be determined from the metric tensor $g_{\mu\nu}$, which can be extracted from the trace $\operatorname{Tr}\delta r\delta r^\dagger$, when it is expressed in terms of the infinitesimals $d\alpha_m$ and dp_i (collectively denoted as dx_μ):

$$\operatorname{Tr}\delta r\delta r^\dagger = \sum_{\mu,\,\nu} g_{\mu\nu} dx_\mu dx_\nu \,. \tag{2.27}$$

In view of the polar decomposition (2.11) one has

$$W^\dagger dr W^* = \delta W L + dL + L\delta W^T, \tag{2.28}$$

where we abbreviated

$$W = \begin{pmatrix} U & 0 \\ 0 & U^* \end{pmatrix}, \quad L = \begin{pmatrix} \Gamma & \Lambda \\ \Lambda^T & \Gamma \end{pmatrix} . \tag{2.29}$$

Unitarity ensures $0 = d(U^\dagger U) = dU^\dagger U + U^\dagger dU \Rightarrow \delta U^\dagger = -\delta U$. Substitution of Eqs. (2.28) and (2.29) into $\operatorname{Tr}\delta r\delta r^\dagger = \operatorname{Tr} dr dr^\dagger = \operatorname{Tr}(W^\dagger dr W^* W^T dr^\dagger W)$ gives

$$\operatorname{Tr}\delta r\delta r^\dagger = \operatorname{Tr}(dL dL^\dagger - 2L\delta W^T L^\dagger \delta W - 2\delta W^2) \,. \tag{2.30}$$

From the block structure of W and L we find $\operatorname{Tr}\delta W^2 = 2\operatorname{Tr}\delta U^2$ and

$$\operatorname{Tr}(L\delta W^T L^\dagger \delta W) = 2\operatorname{Tr}(\Gamma\delta U\Gamma\delta U^T - \Lambda\delta U\Lambda\delta U), \tag{2.31}$$

where we have used $\Gamma^T = \Gamma^* = \Gamma$ and $\Lambda^\dagger = \Lambda$.

It is convenient to express $\operatorname{Tr}\delta r\delta r^\dagger$ in terms of the form $\operatorname{Tr} AA^\dagger = \sum_{ij} |A_{ij}|^2$. Using $\Gamma\Gamma + \Lambda\Lambda = \mathbb{1}_N$ we find

$$\begin{aligned}\operatorname{Tr}\delta r\delta r^\dagger &= \operatorname{Tr} dL dL^\dagger + 2\operatorname{Tr}(\Gamma\delta U^T + \delta U\Gamma)(\Gamma\delta U^T + \delta U\Gamma)^\dagger \\ &\quad + 2\operatorname{Tr}(\Lambda\delta U - \delta U\Lambda)(\Lambda\delta U - \delta U\Lambda)^\dagger \\ &\equiv T_1 + T_2 + T_3. \end{aligned} \tag{2.32}$$

The first trace simply evaluates to

$$T_1 = 2\sum_{ij=1}^{N} (|d\Gamma_{ij}|^2 + |d\Gamma_{ij}|^2) = 4\sum_{m=1}^{M} (d\alpha_m)^2 \,. \tag{2.33}$$

The remaining two traces T_2 and T_3 need to be calculated using the block structure of Γ and Λ in Eq. (2.12). We work out the calculation for $Q = 0$, N even ($\Rightarrow \zeta = 0$). The two matrices Λ and Γ are in this case fully described by $M = N/2$ blocks of 2×2 matrices. The two traces evaluate to

$$\begin{aligned}\tfrac{1}{4}T_2 =& \sum_{k=1}^{M} 2\cos^2\alpha_k \left\{|\delta U_{2k,2k}|^2 + |\delta U_{2k-1,2k-1}|^2 + 2\left[\mathrm{Im}\left(\delta U_{2k-1,2k}\right)\right]^2\right\} \\ &+ \sum_{k<l=1}^{M} \Big\{(\cos^2\alpha_k + \cos^2\alpha_l)(|\delta U_{2k,2l}|^2 + |\delta U_{2k,2l-1}|^2 + |\delta U_{2k-1,2l}|^2 \\ &\qquad +|\delta U_{2k-1,2l-1}|^2) - 2\cos\alpha_l\cos\alpha_k\,\mathrm{Re}\left(\delta U^2_{2l,2k} + \delta U^2_{2l,2k-1}\right. \\ &\qquad \left. +\delta U^2_{2l-1,2k} + \delta U^2_{2l-1,2k-1}\right)\Big\}\,, \end{aligned} \tag{2.34}$$

$$\begin{aligned}\tfrac{1}{4}T_3 =& \sum_{k=1}^{M} \sin^2\alpha_k \left\{|\delta U_{2k,2k} - \delta U_{2k-1,2k-1}|^2 + 4\left[\mathrm{Im}\left(\delta U_{2k-1,2k}\right)\right]^2\right\} \\ &+ \sum_{k<l=1}^{M} \Big\{(\sin^2\alpha_k + \sin^2\alpha_l)\left(|\delta U_{2k,2l}|^2 + |\delta U_{2k,2l-1}|^2 + |\delta U_{2k-1,2l}|^2\right. \\ &\qquad \left.+|\delta U_{2k-1,2l-1}|^2\right) + 4\sin\alpha_k\sin\alpha_l\,\mathrm{Re}\left(\delta U_{2k,2l-1}\delta U^*_{2k-1,2l}\right. \\ &\qquad \left.-\delta U_{2k,2l}\delta U^*_{2k-1,2l-1}\right)\Big\}\,. \end{aligned} \tag{2.35}$$

Like Γ and Λ the elements of the matrix δU can be grouped into separate 2×2 blocks, denoted by the block indices $k, l = 1, \ldots, M$. We first consider the block-off-diagonal part for which we can choose as independent parameters

$$\delta U_{2k,2l},\ \delta U_{2k,2l-1},\ \delta U_{2k-1,2l},\ \delta U_{2k-1,2l-1},$$

with $1 \leq k < l \leq M$. The real and imaginary parts, denoted by $\delta U^{\mathrm{R}}, \delta U^{\mathrm{I}}$, produce a total of $4M(M-1)$ independent parameters. Note that $\delta U^\dagger = -\delta U$ immediately implies $\delta U^{\mathrm{R}}_{2k,2l} = -\delta U^{\mathrm{R}}_{2l,2k}$, $\delta U^{\mathrm{I}}_{2k,2l} = \delta U^{\mathrm{I}}_{2l,2k}$, and so on.

For given values of k and l the contribution to $\mathrm{Tr}\,\delta r \delta r^\dagger$ has the form

$$\begin{aligned}
&a\Big[(\delta U^{\mathrm{R}}_{2k,2l})^2+(\delta U^{\mathrm{R}}_{2k,2l-1})^2+(\delta U^{\mathrm{R}}_{2k-1,2l})^2+(\delta U^{\mathrm{R}}_{2k-1,2l-1})^2\Big] \\
&+ b\Big[(\delta U^{\mathrm{I}}_{2k,2l})^2+(\delta U^{\mathrm{I}}_{2k,2l-1})^2+(\delta U^{\mathrm{I}}_{2k-1,2l})^2+(\delta U^{\mathrm{I}}_{2k-1,2l-1})^2\Big] \\
&+ 2c\Big[\delta U^{\mathrm{R}}_{2k,2l-1}\delta U^{\mathrm{R}}_{2k-1,2l} + \delta U^{\mathrm{I}}_{2k,2l-1}\delta U^{\mathrm{I}}_{2k-1,2l} - \delta U^{\mathrm{R}}_{2k,2l}\delta U^{\mathrm{R}}_{2k-1,2l-1} \\
&\qquad - \delta U^{\mathrm{I}}_{2k,2l}\delta U^{\mathrm{I}}_{2k-1,2l-1}\Big]\,,
\end{aligned}$$

where we abbreviated $a = 2(1 - \cos\alpha_k \cos\alpha_l)$, $b = 2(1 + \cos\alpha_k \cos\alpha_l)$, and $c = 2\sin\alpha_k \sin\alpha_l$.

The contribution to the metric tensor is a block matrix

$$\begin{pmatrix} a & -c & 0 & 0 \\ -c & a & 0 & 0 \\ 0 & 0 & a & c \\ 0 & 0 & c & a \end{pmatrix} \oplus \begin{pmatrix} b & -c & 0 & 0 \\ -c & b & 0 & 0 \\ 0 & 0 & b & c \\ 0 & 0 & c & b \end{pmatrix}\,,$$

where the first and the second block correspond to the real and imaginary parts, respectively. The determinant of this block matrix is $256\,(\sin^2\alpha_k - \sin^2\alpha_l)^4$. This gives us the contribution to the Jacobian from the off-diagonal matrix elements

$$J_{\text{off-diagonal}} = \prod_{k<l=1}^{M} (\sin^2\alpha_k - \sin^2\alpha_l)^2. \tag{2.36}$$

Next we consider the diagonal 2×2 blocks. Anti-Hermiticity of δU implies $\delta U^{\mathrm{R}}_{ii} = 0$ $(i = 1, \ldots, N)$. We choose the $3M$ independent parameters

$$\delta U^{\mathrm{I}}_{2k,2k}, \quad \delta U^{\mathrm{I}}_{2k-1,2k-1}, \quad \delta U^{\mathrm{I}}_{2k-1,2k}\,.$$

The contribution to $\mathrm{Tr}\,\delta r \delta r^\dagger$ for a given value k has the form

$$\begin{aligned}
&v\Big[(\delta U^{\mathrm{I}}_{2k,2k})^2 + (\delta U^{\mathrm{I}}_{2k-1,2k-1})^2\Big] \\
&- 2w\delta U^{\mathrm{I}}_{2k,2k}\delta U^{\mathrm{I}}_{2k-1,2k-1} + 4(\delta U^{\mathrm{I}}_{2k-1,2k})^2\,,
\end{aligned}$$

where $v = 1 + \cos^2\alpha_k$ and $w = \sin^2\alpha_k$. Note that $\delta U^{\mathrm{I}}_{2k-1,2k}$ is fully decoupled. The contribution to the metric tensor is

$$\begin{pmatrix} v & -w \\ -w & v \end{pmatrix}$$

with a determinant of $4\cos^2\alpha_k$. This leads to a contribution to the Jacobian from the diagonal matrix elements

$$J_{\text{diagonal}} = \prod_{k=1}^{M}(1-\sin^2\alpha_k)^{1/2}\ . \tag{2.37}$$

The total number of independent parameters that we have accounted for is $4M^2 = N^2$ (including the M angular parameters α_m). This is exactly the number we expect for N even and $Q = 0$. Collecting all the terms that contribute to the Jacobian in Eq. (2.25), we obtain the probability distribution

$$P(\alpha_k) \propto \prod_{k=1}^{M}(1-\sin^2\alpha_k)^{1/2}\prod_{k<l=1}^{M}(\sin^2\alpha_k - \sin^2\alpha_l)^2. \tag{2.38}$$

Integration over the $N^2 - |Q|^2 - M$ ancillary degrees of freedom of the matrix of eigenvectors U only gives rise to an overall constant. A transformation of variables from α_m to $R_m = \sin^2\alpha_m$ gives the distribution (2.13) of the twofold degenerate Andreev reflection values in the case $Q = 0$, N even ($\zeta = 0$). The cases $Q \neq 0$ and/or N odd are worked out similarly.

2.6.2 Average conductance in the BDI circular ensemble

In the circular ensemble of Sec. 2.3.2 the $2N \times 2N$ reflection matrix r is uniformly distributed in the unitary group, subject to the restrictions of electron-hole symmetry and chiral symmetry. The average conductance can be calculated directly by integration over the unitary group. We give this calculation here, as a check on the result (2.17) derived by going through the distribution of Andreev reflection eigenvalues.

Unitarity ($rr^\dagger = 1$) implies that the expression (2.1) for the conductance can be written equivalently as

$$\begin{aligned} G &= \tfrac{1}{4}G_0\,\mathrm{Tr}\,(1 + r_{\text{he}}r_{\text{he}}^\dagger + r_{\text{eh}}r_{\text{eh}}^\dagger - r_{\text{ee}}r_{\text{ee}}^\dagger - r_{\text{hh}}r_{\text{hh}}^\dagger) \\ &= \tfrac{1}{4}G_0\,\mathrm{Tr}\,(1 - \tau_z r \tau_z r^\dagger). \end{aligned} \tag{2.39}$$

Electron-hole symmetry ($r = \tau_x r^* \tau_x$) and chiral symmetry ($r = r^T$) constrain r to the form

$$r = -ie^{i\tau_x\pi/4}O\mathcal{D}_Q O^T e^{i\tau_x\pi/4}. \tag{2.40}$$

The matrix O is real orthogonal ($OO^T = 1$). The diagonal matrix $\mathcal{D}_Q$ has entries ±1 on the diagonal with $\mathrm{Tr}\,\mathcal{D}_Q = 2Q$, consistent with Eq. (2.6). Substitution into Eq. (2.39) gives

$$G = \tfrac{1}{4}G_0\,\mathrm{Tr}\,\big(1 + \tau_y O\mathcal{D}_Q O^T \tau_y O\mathcal{D}_Q O^T\big). \tag{2.41}$$

In the circular ensemble the matrix O is uniformly distributed with respect to the Haar measure for $2N\times 2N$ orthogonal matrices. The average of a product of four orthogonal matrices equals [41]

$$\begin{aligned}
&\langle O_{\alpha a}O_{\beta b}O_{\gamma c}O_{\delta d}\rangle = \\
&\quad \frac{2N+1}{2N(2N-1)(2N+2)}\big(\delta_{\alpha\beta}\delta_{ab}\delta_{\gamma\delta}\delta_{cd} + \delta_{\alpha\gamma}\delta_{ac}\delta_{\beta\delta}\delta_{bd} + \delta_{\alpha\delta}\delta_{ad}\delta_{\beta\gamma}\delta_{bc}\big) \\
&\quad - \frac{1}{2N(2N-1)(2N+2)}\big(\delta_{\alpha\beta}\delta_{ac}\delta_{\gamma\delta}\delta_{bd} + \delta_{\alpha\beta}\delta_{ad}\delta_{\gamma\delta}\delta_{bc} + \delta_{\alpha\gamma}\delta_{ab}\delta_{\beta\delta}\delta_{cd} \\
&\qquad + \delta_{\alpha\gamma}\delta_{ad}\delta_{\beta\delta}\delta_{bc} + \delta_{\alpha\delta}\delta_{ab}\delta_{\beta\gamma}\delta_{cd} + \delta_{\alpha\delta}\delta_{ac}\delta_{\beta\gamma}\delta_{bd}\big).
\end{aligned} \tag{2.42}$$

The average of Eq. (2.39) becomes

$$\langle G\rangle = \tfrac{1}{4}G_0\left(2N + \frac{4Q^2 - 2N}{2N-1}\right), \tag{2.43}$$

which is just Eq. (2.17).

Chapter 3

Phase-locked magnetoconductance oscillations as a probe of Majorana edge states

3.1 Introduction

Two-dimensional superconductors can support propagating edge states that are not localized by disorder for topological reasons [177, 149, 130], as a superconducting analogue of the metallic edge states in the quantum Hall effect or quantum spin-Hall effect [73, 127]. Unlike the dispersionless "flat band" edge states of nodal superconductors [84], which leave a strong signature in the density of states, the propagating edge states have not yet been observed. They have been predicted in a variety of materials — including strontium ruthenate [100], heavily doped graphene [114], and topological insulators on a superconducting substrate [61].

The symmetry-based classification of topological superconductors lists three types of propagating edge states [138]: chiral Dirac modes, and chiral or helical Majorana modes (see Table 3.1). A spin-singlet superconductor with $d_{x^2-y^2} + id_{xy}$ orbital pairing supports edge states that propagate in one direction only (chiral) and are not selfconjugate (Dirac fermions). For spin-triplet $p_x + ip_y$ pairing the edge states are chiral and selfconjugate (Majorana fermions). Counterpropagating (helical) Majorana modes are also stable against localization [126, 161, 143], unlike counterpropagating

pair potential	edge state	symmetry class
singlet, $d_{x^2-y^2}+id_{xy}$	chiral Dirac	C
triplet, p_x+ip_y	chiral Majorana	D
triplet, $p_x \pm ip_y$	helical Majorana	DIII

Table 3.1. The three types of propagating edge states in a two-dimensional topological superconductor.

Dirac modes.

The topological protection allows for correlations in the electrical current measured at distant points on the boundary connected by an edge state [94, 151, 40, 97, 159, 96, 17]. For example, in an early study of this type, Law, Lee, and Ng considered a superconducting disc deposited on the surface of a three-dimensional topological insulator [94]. A chiral Majorana mode is confined to the perimeter of the disc, when the surface outside the superconductor is gapped by a ferromagnet [61]. Two point contacts attached to the perimeter measure a correlated current, mediated by the circulating edge state, and dependent on the number of magnetic vortices inside the disc. It is essential that the contacts share a boundary. If the disc would be replaced by a ring, with one contact at the inner and one at the outer perimeter, then there would be no correlations.

Here we revisit this problem of edge-state mediated correlations in a superconducting ring, to show that the physics changes qualitatively if the ring contains a weak link forming a Josephson junction (see Fig. 3.1). The weak link is a one-dimensional subsystem of the two-dimensional topological superconductor, with its own topological phase transition [163]. Since magnetic flux Φ can enter into the ring along the junction, there is no flux quantization and we can ask for the Φ-dependence of the conductances G_1 and G_2 measured between the grounded superconductor and either the inner or the outer perimeter. Dirac and Majorana modes both produce h/e-periodic oscillations in the conductances, but only Majorana modes can correlate the oscillations in G_1 and G_2. The mechanism by which the inner and outer perimeter communicate is a closing of the excitation gap when the Josephson junction undergoes a one-dimensional topological phase transition. The same conclusion was reached recently by Wieder, Zhang, and Kane [183].

The outline of the paper is as follows. In the next section we formulate the scattering problem of Andreev reflection from the perimeter of a super-

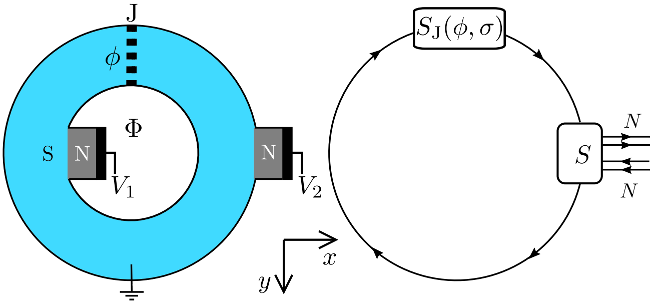

Figure 3.1. *Left panel:* Superconducting ring (S) containing a weak link (J), forming a flux-biased Josephson junction. A current can be injected into the grounded superconductor from a voltage-biased normal-metal (N) contact at the inner or outer perimeter. The Andreev conductance $G_n = I/V_n$ is the ratio of the current-to-ground I and the applied voltage V_n to contact $n = 1, 2$ (with $V = 0$ for the other contact). *Right panel:* Scattering processes at the outer perimeter, involving the coupling of a chiral edge state to $2N$ incoming and $2N$ outgoing electron-hole modes at the normal metal. This coupling introduces a dependence of the conductance on the phase difference $\phi = (2e/\hbar)\Phi$ across the Josephson junction and on its topological quantum number σ.

conducting ring, to obtain a general formula for the electrical conductance. The conductance $G(\Phi, \sigma)$ depends in general both on the enclosed flux Φ and on the $\mathbb{Z}_2$ topological quantum number σ of the Josephson junction. A topological phase transition switches σ between $+1$ and -1, resulting in a jump δG of the conductance. In Sec. 3.3 we calculate the probability distribution $P(\delta G)$ in an ensemble of disordered rings, using the method of random-matrix theory. These are model-independent results, which take as input only the symmetry class of the topological superconductor. We then turn, in Sec. 4.2, to specific model Hamiltonians in each symmetry class. The numerical results for these models are discussed in Sec. 3.5 to arrive at a set of experimentally observable signatures of (1) the presence of circulating edge states and (2) their Majorana or Dirac fermionic nature.

3.2 Scattering formula for the conductance

We formulate the scattering problem for a superconducting ring interrupted by a Josephson junction, enclosing a magnetic flux Φ. The ring is contacted at the inner or outer perimeter by a normal-metal electrode.

Far away from any gap closings there is no transmission between the inner and outer perimeter, so we can treat these two scattering problems independently. We calculate the Andreev conductance G between the normal metal (N) and the (grounded) superconductor (S). An h/e-periodic flux dependence of the conductance serves as a signature of edge states circulating along the ring.

As illustrated in Fig. 3.1, the NS interface is described by a scattering matrix S, with submatrices $r_{\rm N}$ (reflection back into the normal metal), $t_{\rm edge,N}$, $t_{\rm N,edge}$ (transmission from the normal metal into an edge state, and vice versa), and $t_{\rm edge}$ (transmission along an edge state without entering the normal metal):

$$S = \begin{pmatrix} r_{\rm N} & t_{\rm N,edge} \\ t_{\rm edge,N} & t_{\rm edge} \end{pmatrix}. \tag{3.1}$$

Incoming and outgoing wave amplitudes at the NS interface are related by

$$a_{\rm N}^{\rm out} = r_{\rm N} a_{\rm N}^{\rm in} + t_{\rm N,edge} a_{\rm edge}^{\rm in} \tag{3.2}$$

$$a_{\rm edge}^{\rm out} = t_{\rm edge,N} a_{\rm N}^{\rm in} + t_{\rm edge} a_{\rm edge}^{\rm in}. \tag{3.3}$$

The scattering matrix $S_{\rm J}$ of the Josephson junction describes how the edge states return back to the NS interface after encircling the ring,

$$a_{\rm edge}^{\rm in} = S_{\rm J} a_{\rm edge}^{\rm out}. \tag{3.4}$$

Elimination of the edge state amplitudes gives the relation $a_{\rm N}^{\rm out} = R a_{\rm N}^{\rm in}$, with the effective reflection matrix of the NS interface,

$$R = r_{\rm N} + t_{\rm N,edge}(1 - S_{\rm J} t_{\rm edge})^{-1} S_{\rm J} t_{\rm edge,N}. \tag{3.5}$$

The matrix R is unitary, $RR^\dagger = 1$, with electron and hole submatrices,

$$R = \begin{pmatrix} R_{\rm ee} & R_{\rm eh} \\ R_{\rm he} & R_{\rm hh} \end{pmatrix}, \tag{3.6}$$

describing normal reflection (from electron to electron or from hole to hole) and Andreev reflection (from electron to hole or vice versa). The linear response conductance (in the zero-temperature limit) is given by

$$G = G_0 \, {\rm Tr}\, (1 - R_{\rm ee} R_{\rm ee}^\dagger + R_{\rm he} R_{\rm he}^\dagger) = 2G_0 \, {\rm Tr}\, R_{\rm he} R_{\rm he}^\dagger, \tag{3.7}$$

with $G_0 = e^2/h$ the conductance quantum. It it convenient to rewrite this without reference to the submatrices,

$$G/G_0 = \tfrac{1}{2}\,\mathrm{Tr}\,(1 - R\tau_z R^\dagger \tau_z), \quad \tau_z = \begin{pmatrix} 1 & 0 \\ 0 & -1 \end{pmatrix}. \tag{3.8}$$

The Pauli matrix τ_z acts on the electron and hole degrees of freedom.

The edge channels of a spin-triplet p-wave superconductor are self-conjugate Majorana modes. It is then useful, following Refs. [151, 96], to transform from the electron-hole basis to the Majorana basis,

$$R \mapsto \mathcal{U} R \mathcal{U}^\dagger, \quad \mathcal{U} = \sqrt{\frac{1}{2}} \begin{pmatrix} 1 & 1 \\ -i & i \end{pmatrix}. \tag{3.9}$$

Electron-hole symmetry at the Fermi level requires that the scattering matrix elements are real in the Majorana basis, so $R^\dagger = R^{\mathrm{T}} = R^{-1}$. Because the Pauli matrix τ_z transforms into $\mathcal{U}\tau_z\mathcal{U}^\dagger = -\tau_y$, the conductance is given by

$$G/G_0 = \tfrac{1}{2}\,\mathrm{Tr}\,(1 - R\tau_y R^{\mathrm{T}} \tau_y), \quad \tau_y = \begin{pmatrix} 0 & -i \\ i & 0 \end{pmatrix}. \tag{3.10}$$

In what follows we will work in the electron-hole basis (3.8) for spin-singlet d-wave pairing (when the modes are not self-conjugate) and in the Majorana basis (3.10) for spin-triplet p-wave pairing.

3.3 Random-matrix theory

The effect on the Andreev conductance of a topological phase transition at the Josephson junction can be analyzed in a model-independent way by means of random-matrix theory. We will first do this for an unpaired chiral Majorana mode and then for a pair of helical Majorana modes. The Josephson junction cannot undergo a topological phase transition for chiral Dirac modes, and will generically not for an even number of chiral Majorana modes, so these two cases are not considered in this section.

3.3.1 Chiral Majorana mode

The conductance depends on the magnetic flux in a way which is restricted by electron-hole symmetry at the Fermi level. The restrictions are most severe for an unpaired chiral Majorana mode: The only phase shift allowed by electron-hole symmetry is π (mod 2π), so the conductance remains flux independent except when the enclosed flux is $h/4e$ (mod $h/2e$). Let us investigate this case in some detail.

A single Majorana mode corresponds to scalars $S_{\rm J}$ and $t_{\rm edge}$, to a row vector $t_{\rm edge,N}$, and to a column vector $t_{\rm N,edge}$. The contraction $t_{\rm edge,N}\tau_y t^{\rm T}_{\rm edge,N}$ produces a scalar, which vanishes because τ_y is an antisymmetric matrix. This eliminates one term when we substitute Eq. (3.5) into Eq. (3.10). What remains is

$$\begin{aligned} G/G_0 = {} & \tfrac{1}{2}\,{\rm Tr}\,(1 - r_{\rm N}\tau_y r^{\rm T}_{\rm N}\tau_y) \\ & - \frac{S_{\rm J}}{1 - S_{\rm J}t_{\rm edge}} t_{\rm edge,N}\tau_y r^{\rm T}_{\rm N}\tau_y t_{\rm N,edge}. \end{aligned} \tag{3.11}$$

Because $S_{\rm J}$ is an orthogonal matrix consisting of a single matrix element, it can only equal ±1. Including a π phase shift from the winding around the ring, we define

$$\sigma = -S_{\rm J} \in \{+1, -1\} \tag{3.12}$$

as the topological quantum number of the Josephson junction. The effective reflection matrix R of the NS interface, constructed from Eq. (3.5), inherits this topological quantum number,

$$\operatorname{Det} R = \sigma. \tag{3.13}$$

This follows from general considerations for a topological quantum number in symmetry class D [3], but one can check it explicitly from Eq. (3.5).

The conductance for a ring with an unpaired Majorana mode is flux independent — except at topological phase transitions, when σ changes sign and the conductance jumps by an amount $\pm\delta G$ with

$$\delta G = G(\sigma = 1) - G(\sigma = -1). \tag{3.14}$$

Using Eq. (3.11) this can be written as

$$\delta G/G_0 = \frac{2}{1 - t^2_{\rm edge}} t_{\rm edge,N}\tau_y r^{\rm T}_{\rm N}\tau_y t_{\rm N,edge}. \tag{3.15}$$

For a disordered NS interface we may consider an ensemble of scattering matrices S, generated by varying the disorder realization. A simple choice is the circular real ensemble (CRE) of class-D random-matrix theory [151, 7, 12], for which S is uniformly distributed in $\mathrm{SO}(2N+1)$: The group of orthogonal $(2N+1)\times(2N+1)$ matrices O with $\mathrm{Det}\, O = 1$. The integer N counts the number of modes in the contact with the normal metal, including the spin degree of freedom. The factor of 2 in $2N+1$ accounts for the electron-hole degree of freedom and the $+1$ refers to the unpaired Majorana mode.

The effective reflection matrix R, constructed from S via Eq. (3.5), inherits the uniform CRE distribution in $\mathrm{O}_\sigma(2N)$ — the set of $2N \times 2N$ orthogonal matrices with determinant σ. The uniformity of $R \in \mathrm{O}_\sigma(2N)$ is a consequence of the uniformity of $S \in \mathrm{SO}(2N+1)$ because the transformation $S \mapsto S\cdot(U_0 \oplus 1)$ with $U_0 \in \mathrm{SO}(2N)$ maps R onto $R\cdot U_0$ without changing the determinant.

If $N = 1$ or $N = 2$ the distribution of δG follows directly from the known [12] distribution $P_\sigma(G)$ of the conductance in the CRE: In both these cases $P_-(G) = \delta(G - 2G_0)$ is a delta-function distribution, so we may equate $P(\delta G) = P_+(G = \delta G + 2G_0)$. Since $P_+(G) = \delta(G)$ for $N = 1$ and uniform in $[0, 4G_0]$ for $N = 2$, we arrive at

$$\begin{aligned} &P(\delta G) = \delta(\delta G + 2G_0), \quad \text{for} \quad N = 1, \\ &P(\delta G) = 1/4G_0, \quad -2G_0 \le G \le 2G_0, \quad \text{for} \quad N = 2. \end{aligned} \tag{3.16}$$

For $N > 2$ the knowledge of $P_\sigma(G)$ is not sufficient to determine $P(\delta G)$, but it can be determined directly from the uniform distribution of S in $\mathrm{SO}(2N+1)$. We have carried out this calculation numerically for small N, see Fig. 3.2.

For large N we can approximate the matrix elements of S by independent Gaussians, of zero mean and variance $1/2N$. We define the unit vectors

$$\hat{u} = \frac{it_{\mathrm{edge,N}}\tau_y}{(1 - t_{\mathrm{edge}}^2)^{1/2}}, \quad \hat{v} = \frac{i\tau_y t_{\mathrm{N,edge}}}{(1 - t_{\mathrm{edge}}^2)^{1/2}}, \tag{3.17}$$

so that the conductance change (3.15) is given by

$$\delta G/G_0 = -2 \sum_{n,m=1}^{2N} \hat{u}_n \hat{v}_m (r_{\mathrm{N}})_{mn}. \tag{3.18}$$

In the large-N Gaussian approximation, $\delta G/G_0$ is the sum of Gaussians with zero mean and variance $(2/N)(\hat{u}_n\hat{v}_m)^2$, so its distribution is

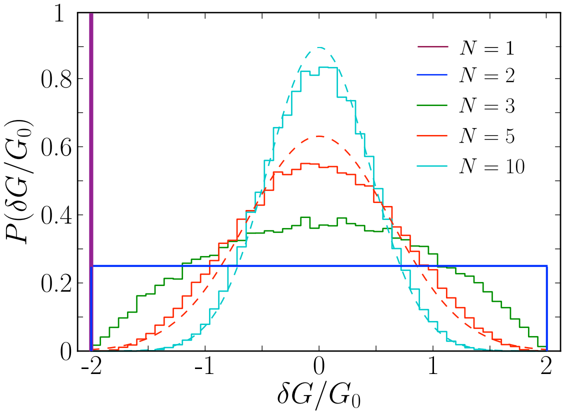

Figure 3.2. Probability distribution of the change δG in the conductance of the superconducting ring when the Josephson junction switches from topologically trivial to nontrivial. These are results from random-matrix theory in the circular real ensemble (CRE, symmetry class D), for an unpaired chiral Majorana mode circulating along the ring and N modes in the contact to the normal metal. The solid lines for $N = 1, 2$ are from Eq. (3.16), the histograms are obtained numerically by averaging the scattering matrix S uniformly over SO$(2N + 1)$, and the dashed curves are the large-N Gaussian limit (3.19).

again a Gaussian with zero mean and variance

$$\mathrm{Var}\,(\delta G/G_0) = \frac{2}{N}\sum_{n,m=1}^{2N}(\hat{u}_n\hat{v}_m)^2 = \frac{2}{N},\quad N \gg 1. \tag{3.19}$$

3.3.2 Helical Majorana modes

Spin-triplet pairing with time-reversal symmetry can produce a pair of counterpropagating (helical) Majorana modes. This is symmetry class DIII. In the Majorana basis the scattering matrix is orthogonal, as in class D, with the additional time-reversal symmetry condition [7]

$$S = \tau_y S^{\mathrm{T}} \tau_y. \tag{3.20}$$

This is equivalent to the requirement that the matrix product $\tilde{S} \equiv i\tau_y S$ is both orthogonal ($\tilde{S}^\dagger = \tilde{S}^{\mathrm{T}} = \tilde{S}^{-1}$) and antisymmetric ($\tilde{S}^{\mathrm{T}} = -\tilde{S}$). The class-DIII random-matrix ensemble (T-CRE) is generated by drawing a matrix O from the CRE and constructing

$$\tilde{S} \equiv i\tau_y S = O \cdot i\tau_y \cdot O^{\mathrm{T}},\quad O \in \mathrm{SO}(4M + 2). \tag{3.21}$$

The channel number $M = N/2$ again only refers to the orbital degree of freedom, each mode having a twofold Kramers degeneracy.

The Josephson junction breaks time-reversal symmetry, for $\phi \neq 0 \pmod{\pi}$, so it may couple the two edge states and cause backscattering at the junction. In the simplest description (not made in the numerical calculations of the next section) we neglect this coupling and set

$$S_{\rm J} = -\sigma \begin{pmatrix} 1 & 0 \\ 0 & 1 \end{pmatrix} \Rightarrow \tilde{S}_{\rm J} \equiv i\tau_y S_{\rm J} = -i\sigma\tau_y. \tag{3.22}$$

The Pfaffian of $\tilde{S}_{\rm J}$ is the class-DIII topological invariant [65],

$$\sigma = -{\rm Pf}\,\tilde{S}_{\rm J} \in \{+1, -1\}. \tag{3.23}$$

The effective reflection matrix R, constructed from S and $S_{\rm J}$ via Eq. (3.5), inherits this topological invariant,

$$\mathrm{Pf}\,(i\tau_y R) = \sigma, \tag{3.24}$$

and also inherits the uniform distribution of the T-CRE:

$$\tilde{R} \equiv i\tau_y R = O \cdot i\tau_y \cdot O^{\rm T}, \;\; O \in {\rm O}_\sigma(4M). \tag{3.25}$$

We seek the probability distribution $P(\delta G)$ of the conductance change upon a topological phase transition in the T-CRE. For $N = 2M = 2$ the known [12] probability distribution $P_\sigma(G)$ of the conductance gives sufficient information, since $P_-(G) = \delta(G - 4G_0) \Rightarrow P(\delta G) = P_+(G = \delta G + 4G_0)$, resulting in

$$P(\delta G/G_0) = \frac{1}{8\sqrt{1 + \delta G/4G_0}}, \;\; -4 \leq \delta G/G_0 \leq 0, \\ \text{for } \; N = 2. \tag{3.26}$$

The distribution $P(\delta G)$ for $M > 1$ has been obtained by generating random matrices O uniformly in ${\rm SO}(4M + 2)$ and then constructing S in the T-CRE via Eq. (3.21). Results are shown in Fig. 3.3. For $N \gg 1$ we have again a Gaussian distribution with zero mean and variance

$$\mathrm{Var}\,(\delta G/G_0) = \frac{8}{N}, \;\; N \gg 1, \tag{3.27}$$

four times larger than Eq. (3.19) because of the twofold Kramers degeneracy.

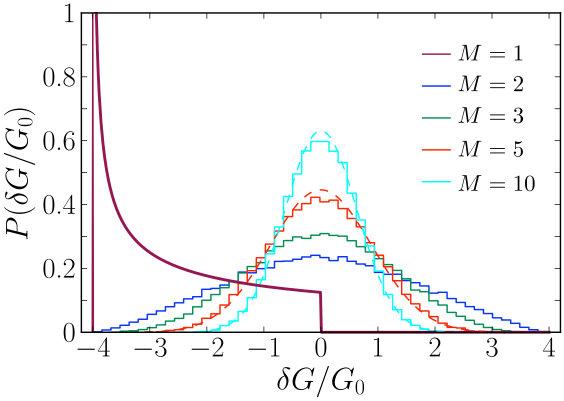

Figure 3.3. Probability distribution of the conductance change upon a topological phase transition in symmetry class DIII, involving a pair of helical Majorana modes circulating along the ring. The contact to the normal metal has M orbital modes, each with a twofold Kramers degeneracy. The results are from the time-reversally invariant circular real ensemble (T-CRE) of random-matrix theory. The solid line for $M = 1$ is from Eq. (3.26), the histograms are obtained numerically, and the dashed curves are the large-N Gaussian limit (3.27).

3.4 Results for model Hamiltonians

The analytical considerations of the previous section rely only on the fundamental symmetries of the Hamiltonian, without reference to a particular model. Here we present numerical results for model Hamiltonians in the various symmetry classes.

3.4.1 Chiral pair potentials

We consider a two-dimensional superconductor in the x-y plane, with pair potential $\hat{\Delta}$ dependent on the momentum $\boldsymbol{p} = -i\hbar(\partial_x, \partial_y)$. The Bogoliubov-De Gennes Hamiltonian, in the electron-hole basis, has the form

$$\mathcal{H} = \begin{pmatrix} H & \hat{\Delta} \\ \hat{\Delta}^\dagger & -H^* \end{pmatrix}. \tag{3.28}$$

It contains the single-particle Hamiltonian

$$H = (\boldsymbol{p} - e\boldsymbol{A})^2/2m_{\text{eff}} - \mu + U, \tag{3.29}$$

with $\boldsymbol{A}(\boldsymbol{r})$ the vector potential, m_{eff} the effective mass, μ the chemical potential, and $U(\boldsymbol{r})$ an electrostatic disorder potential. (We conveniently set the electronic charge to $+e$.)

The electron-hole symmetry relations are different for the different symmetry classes,

$$\hat{\Delta}_{\rm D}^{\dagger} = -\hat{\Delta}_{\rm D}^{*} \Rightarrow \mathcal{H}_{\rm D} = -\tau_x \mathcal{H}_{\rm D}^{*} \tau_x, \tag{3.30a}$$

$$\hat{\Delta}_{\rm C}^{\dagger} = \hat{\Delta}_{\rm C}^{*} \Rightarrow \mathcal{H}_{\rm C} = -\tau_y \mathcal{H}_{\rm C}^{*} \tau_y. \tag{3.30b}$$

As specific models we take in class D the spin-triplet chiral p-wave pairing

$$\hat{\Delta}_{\rm D} = p_{\rm F}^{-1}\{\Delta(\boldsymbol{r}), p_x + ip_y\}, \tag{3.31}$$

with operators symmetrized by $\{a,b\} = \frac{1}{2}(ab+ba)$. In class C we take the spin-singlet chiral d-wave pairing

$$\hat{\Delta}_{\rm C} = \sum_{\alpha,\beta} (\boldsymbol{p} - e\boldsymbol{A})_{\alpha} M_{\alpha\beta} (\boldsymbol{p} + e\boldsymbol{A})_{\beta}, \tag{3.32a}$$

$$\boldsymbol{M}(\boldsymbol{r}) = p_{\rm F}^{-2} \Delta(\boldsymbol{r}) \begin{pmatrix} 1 & i \\ i & -1 \end{pmatrix}. \tag{3.32b}$$

Both pair potentials properly produce a gauge invariant Bogoliubov-De Gennes Hamiltonian, [1]

$$e^{-i\chi\tau_z} \mathcal{H}(\boldsymbol{A}, \Delta) e^{i\chi\tau_z} = \mathcal{H}\left(\boldsymbol{A} - \frac{\hbar}{e}\nabla\chi, e^{-2i\chi}\Delta\right). \tag{3.33}$$

Since $\hat{\Delta}_{\rm D} = \Delta_0 e^{i\theta}$ and $\hat{\Delta}_{\rm C} = \Delta_0 e^{2i\theta}$ when $\Delta(\boldsymbol{r}) = \Delta_0$, $\boldsymbol{A} = 0$, and $\boldsymbol{p} = p_{\rm F}(\cos\theta, \sin\theta)$, the magnitude of the gap is independent of the orientation. We expect that more general anisotropic models will give the same qualitative results — provided that the gap does not vanish in any direction.

The ring has a weak link of length $R_{\rm outer} - R_{\rm inner}$, with $R_{\rm inner}$ and $R_{\rm outer}$ the inner and outer radius of the ring. We assume that the ring is wide compared to the London penetration depth $\lambda_{\rm L}$ but narrow compared to the Josephson penetration depth $\lambda_{\rm J}$,

$$\lambda_{\rm L} \ll R_{\rm outer} - R_{\rm inner} \ll \lambda_{\rm J}. \tag{3.34}$$

---

[1] The symmetry requirement (3.30) and the requirement of gauge invariance (3.33) constrain the functional form of the pair potential in the Bogoliubov-De Gennes Hamiltonian, but some freedom is left. An alternative gauge invariant d-wave pair potential was introduced by Vafek et al. [172]

The first inequality ensures that the magnetic field is screened from the ring except at the weak link, along which a flux Φ can enter. The second inequality prevents vortices to appear inside the weak link. The gauge invariant phase difference across the weak link then has a uniform value $\phi = (2e/\hbar)\Phi$. We will use a gauge with a real uniform order parameter $\Delta(\boldsymbol{r}) = \Delta_0$ and a delta-function vector potential

$$\boldsymbol{A} = \Phi\,\theta(-y)\delta(x)\hat{x}, \tag{3.35}$$

for a Josephson junction at $x = 0$ (aligned along the negative y-axis).

3.4.2 Helical pair potential

We construct a model Hamiltonian with helical pairing from two time-reversed copies of the class-D chiral p-wave pairing, $p_x \pm ip_y$. Spin-orbit coupling of the Rashba form couples the spin-up $p_x + ip_y$ sector with the spin-down $p_x - ip_y$ sector, promoting the symmetry class from D to DIII.

The Bogoliubov-De Gennes Hamiltonian (3.28) contains the single-particle Hamiltonian

$$H_{\text{DIII}} = \big[(\boldsymbol{p} - e\boldsymbol{A})^2/2m_{\text{eff}} - \mu + U\big]\sigma_0 + \alpha_{\text{so}}(p_x\sigma_y - p_y\sigma_x), \tag{3.36}$$

where $\sigma_x, \sigma_y, \sigma_z$ are the Pauli matrices acting on the spin degree of freedom and σ_0 is the corresponding unit matrix. The spin-orbit coupling strength is denoted by α_{so}. The helical pair potential is given by

$$\hat{\Delta}_{\text{DIII}} = p_{\text{F}}^{-1}\{\Delta(\boldsymbol{r}), p_x\sigma_z + ip_y\sigma_0\}. \tag{3.37}$$

The electron-hole symmetry requirement in class DIII is the same as in class D, cf. Eq. (3.30),

$$\hat{\Delta}_{\text{DIII}}^{\dagger} = -\hat{\Delta}_{\text{DIII}}^{*} \Rightarrow \mathcal{H}_{\text{DIII}} = -\tau_x\mathcal{H}_{\text{DIII}}^{*}\tau_x. \tag{3.38}$$

For $\boldsymbol{A} = 0$ and real Δ the class-DIII Hamiltonian satisfies the time reversal symmetry

$$\mathcal{H}_{\text{DIII}} = \sigma_y\mathcal{H}_{\text{DIII}}^{*}\sigma_y. \tag{3.39}$$

3.4.3 Topological phase transition at the Josephson junction

The phase transition in classes D and DIII is evidenced by a closing of the excitation gap at the Josephson junction when $\phi = \pi \pmod{2\pi}$. The

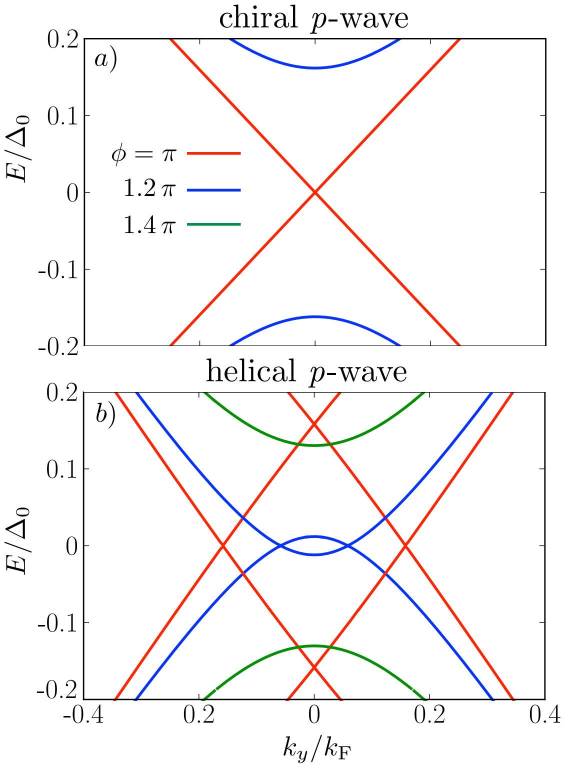

Figure 3.4. Excitation spectrum of an infinitely long Josephson junction along the y-axis, for different values of the phase difference ϕ, calculated numerically from the discretized Bogoliubov-De Gennes Hamiltonian (3.28). Panel a) is for the class-D chiral p-wave pair potential (3.31) and panel b) for the class-DIII helical p-wave pair potential (3.38). The closing of the excitation gap at $\phi = \pi$ is topologically protected. [Model parameters are the same as in Fig. 3.6]

gap closing and reopening is accompanied [3, 65] by a sign change of the topological quantum number $\sigma = \operatorname{Det} R$ (in class D) or $\sigma = \operatorname{Pf} i\tau_y R$ (in class DIII). In Fig. 3.4 we illustrate the gap closing for the chiral and helical p-wave pairings (3.31) and (3.38).

Away from $\phi = \pi$ the gap immediately opens in class D, while the gap closing persists for some range of ϕ in class DIII. This is a consequence of translational invariance along the weak link, see App. 3.6.1. Only the gap closing at $\phi = \pi$ is topologically protected.

In class C there is no gap closing that is *topologically* protected. However, as explained in App. 3.6.1, the combination of translational invari-

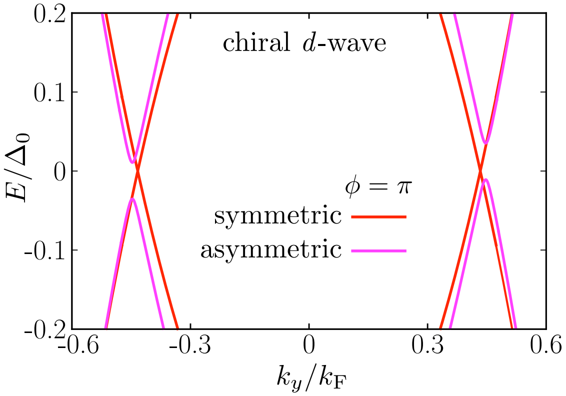

Figure 3.5. Same as Fig. 3.4, for a class-C chiral d-wave pair potential. The two curves are for $\phi = \pi$, with and without $\pm x$ symmetry of the Josephson junction along the y-axis. The gap closing now has no topological protection, but requires a spatial symmetry.

ance along the y-axis and $x \mapsto -x$ reflection symmetry allow for a gap closing at $\phi = \pi$ (mod 2π). We show this in Fig. 3.5 for the chiral d-wave pairing (3.32). Disorder will break these symmetries and remove the gap closing.

3.4.4 Numerical results

We have discretized the Bogoliubov-De Gennes Hamiltonian on a square lattice (lattice constant a, hopping amplitude t, see App. 3.6.2). The geometry is shown in Fig. 3.1, with a pair of normal-metal leads (width $30\,a$) attached to the inner and outer perimeter (radii $50\,a$ and $100\,a$).

The leads are modeled by setting Δ_0, $\boldsymbol{A}$, α_{so}, and U all equal to zero, at a chemical potential $\mu_{\text{N}} = 0.5\,t$ for which there are $M = 6$ orbital modes. Each of these modes is spin-degenerate when coupled to the chiral d-wave or helical p-wave superconductor, and nondegenerate when coupled to the chiral p-wave superconductor.

At the weak link the hopping matrix elements are reduced such that the transmission probability per mode is $\lesssim 0.1$. Disorder in the superconductor is introduced by a random on-site potential $U(x, y)$, uniformly distributed in the interval $(-U_{\text{disorder}}/2, U_{\text{disorder}}/2)$. We took $U_{\text{disorder}} = 0.7\,t$.

We solve the scattering problem numerically [185], to obtain the scat-

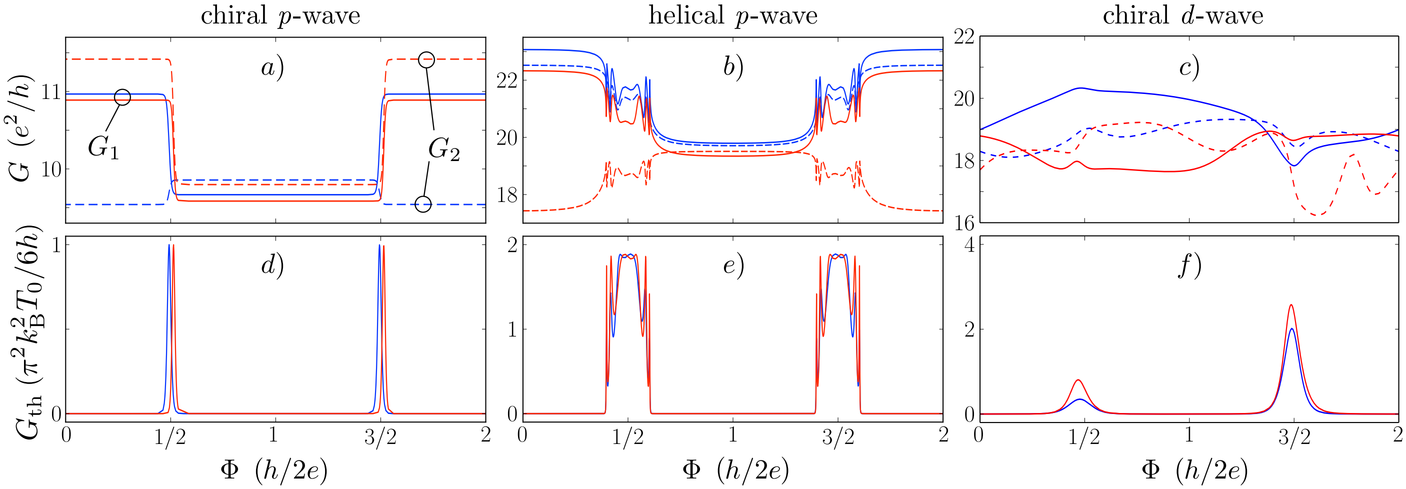

Figure 3.6. Electrical conductance (upper row) and thermal conductance (lower row) in the ring geometry of Fig. 3.1, as a function of the enclosed flux Φ, for the three pair potentials (3.31), (3.38), and (3.32). The red and blue curves are calculated numerically for two different realizations of the disorder potential. The thermal conductance is measured between the inner and outer perimeter of the ring. The electrical conductance is measured either between the inner perimeter and ground (G_1, solid curves) or between the outer perimeter and ground (G_2, dashed curves). [Model parameters for the superconductor are $\mu = t$, $\Delta_0 = 0.4\,t$ for the chiral p-wave pairing, $\mu = t$, $\Delta_0 = 0.6\,t$, $\alpha_{\rm so} = 0.2\,t/p_{\rm F}$ for the helical p-wave pairing, and $\mu = t$, $\Delta_0 = 0.4\,t$ for the chiral d-wave pairing.]

tering matrix $\mathcal{S}$ for the electron (e) and hole (h) modes incident on the superconductor from the inner contact (1) and the outer contact (2). We then calculate the Andreev conductances G_1 and G_2 from the outer or inner contact to ground,

$$G_1 = \frac{e^2}{h}\,\mathrm{Tr}\,(1 - \mathcal{S}_{1e,1e}\mathcal{S}^{\dagger}_{1e,1e} + \mathcal{S}_{1h,1e}\mathcal{S}^{\dagger}_{1h,1e}), \tag{3.40}$$

$$G_2 = \frac{e^2}{h}\,\mathrm{Tr}\,(1 - \mathcal{S}_{2e,2e}\mathcal{S}^{\dagger}_{2e,2e} + \mathcal{S}_{2h,2e}\mathcal{S}^{\dagger}_{2h,2e}). \tag{3.41}$$

This expression holds also at the gap closing, when there is a nonzero transmission probability between contacts 1 and 2, under the assumption that contact 2 is grounded for the measurement of G_1 and contact 1 is grounded for the measurement of G_2.

To probe the gap closing we also calculate the thermal conductance

$$\begin{aligned} G_{\mathrm{th}} = \frac{\pi^2 k_{\mathrm{B}}^2 T_0}{6h}\,\mathrm{Tr}\,(&\mathcal{S}_{2e,1e}\mathcal{S}^{\dagger}_{2e,1e} + \mathcal{S}_{2h,1e}\mathcal{S}^{\dagger}_{2h,1e} \\ &+ \mathcal{S}_{2h,1h}\mathcal{S}^{\dagger}_{2h,1h} + \mathcal{S}_{2e,1h}\mathcal{S}^{\dagger}_{2e,1h}), \end{aligned} \tag{3.42}$$

which measures the thermal current between the inner and outer perimeter at temperatures T_0 and $T_0 + \delta T$.

Results are shown in Fig. 3.6 for several disorder realizations. The results for the electrical conductance (top row) will be discussed in the next section, in connection with experimental probes for Dirac or Majorana edge modes.

The thermal conductance (bottom row) is not easily measured, but is included here because it illustrates in a striking way the significance of topological protection for a gap closing. The change in sign of the topological quantum number at the class-D phase transition results in a peak of the thermal conductance that is quantized [3] in units of the thermal quantum $\pi^2 k_{\mathrm{B}}^2 T_0/6h$, see Fig. 3.6d. The gap closing in class C has no topological protection, there is no sign change of a topological quantum number and no quantized peak, see Fig. 3.6f. The class-DIII gap closing has topological protection (no backscattering) if it happens when the flux is a multiple of $h/4e$, so time-reversal symmetry is preserved. Disorder leads to small displacements of the transition away from $h/4e$, allowing for backscattering and resulting in a small deviation of the thermal conductance peak from the quantized value (see Fig. 3.6e).

3.5 Discussion

The numerical results of Fig. 3.6a,b,c illustrate how circulating edge states manifest themselves in the magnetoconductance of the ring. All three types of edge states introduce a flux dependence with a period of *twice* the superconducting flux quantum $\Phi_0 = h/2e$. The magnetoconductance oscillations are sample specific, depending on the disorder realization. The inner and outer perimeter experience a different impurity potential and thus show a different magnetoconductance, but with the same h/e periodicity. A measurement of the fundamental frequency of the Fourier transformed magnetoconductance would be an unambiguous way to establish the presence of circulating edge states.

The magnetoconductance contains additional information, it can identify unpaired (chiral or helical) Majorana modes. These produce jumps δG in the conductance when the flux is close to an odd multiple of $\Phi_0/2$, associated with a topological phase transition at the Josephson junction. Both the sign and magnitude of δG is disorder dependent and different at the inner and outer perimeter, but the flux Φ_c at which the conductance jumps lines up. Notice that even when different disorder realizations cause a small shift in Φ_c (compare red and blue curves in Fig. 3.6a), the conductance at the inner and outer perimeter jumps at precisely the same Φ_c (compare solid and dashed curves). This phase locking is a striking signature of a topological phase transition at the Josephson junction.

A measurement of the fundamental frequency component $\cos(\Phi/2\Phi_0 + \alpha)$ of the magnetoconductance at the inner and outer perimeter of the ring would therefore show a random and uncorrelated phase α for Dirac modes, and a correlated phase peaked at 0 (modulo π) for an unpaired Majorana mode.

These magnetoconductance signatures of Dirac and Majorana edge states can be helpful in the ongoing search for topological superconductors. Recent attention has focused on hybrid structures combining strong spin-orbit coupling with induced s-wave superconductivity, to produce an effective chiral p-wave pairing [139, 184, 174]. A superconducting ring deposited on a three-dimensional topological insulator would need a magnetic barrier along the perimeter to confine the edge states [61, 94]. Alternatively, one might induce superconductivity in the two-dimensional electron gas of a semiconductor heterostructure with strong spin-orbit coupling [145, 5], such as an InAs quantum well, and confine the edge states electrostatically by gate electrodes.

3.6 Appendix

3.6.1 Gap closings due to spatial symmetries

In symmetry classes D and DIII the closing of the excitation gap at the topological phase transition of the Josephson junction is topologically protected, meaning that disorder cannot open up the gap. However, in Fig. 3.5 we see a gap closing in symmetry class C, where the Josephson junction remains topologically trivial. Morover, in Fig. 3.4b we see that the gap closing in the helical p-wave junction persists over a range of ϕ, rather than being limited to a single ϕ as it is in class D. Both these features are due to spatial symmetries, as we now explain.

Translational symmetry along the weak link (the y-axis) permits us to consider the parallel momentum $k_y \equiv q$ as an external parameter. The Hamiltonian $\mathcal{H}(q)$ describes a zero-dimensional system which can undergo a topological phase transition as a function of the parameter q in symmetry classes D and BDI [138]. At this transition a $\mathbb{Z}_2$ topological quantum number changes sign, so to open up the gap requires, either, the breaking of a symmetry, or the merging of a pair of gap closings at a single value of q.

So how do we arrive in class D or BDI when we start out from class DIII or class C? As pointed out in Ref. [42] in a different context, spatial symmetries can do this.

Let us first show that $\mathcal{H}(q)$ is in class D for helical p-wave pairing. On the one hand, the electron-hole symmetry relation (3.38) gives

$$\mathcal{H}(q) = -\tau_x \mathcal{H}^*(-q)\tau_x, \tag{3.43}$$

on the other hand, the helical p-wave pairing has the additional symmetry

$$(\tau_z \otimes \sigma_y)\mathcal{H}(q)(\tau_z \otimes \sigma_y) = \mathcal{H}(-q). \tag{3.44}$$

Taking these two equations together we arrive at a symmetry relation for $\mathcal{H}(q)$ at one single value of q,

$$\Omega\mathcal{H}(q) = -\mathcal{H}(q)\Omega, \;\; \Omega = (\tau_y \otimes \sigma_y)\mathcal{K}, \tag{3.45}$$

with $\mathcal{K}$ the operator of complex conjugation. Because Ω is an anti-unitary operator that squares to $+1$, this places $\mathcal{H}(q)$ in symmetry class D, with a topologically protected gap closing. Indeed, as we see in Fig. 3.4b, the pair of gap closings at $\phi = \pi$ persist as ϕ is increased, until the gaps merge at $q = 0$.

Turning now to class C, we will show that $\mathcal{H}(q)$ is in class BDI for chiral d-wave pairing at $\phi = \pi$ and if the electrostatic potential $U(x)$ is $\pm x$ symmetric. Firstly, the class-C electron-hole symmetry relation reads

$$\mathcal{H}(q) = -\tau_y \mathcal{H}^*(-q)\tau_y. \tag{3.46}$$

Secondly, for $\phi = \pi$ and $\boldsymbol{A} = 0$ the Hamiltonian is real,

$$\mathcal{H}^*(q) = \mathcal{H}(q). \tag{3.47}$$

Thirdly, the combination of $U(x) = U(-x)$ and $\Delta(x) = -\Delta(-x)$ at $\phi = \pi$ gives

$$\tau_z \mathcal{P}\mathcal{H}(q) = \mathcal{H}(-q)\tau_z \mathcal{P}, \tag{3.48}$$

where $\mathcal{P}$ is the reflection operator ($x \mapsto -x$). Eqs. (3.46) and (3.48) together give

$$\Omega' \mathcal{H}(q) = -\mathcal{H}(q)\Omega', \;\; \Omega' = \tau_x \mathcal{P}\mathcal{K}. \tag{3.49}$$

The anti-unitary operator Ω' also squares to $+1$. The symmetries (3.47) and (3.49) place $\mathcal{H}(q)$ in class BDI, provided that $\phi = \pi$ and the reflection symmetry is unbroken. This is consistent with what is seen in Fig. 3.5: The gap closing for chiral d-wave pairing can be removed either by increasing ϕ away from π or by breaking the $\pm x$ symmetry of the weak link.

3.6.2 Gauge invariant discretization of the Bogoliubov-De Gennes Hamiltonian

The discretization of the Bogoliubov-De Gennes Hamiltonian (3.28) with a momentum dependent pair potential requires special care to ensure that the resulting tight-binding model is gauge invariant. We go through the steps in this Appendix. Following the established procedure of minimal coupling, we first discretize without a vector potential, then perform a gauge transformation on the lattice, and finally replace the gradient of the gauge field by the vector potential.

The discretization for $\boldsymbol{A} = 0$ is carried out by replacing the differential operators by symmetric finite differences,

$$\partial_x f(x) \mapsto \frac{1}{2a}[f(x+a) - f(x-a)], \tag{3.50}$$

to arrive at the tight-binding Hamiltonian

$$t(n,m) = \begin{pmatrix} t_{\rm ee}(n,m) & t_{\rm eh}(n,m) \\ t_{\rm he}(n,m) & t_{\rm hh}(n,m) \end{pmatrix}. \tag{3.51}$$

The indices n, m label sites $\boldsymbol{r}_n, \boldsymbol{r}_m$ of a square lattice (lattice constant a). The diagonal elements $n = m$ are the on-site energies and the off-diagonal elements $n \neq m$ are the hopping amplitudes between sites n and m.

The single-particle kinetic energy gives the electron-electron matrix elements,

$$\begin{aligned} t_{\rm ee}(n,n) &= 4t - \mu + U(\boldsymbol{r}_n), \quad t = \hbar^2/2m_{\rm eff}a^2, \\ t_{\rm ee}(n,m \neq n) &= \begin{cases} -t & \text{for } n,m \text{ nearest neighbours,} \\ 0 & \text{otherwise,} \end{cases} \end{aligned} \tag{3.52}$$

and the hole-hole matrix elements $t_{\rm hh}(n,m) = -t_{\rm ee}(n,m)$.

For the chiral d-wave pair potential (3.32), still at $\boldsymbol{A} = 0$, we obtain the nearest-neighbor hopping amplitudes

$$\begin{aligned} t_{\rm eh}(n \pm a\hat{x}, n) &= -\frac{1}{2q^2}\left[\Delta(\boldsymbol{r}_n) + \Delta(\boldsymbol{r}_n \pm a\hat{x})\right], \\ t_{\rm eh}(n \pm a\hat{y}, n) &= \frac{1}{2q^2}\left[\Delta(\boldsymbol{r}_n) + \Delta(\boldsymbol{r}_n \pm a\hat{y})\right], \end{aligned} \tag{3.53}$$

the next-nearest-neighbor hopping amplitudes

$$\begin{aligned} t_{\rm eh}(n + a\hat{x} \pm a\hat{y}, n) &= \frac{\mp i}{4q^2}\left[\Delta(\boldsymbol{r}_n + a\hat{x}) + \Delta(\boldsymbol{r}_n \pm a\hat{y})\right], \\ t_{\rm eh}(n - a\hat{x} \pm a\hat{y}, n) &= \frac{\pm i}{4q^2}\left[\Delta(\boldsymbol{r}_n - a\hat{x}) + \Delta(\boldsymbol{r}_n \pm a\hat{y})\right], \end{aligned} \tag{3.54}$$

and the on-site matrix elements

$$\begin{aligned} t_{\rm eh}(n,n) = \frac{1}{2q^2}[&\Delta(\boldsymbol{r}_n + a\hat{x}) + \Delta(\boldsymbol{r}_n - a\hat{x}) \\ &- \Delta(\boldsymbol{r}_n + a\hat{y}) - \Delta(\boldsymbol{r}_n - a\hat{y})]. \end{aligned} \tag{3.55}$$

(We have defined $q = k_{\rm F}a$.) These are all hopping amplitudes from hole to electron. The hopping amplitudes from electron to hole are related by Hermiticity,

$$t_{\rm he}(n,m) = t^*_{\rm eh}(m,n). \tag{3.56}$$

We now introduce the vector potential $\boldsymbol{A}(\boldsymbol{r}) = -(\hbar/e)\nabla\chi(\boldsymbol{r})$ by means of the gauge transformation

$$
\begin{aligned}
\tilde{t}(n,m) &= e^{-i\tau_z\chi(\boldsymbol{r}_n)}t(n,m)e^{i\tau_z\chi(\boldsymbol{r}_m)},\\
\tilde{\Delta}(\boldsymbol{r}_n) &= e^{-2i\chi(\boldsymbol{r}_n)}\Delta(\boldsymbol{r}_n).
\end{aligned}
\tag{3.57}
$$

This is the lattice analogue of Eq. (3.33).

The effect on the electron-electron and hole-hole hopping amplitudes is the Peierls substitution [121],

$$
\begin{aligned}
\tilde{t}_{\mathrm{ee}}(n,m) &= t_{\mathrm{ee}}(n,m)\exp\left(i\frac{e}{\hbar}\int_m^n \boldsymbol{A}\cdot d\boldsymbol{l}\right),\\
\tilde{t}_{\mathrm{hh}}(n,m) &= t_{\mathrm{hh}}(n,m)\exp\left(-i\frac{e}{\hbar}\int_m^n \boldsymbol{A}\cdot d\boldsymbol{l}\right).
\end{aligned}
\tag{3.58}
$$

The line integral of the vector potential is taken along the lattice bond from site m to site n, and with this prescription the Peierls substitution can also be applied to vector potentials that do not derive from a gauge field.

The transformed electron-hole matrix hopping amplitudes for chiral d-wave pairing are given by

$$
\begin{aligned}
\tilde{t}_{\mathrm{eh}}(n\pm a\hat{x},n) &= \frac{-1}{2q^2}\left[e^{i\frac{e}{\hbar}\int_n^{n\pm a\hat{x}}\boldsymbol{A}\cdot\mathrm{d}\boldsymbol{l}}\tilde{\Delta}(\boldsymbol{r}_n)+\tilde{\Delta}(\boldsymbol{r}_n\pm a\hat{x})e^{-i\frac{e}{\hbar}\int_n^{n\pm a\hat{x}}\boldsymbol{A}\cdot\mathrm{d}\boldsymbol{l}}\right],\\
\tilde{t}_{\mathrm{eh}}(n\pm a\hat{y},n) &= \frac{1}{2q^2}\left[e^{i\frac{e}{\hbar}\int_n^{n\pm a\hat{y}}\boldsymbol{A}\cdot\mathrm{d}\boldsymbol{l}}\tilde{\Delta}(\boldsymbol{r}_n)+\tilde{\Delta}(\boldsymbol{r}_n\pm a\hat{y})e^{-i\frac{e}{\hbar}\int_n^{n\pm a\hat{y}}\boldsymbol{A}\cdot\mathrm{d}\boldsymbol{l}}\right],
\end{aligned}
\tag{3.59}
$$

$$
\begin{aligned}
\tilde{t}_{\mathrm{eh}}(n+a\hat{x}\pm a\hat{y},n) = \frac{\mp i}{4q^2}\Bigg[&e^{i\frac{e}{\hbar}\int_{n+a\hat{x}}^{n+a\hat{x}\pm a\hat{y}}\boldsymbol{A}\cdot\mathrm{d}\boldsymbol{l}}\tilde{\Delta}(\boldsymbol{r}_n+a\hat{x})e^{-i\frac{e}{\hbar}\int_n^{n+a\hat{x}}\boldsymbol{A}\cdot\mathrm{d}\boldsymbol{l}}\\
&+e^{i\frac{e}{\hbar}\int_{n\pm a\hat{y}}^{n+a\hat{x}\pm a\hat{y}}\boldsymbol{A}\cdot\mathrm{d}\boldsymbol{l}}\tilde{\Delta}(\boldsymbol{r}_n\pm a\hat{y})e^{-i\frac{e}{\hbar}\int_n^{n\pm a\hat{y}}\boldsymbol{A}\cdot\mathrm{d}\boldsymbol{l}}\Bigg],\\
\tilde{t}_{\mathrm{eh}}(n-a\hat{x}\pm a\hat{y},n) = \frac{\pm i}{4q^2}\Bigg[&e^{i\frac{e}{\hbar}\int_{n-a\hat{x}}^{n-a\hat{x}\pm a\hat{y}}\boldsymbol{A}\cdot\mathrm{d}\boldsymbol{l}}\tilde{\Delta}(\boldsymbol{r}_n-a\hat{x})e^{-i\frac{e}{\hbar}\int_n^{n-a\hat{x}}\boldsymbol{A}\cdot\mathrm{d}\boldsymbol{l}}\\
&+e^{i\frac{e}{\hbar}\int_{n\pm a\hat{y}}^{n-a\hat{x}\pm a\hat{y}}\boldsymbol{A}\cdot\mathrm{d}\boldsymbol{l}}\tilde{\Delta}(\boldsymbol{r}_n\pm a\hat{y})e^{-i\frac{e}{\hbar}\int_n^{n\pm a\hat{y}}\boldsymbol{A}\cdot\mathrm{d}\boldsymbol{l}}\Bigg],\\
\tilde{t}_{\mathrm{eh}}(n,n) = \frac{1}{2q^2}\Bigg[&\tilde{\Delta}(\boldsymbol{r}_n+a\hat{x})e^{-i\frac{2e}{\hbar}\int_n^{n+a\hat{x}}\boldsymbol{A}\cdot\mathrm{d}\boldsymbol{l}}+\tilde{\Delta}(\boldsymbol{r}_n-a\hat{x})e^{-i\frac{2e}{\hbar}\int_n^{n-a\hat{x}}\boldsymbol{A}\cdot\mathrm{d}\boldsymbol{l}}\\
&-\tilde{\Delta}(\boldsymbol{r}_n+a\hat{y})e^{-i\frac{2e}{\hbar}\int_n^{n+a\hat{y}}\boldsymbol{A}\cdot\mathrm{d}\boldsymbol{l}}-\tilde{\Delta}(\boldsymbol{r}_n-a\hat{y})e^{-i\frac{2e}{\hbar}\int_n^{n-a\hat{y}}\boldsymbol{A}\cdot\mathrm{d}\boldsymbol{l}}\Bigg].
\end{aligned}
\tag{3.60}
$$

A similar calculation for the chiral p-wave pairing (3.31) gives the electron-hole hopping amplitudes

$$\begin{aligned}\tilde{t}_{\rm eh}(n \pm a\hat{x}, n) &= \frac{\mp i}{4q}\left[e^{i\frac{e}{\hbar}\int_n^{n\pm a\hat{x}} \boldsymbol{A}\cdot {\rm d}\boldsymbol{l}}\tilde{\Delta}(\boldsymbol{r}_n) + \tilde{\Delta}(\boldsymbol{r}_n \pm a\hat{x})e^{-i\frac{e}{\hbar}\int_n^{n\pm a\hat{x}} \boldsymbol{A}\cdot {\rm d}\boldsymbol{l}}\right], \\ \tilde{t}_{\rm eh}(n \pm a\hat{y}, n) &= \frac{\pm 1}{4q}\left[e^{i\frac{e}{\hbar}\int_n^{n\pm a\hat{y}} \boldsymbol{A}\cdot {\rm d}\boldsymbol{l}}\tilde{\Delta}(\boldsymbol{r}_n) + \tilde{\Delta}(\boldsymbol{r}_n \pm a\hat{y})e^{-i\frac{e}{\hbar}\int_n^{n\pm a\hat{y}} \boldsymbol{A}\cdot {\rm d}\boldsymbol{l}}\right].\end{aligned} \tag{3.61}$$

There are neither next-nearest-neighbor hoppings, nor on-site electron-hole matrix elements in this case.

Notice that the discretized p-wave pair potential (3.61) depends explicitly on the vector potential, while in the continuum representation (3.31) the vector potential enters only implicitly through $\Delta(\boldsymbol{r})$. All of this is required by gauge invariance.

Finally, we give the corresponding expressions for the helical p-wave pairing (3.37). There is now a spin degree of freedom $\sigma =\uparrow,\downarrow$, and the pair potential is diagonal in that index. The electron-hole hopping amplitudes are given by

$$\begin{aligned}\tilde{t}_{\rm e\uparrow,h\uparrow}(n \pm a\hat{x}, n) &= -\tilde{t}_{\rm e\downarrow,h\downarrow}(n \pm a\hat{x}, n) \equiv \tilde{t}_{\rm eh}(n \pm a\hat{x}, n), \\ \tilde{t}_{\rm e\uparrow,h\uparrow}(n \pm a\hat{y}, n) &= \tilde{t}_{\rm e\downarrow,h\downarrow}(n \pm a\hat{y}, n) \equiv \tilde{t}_{\rm eh}(n \pm a\hat{y}, n),\end{aligned} \tag{3.62}$$

where matrix elements without spin indices should be taken from Eq. (3.61).

Chapter 4

Bimodal conductance distribution of Kitaev edge modes in topological superconductors

4.1 Introduction

Gapless edge states are a striking manifestation of topological protection in two-dimensional systems. First studied in connection with the quantum Hall effect in a strong magnetic field [72, 28], they are now known to exist also in the presence of time-reversal symmetry (for topological insulators) or particle-hole symmetry (for topological superconductors) [73, 127]. The edge current can carry charge or heat, it can be uni-directional (chiral) or bi-directional (helical), but in each manifestation there is no backscattering — so that the corresponding electrical or thermal conductance is quantized, independent of system size.

Isotropic two-dimensional superconductors with spin-triplet p-wave pairing belong to the class of topological superconductors, with charge-neutral gapless edge states. Depending on the absence or presence of time-reversal symmetry, the edge modes can be chiral (class D) or helical (class DIII). It is known that the quantization of the thermal conductance breaks down if the two-dimensional superconductor is strongly anisotropic; the edge states remain, but backscattering by disorder is no longer forbidden by a topological invariant [9, 68, 152, 27]. One might surmise

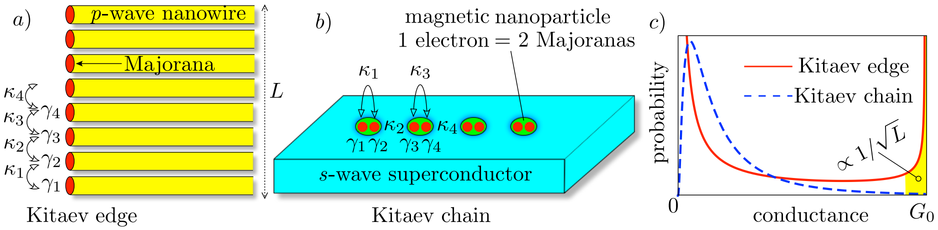

Figure 4.1. Two realizations of the Kitaev Hamiltonian, at the edge of an array of nanowires (Kitaev edge, panel *a*) and in a chain of magnetic nanoparticles (Kitaev chain, panel *b*, adapted from Refs. [39, 110]). Statistical translational invariance at the Kitaev edge means that all couplings κ_n between Majorana fermion operators γ_n and γ_{n+1} have the same statistical distribution. In the Kitaev chain it means that the couplings κ_{2n} between nanoparticles have the same distribution, as well as the couplings κ_{2n-1} of pairs of Majorana fermions within a nanoparticle — while the sets κ_{2n} and κ_{2n-1} are unrelated. This difference is the reason that statistical translational invariance protects the Kitaev edge from localization, but not the Kitaev chain. As a consequence, the thermal conductance has a lognormal distribution in the Kitaev chain (dashed curve in panel *c*), but a bimodal distribution in the Kitaev edge (solid curve, with a second peak of weight $\propto 1/\sqrt{L}$ at the conductance quantum G_0).

that the edge states will localize on length scales L larger than the mean free path ℓ, with an exponentially decaying conductance $\propto \exp(-L/\ell)$, but that is not what happens. Instead, in Ref. [68] an anomalously slow (super-Ohmic) scaling $\propto \sqrt{\ell/L}$ was found, unlike that of any known one-dimensional system. A statistical symmetry (translational invariance of the disorder distribution) was identified as the origin of the topological protection [68].

Here we study this remarkable delocalization of edge states in the framework of the Kitaev Hamiltonian [90] of randomly coupled Majorana fermions. We contrast the two realizations of the model illustrated in Fig. 4.1: at the edge of a two-dimensional superconductor (Kitaev edge, Fig. 4.1*a*) and as a one-dimensional chain of nanoparticles (Kitaev chain, Fig. 4.1*b*). While the Kitaev chain allows for delocalization, this requires a fine-tuning to the critical point of the topological phase diagram [23, 3]. Generically, the conductance of the Kitaev chain has a log-normal distribution peaked at an exponentially small value [108, 24, 25, 71], because disorder drives the system away from the gapless critical point into the gapped phase. In contrast, for the Kitaev edge we find a bimodal conductance distribution, with a second peak near the quantized conductance of the clean system. (Compare dashed and solid curves in Fig. 4.1*c*.) The $\sqrt{\ell/L}$ weight of this second peak produces the super-Ohmic conductance scaling of Ref. [68].

We explain the difference in conductance distributions in terms of the different way in which translational invariance of the disorder distribution is realized in the two systems: in the Kitaev edge all nearest-neigbor coupling strengths of Majorana fermions are statistically equivalent, while in the Kitaev chain even and odd-numbered couplings are inequivalent. Finally, we show how the charge-neutral edge modes of the topological superconductor can be detected in an electrical — rather than thermal — measurement, by considering the shot noise of time-dependent current fluctuations.

The outline of this paper is as follows. In Section 4.2 we introduce model Hamiltonians for p-wave superconductors with chiral or helical edge states and calculate the topological phase diagram in the presence of both anisotropy and disorder. The topological phase transitions are identified by considering the bulk conductance and the associated topological invariants. Edge conductance in the topologically nontrivial phases is studied in Section 4.3. In Section 4.4 we contrast the conductance distributions of the Kitaev edge and the Kitaev chain. Electrical, rather than thermal, detection of the edge modes is discussed in Section 4.5. We conclude in Section 4.6.

4.2 Topological phase diagrams of chiral and helical *p*-wave superconductors

The topological phase diagram of clean chiral p-wave superconductors (or superfluids) was studied in Refs. [9, 152, 27]. Here we show how the topologically distinct phases evolve when we include disorder, for both chiral and helical pair potentials, which as we will see have a qualitatively different phase diagram. Numerical calculations on a disordered tight-binding model are compared with analytical calculations of the phase boundaries in self-consistent Born approximation.

4.2.1 Model Hamiltonians

Superconductors with broken spin-rotation symmetry are in symmetry class D or DIII in the Altland-Zirnbauer classification [7], depending on whether time-reversal symmetry is broken or not. In both symmetry classes the Bogoliubov-De Gennes Hamiltonian $\mathcal{H}(\boldsymbol{k})$ has electron-hole symmetry,

$$\tau_x \mathcal{H}(\boldsymbol{k}) \tau_x = -\mathcal{H}^*(-\boldsymbol{k}), \tag{4.1}$$

where the Pauli matrix τ_i acts on the electron-hole degree of freedom. In class DIII there is additionally the time-reversal symmetry

$$\sigma_y \mathcal{H}(\boldsymbol{k}) \sigma_y = \mathcal{H}^*(-\boldsymbol{k}), \tag{4.2}$$

with σ_i acting on the spin degree of freedom and $\hbar\boldsymbol{k}$ the momentum.

The minimal class-D Hamiltonian, constrained by Eq. (4.1), has the form

$$\mathcal{H}_{\mathrm{D}}(\boldsymbol{k}) = \epsilon(\boldsymbol{k})\tau_z + \Delta_x \tau_x \sin k_x + \Delta_y \tau_y \sin k_y, \tag{4.3a}$$

$$\epsilon(\boldsymbol{k}) = -2t_x \cos k_x - 2t_y \cos k_y - \mu, \tag{4.3b}$$

where $(\Delta_x, \Delta_y) = (\Delta, \alpha\Delta)$ is the anisotropic amplitude of the chiral p-wave pair potential (in a gauge where it's real), $(t_x, t_y) = (t, \alpha t)$ is the anisotropic hopping amplitude, and μ is the chemical potential. The parameter $\alpha \in [0, 1]$ measures the degree of anisotropy, with $\alpha \to 1$ the isotropic limit. We consider equal-spin pairing, so the spin degree of freedom does not appear in $\mathcal{H}_{\mathrm{D}}$.

In class DIII the additional constraint (4.2) is satisfied by taking two time-reversed copies of the Hamiltonian (4.3),

$$\begin{aligned}\mathcal{H}_{\mathrm{DIII}}(\boldsymbol{k}) = {} & \epsilon(\boldsymbol{k})(\sigma_0 \otimes \tau_z) + \Delta_x(\sigma_z \otimes \tau_x) \sin k_x \\ & + \Delta_y(\sigma_0 \otimes \tau_y) \sin k_y + K(\sigma_y \otimes \tau_y),\end{aligned} \tag{4.4}$$

coupled with strength K.

The Hamiltonians (4.3) and (4.4) are discretized on a two-dimensional square lattice of size $L_x \times L_y$ (lattice constant $a \equiv 1$). Electrostatic disorder (strength δ) is added by randomly varying μ, independently for each lattice site and uniformly in the interval $[\mu - \delta, \mu + \delta]$. We study thermal conduction by attaching disorder-free leads at two ends of the

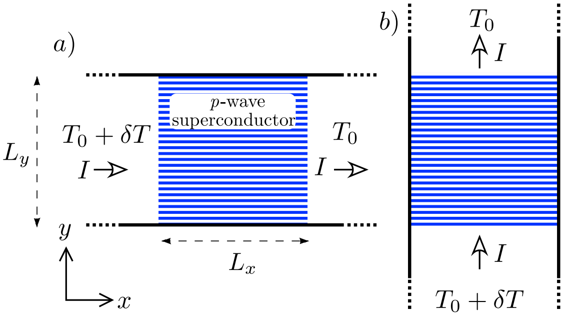

Figure 4.2. Two-terminal geometries for thermal conduction in an anisotropic p-wave superconductor. Panels a and b show the perpendicular orientations of the heat current I in response to a temperature difference δT. The thermal conductance in linear response is $G = \lim_{\delta T \to 0} I/\delta T$.

lattice, connected to reservoirs at temperature T_0 and $T_0 + \delta T$ (see Fig. 4.2). The scattering matrix,

$$S = \begin{pmatrix} r & t \\ t' & r' \end{pmatrix}, \tag{4.5}$$

evaluated at the Fermi level ($E = 0$) determines the thermal conductance

$$G = G_0 \operatorname{Tr} t^\dagger t, \quad G_0 = \pi^2 k_{\rm B}^2 T_0/6h, \tag{4.6}$$

in the low-temperature, linear response regime. The numerical calculations are performed using the KWANT tight-binding code [70].

4.2.2 Class D phase diagram

Clean limit

We first discuss the phase diagram of the class-D Hamiltonian (4.3) in the clean limit of Refs. [9, 152, 27], before including the effects of disorder. Without disorder the momentum is a good quantum number and one can search for gap closings in the Brillouin zone. These occur at the four high-symmetry points $k_x, k_y \in \{0, \pi\}$, for chemical potentials $\mu = \pm 2t(1 \pm \alpha)$. In the μ-α plane the four gapless lines are boundaries separating five topologically distinct insulating phases, see Fig. 4.3.

The number of chiral edge modes is given by the Chern number ν [73, 127, 169], being the winding number of eigenstates in the Brillouin zone.

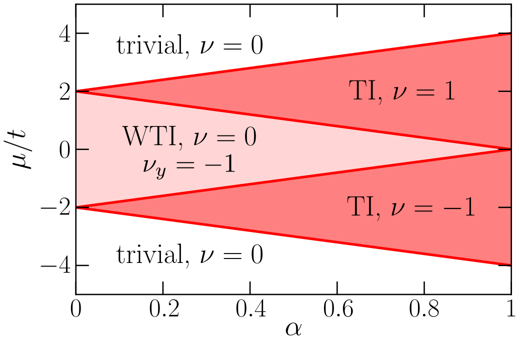

Figure 4.3. Phase diagram of the class-D Hamiltonian (4.3) in the absence of disorder ($\delta = 0$), as a function of chemical potential μ and anisotropy α. The strong topological insulator phases (TI) have chiral Majorana modes along all edges, while the weak topological insulator phase (WTI) has Majorana modes only along edges oriented in the y-direction. The trivial phase has no edge modes.

We compute this two-dimensional topological invariant from the scattering matrix rather than from an integral over the Brillouin zone, in a formulation that can be applied directly to disordered systems [21, 66],

$$\nu = \frac{1}{2\pi i} \int_0^{2\pi} d\phi \, \frac{d}{d\phi} \ln \det r(\phi). \tag{4.7}$$

Here $r(\phi)$ is the reflection block of the scattering matrix (5.4) in the geometry of Fig. 4.2a, with leads attached to $x = 0$ and $x = L_x$ and twisted periodic boundary conditions[1] on the scattering state $\psi(x, y)$ in the y-direction: $\psi(x, 0) = e^{i\phi}\psi(x, L_y)$.

For $2t(1 - \alpha) < |\mu| < 2t(1 + \alpha)$ the system is topologically non-trivial, with $\nu = \operatorname{sign} \mu$ and a chiral Majorana edge mode. (The sign of ν gives the direction of propagation.) The absence of backscattering leads to a quantized thermal edge conductance $G = G_0$. This characterizes the strong topological insulator (TI).

When $|\mu| > 2t(1 + \alpha)$ or $|\mu| < 2t(1 - \alpha)$ the Chern number $\nu = 0$, so there are no chiral edge modes. These regions in the phase diagram are

---

[1] When we implement the twisted periodic boundary condition on the lattice it should extend over an odd number of sites, in order to avoid a minigap in the edge state spectrum that would spoil the calculation of the weak topological invariant (Figs. 4.5 and 4.8). For the conductance it makes no difference whether there is an even or an odd number of lattice sites across.

distinguished by an alternative “weak” topological invariant ν_y [59, 60]. Again, to prepare ourselves for disorder effects, we use a scattering matrix formulation rather than a Brillouin zone formulation [9, 152]. The two-dimensional weak topological invariant is the strong topological invariant in one dimension lower, which in class D is given by the determinant of the reflection matrix [3],

$$\nu_y = \det r(\phi = 0). \tag{4.8}$$

The dimensional reduction is implemented by evaluating $r(\phi)$ at $\phi = 0$, so for periodic boundary conditions in the y-direction. When the Chern number $\nu = 0$ the weak invariant ν_y may be equal to $+1$ (trivial insulator) or -1 (weak topological insulator, WTI).

For $|\mu| > 2t(1+\alpha)$ we are in the topologically trivial phase, with $\nu_y = 1$ and no edge modes at all. In contrast, when $|\mu| < 2t(1-\alpha)$ the system is a WTI, with $\nu_y = -1$ and non-chiral Majorana modes on the edges in the y-direction.

Disorder effects

Having described the phase diagram of the system in the clean limit, we now turn to the effects of disorder. Sufficiently strong disorder can convert a class-D superconductor that is insulating in the bulk into a thermal metal [150, 51, 103]. To search for this topological phase transition we take the two-terminal geometry of Fig. 4.2a with periodic boundary conditions in the y-direction, in order to focus on the metallic or insulating nature of the bulk. (We will consider edge conduction in Sec. 4.3.)

Numerical results for the disorder-averaged thermal conductance $\langle G \rangle$ are shown in Fig. 4.4, as a function of chemical potential μ and disorder strength δ. One can see that both the TI and WTI phases are robust to disorder, up to about $\delta \approx t$. For stronger disorder there is a TI-to-thermal metal phase transition, followed by a transition to a topologically trivial Anderson insulator. The phase boundaries between TI, WTI, and thermal metal are in quite good agreement with those calculated in self-consistent Born approximation (dashed lines in Fig. 4.4, see App. 4.7.1 for details of the calculation). The transition to an Anderson insulator at strong disorder is out of reach of that approximation.

The distinct topological nature of the TI, WTI, and trivial phase is confirmed by a calculation of the topological invariants ν, ν_y, see Fig. 4.5. In the bulk insulating phases these are quantized numbers: $\nu \in \{-1, 0, 1\}$

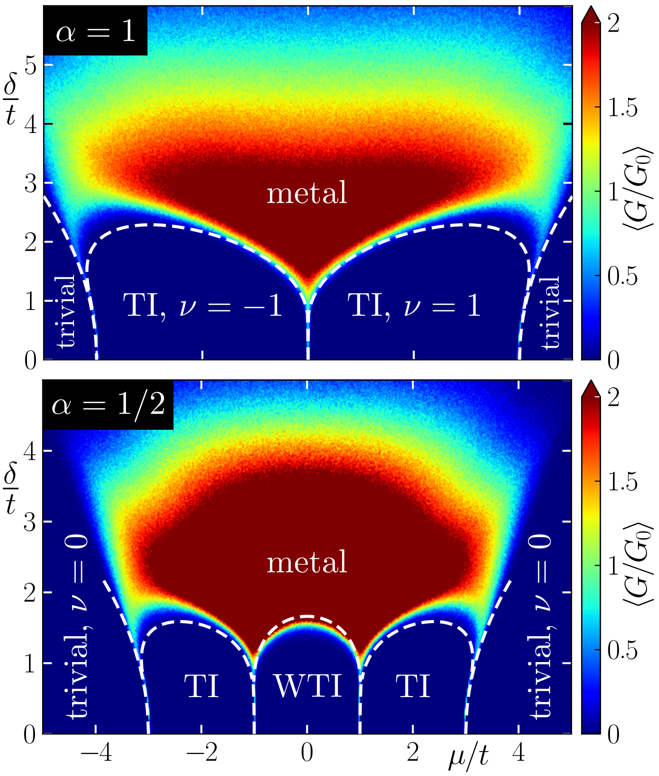

Figure 4.4. Bulk thermal conductance for the class-D Hamiltonian (4.3), as a function of chemical potential μ and disorder strength δ, for two values of the anisotropy at fixed $\Delta = t/2$. The data is averaged over 50 disorder realizations on a lattice of dimensions $L_x = L_y = 50$ (current in the x-direction, periodic boundary conditions in the y-direction). The isotropic case (top panel, $\alpha = 1$) shows gapped TI phases that are robust to disorder up to values $\delta \lesssim 2t$. In the presence of anisotropy (bottom panel, $\alpha = 1/2$), the weak topological insulator which forms at $|\mu| < 2t(1-\alpha)$ survives up to disorder strengths of the same order as the TI phases. Dashed lines represent the phase boundaries in self-consistent Born approximation, without any fit parameter.

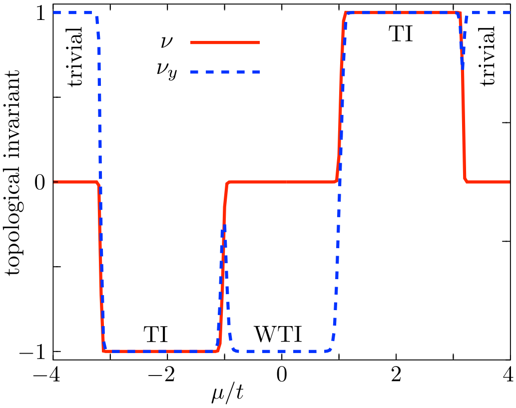

Figure 4.5. Topological phase transitions signaled by a change in the Chern number ν (red solid line) or the weak invariant ν_y (blue dashed line). The curves are calculated from the class-D Hamiltonian (4.3), using the scattering matrix formulas (5.5) and (5.6), for $\Delta = t/2$, $\alpha = 1/2$, $\delta = t$, averaged over 4000 disorder realizations in a system of size $L_x \times L_y = 50 \times 50$.

(a so-called $\mathbb{Z}$ invariant), while $\nu_y \in \{-1, 1\}$ (a $\mathbb{Z}_2$ invariant). At the topological phase transitions, when the bulk gap closes, both ν and ν_y are free to vary between these integer values, resulting in the smooth transitions shown in Fig. 4.5.

4.2.3 Class DIII phase diagram

Clean limit

We now turn to the phase diagram of the class DIII Hamiltonian (4.4), first without disorder. It is convenient to rotate the Hamiltonian to a block off-diagonal form,

$$U\mathcal{H}_{\rm DIII}U^\dagger = \begin{pmatrix} 0 & A \\ A^\dagger & 0 \end{pmatrix}, \quad U = \exp(-\tfrac{1}{4}i\pi\,\sigma_x \otimes \tau_x), \tag{4.9a}$$

$$\begin{aligned} A = {} & i\Delta\sigma_0 \sin k_x + \alpha\Delta\sigma_z \sin k_y \\ & + (\mu + 2t\cos k_x + 2\alpha t \cos k_y - iK)\sigma_y. \end{aligned} \tag{4.9b}$$

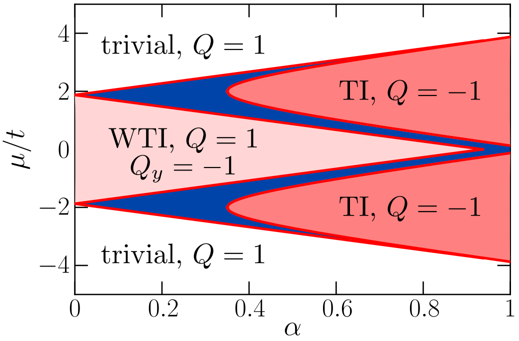

Figure 4.6. Phase diagram of the class-DIII Hamiltonian (4.4) without disorder, for $K/\Delta = 0.35$. Topologically distinct insulating phases are separated by gapless metallic regions (blue). The topologically trivial insulator, without edge states, exists for any amount of anisotropy, while the TI and WTI phases with edge states require, respectively, $\alpha > K/\Delta$ and $\alpha < \sqrt{1 - K^2/\Delta^2}$.

At the gap closings of H_{DIII} the determinant of A vanishes, which happens when

$$\mu/t = -2\cos k_x - 2\alpha \cos k_y, \tag{4.10a}$$

$$K^2/\Delta^2 = \sin^2 k_x + \alpha^2 \sin^2 k_y. \tag{4.10b}$$

The gap closings identify the boundaries of insulating phases, as shown in Fig. 4.6. While in class D the gap closes along a line in the phase diagram, in class DIII there are extended gapless regions of a metallic phase separating the insulating phases. (This is a generic feature of helical p-wave superconductors [67].)

We can distinguish five distinct insulating regions of phase space. For weak anisotropy, $\alpha > K/\Delta$, we find two $\pm\mu$ symmetric insulating phases bounded by

$$2 - 2\sqrt{\alpha^2 - K^2/\Delta^2} < |\mu/t| < 2 + 2\sqrt{\alpha^2 - K^2/\Delta^2}. \tag{4.11}$$

When the anisotropy reaches the critical value

$$\alpha_c = (1 - K^2/\Delta^2)^{1/2}, \tag{4.12}$$

a third insulating phase appears centered around $\mu = 0$, in the interval

$$|\mu/t| < 2(\alpha_c - \alpha), \quad \text{for} \ \ \alpha < \alpha_c. \tag{4.13}$$

Additionally, for any amount of anisotropy there are insulating phases at large chemical potentials, with boundaries given by

$$|\mu/t| < \begin{cases} 2\alpha + 2\sqrt{1 - K^2/\Delta^2}, & \text{for } \alpha < \alpha_c \\ 2\sqrt{2}\sqrt{1 + \alpha^2 - K^2/\Delta^2}, & \text{for } \alpha > \alpha_c. \end{cases} \tag{4.14}$$

To test the topological properties of these phases, we compute the associated DIII topological invariants in a scattering formulation (so that we can directly apply it to disordered systems in the next subsection). The strong topological invariant [66],

$$Q = \text{Pf}\,[i\sigma_y r(\phi = 0)] \times \text{Pf}\,[i\sigma_y r(\phi = \pi)], \tag{4.15}$$

is determined by the Pfaffians of the reflection matrix with periodic ($\phi = 0$) and anti-periodic ($\phi = \pi$) boundary conditions in the y-direction. In view of the time-reversal symmetry condition (4.2), the matrix $i\sigma_y r(\phi)$ is antisymmetric for $\phi = 0, \pi$, so the Pfaffian exists.

The insulating regions delimited by Eq. (4.11) are topologically nontrivial ($Q = -1$), with helical Majorana edge states and quantized thermal conductance $G = 2G_0$. All other phases have $Q = 1$. The ones appearing at large chemical potentials, bounded by Eq. (4.14), are topologically trivial, without edge states. However, the phase which develops at the critical anisotropy α_c, bounded by Eq. (4.13), has $Q = 1$ but still supports gapless modes on edges oriented in the y-direction. The weak topological invariant $Q_y = -1$ of this phase is obtained by dimensional reduction to the one-dimensional class-DIII topological invariant [65],

$$Q_y = \text{Pf}\,[i\sigma_y r(\phi = 0)]. \tag{4.16}$$

Disorder effects

Fig. 4.7 shows the effect of disorder on the topological phases, probed by calculating the thermal conductance in the geometry of Fig. 4.2a with periodic boundary conditions in the y-direction. Comparison with the class-D phase diagram of Fig. 4.4 shows as a qualitative difference that the thermal metal phase extends down to zero disorder. This behavior is also captured by the self-consistent Born approximation (dashed curves), see App. 4.7.1 for details of the calculation.

The scattering matrix formulas (4.15) and (4.16) for the class-DIII strong and weak topological invariants are applied to a disordered system

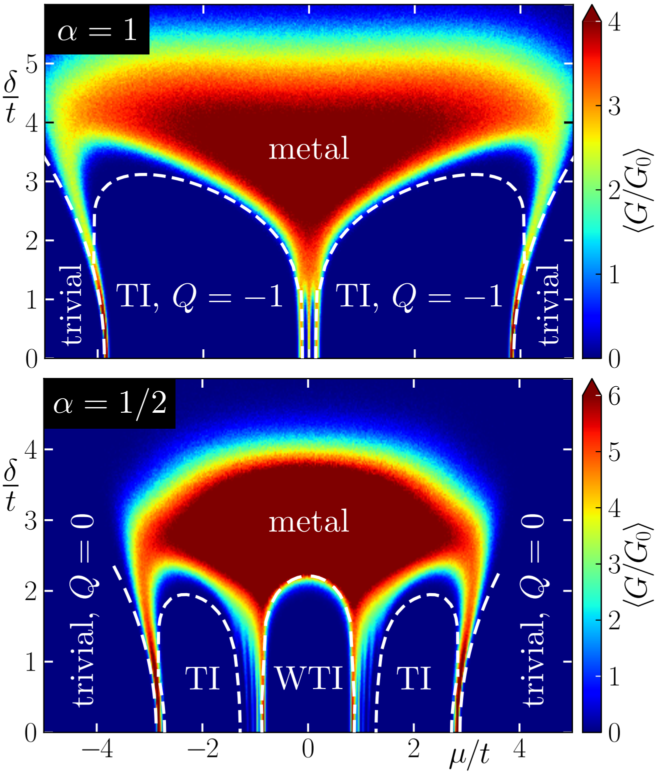

Figure 4.7. Same as Fig. 4.4 for the class-DIII Hamiltonian (4.4) (with $\Delta = t$, $K = 0.35\,t$, other parameters unchanged). Notice that the thermal metal phase starts already at zero disorder.

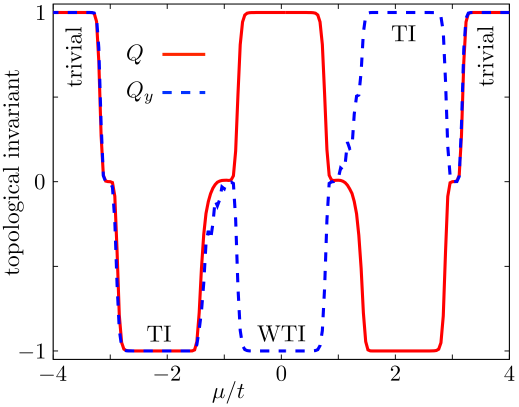

Figure 4.8. Same as Fig. 4.5 for the class-DIII topological invariants Q, Eq. (4.15), and Q_y, Eq. (4.16) (with $\delta = 1.5\,t$, other parameters as in Fig. 4.7).

in Fig. 4.8. These are both $\mathbb{Z}_2$ invariants, meaning that they take on the values ± 1 when the bulk is insulating: $Q = Q_y = 1$ in the trivial insulator, $Q = -1$, $Q_y = \pm 1$ in the TI, and $Q = 1$, $Q_y = -1$ in the WTI.

4.3 Edge conduction

So far we studied thermal conduction in the geometry of Fig. 4.2*a* with periodic boundary conditions in the transverse direction, in order to eliminate edge contributions and focus on bulk properties. To study edge conduction in the TI and WTI phases we now take the geometry of Fig. 4.2*b*, with leads attached to $y = 0, L_y$ and hard-wall boundary conditions at $x = 0, L_x$. We again first consider the clean case and then add the effects of disorder, for both symmetry classes D and DIII.

4.3.1 Clean case

The TI and WTI phases both have gapless edge states, the difference being that the TI edge states appear on all edges while the WTI edge states exist only at two of the four edges (see Fig. 4.9). In the geometry of Fig. 4.2*b* we can probe the edge conductance in both phases. Without disorder the conductance is system-size independent, because there is no backscattering, and the difference between the TI and WTI phases is simply a factor of two.

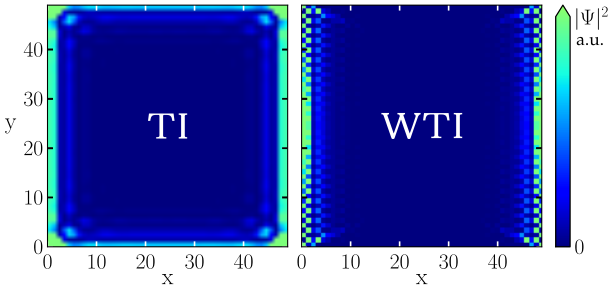

Figure 4.9. Intensity of the lowest eigenstate of the class-D Hamiltonian (4.3) (with $\delta = 0$, $\alpha = 1/2$, $\Delta = t/2$). The edge states in the TI ($\mu = 2.2\,t$) and WTI ($\mu = 0.2\,t$) phases are contrasted in the two panels.

This conductance doubling at the TI-to-WTI transition is shown in Fig. 4.10. In class D it happens because the chiral edge state of the TI phase can propagate in both directions in the WTI phase. In class DIII we start out with helical edge states in the TI phase, with direction of propagation tied to the spin degree of freedom. In the WTI phase this helicity is lost, so now both spin-up and spin-down can propagate in both directions and the conductance is doubled.

4.3.2 Disorder effects

The addition of disorder has no effect on the conductance in the TI phase, since backscattering of chiral or helical edge states is forbidden. The edge states in the WTI are neither chiral nor helical, so disorder does cause backscattering and reduces the edge conductance. However, as discovered in Ref. [68], the recovery of translational invariance upon ensemble averaging prevents localization of the WTI edge states. Instead of an exponential decay of the conductance with the length $L \equiv L_y$ of the edge, there is only an algebraic $1/\sqrt{L}$ decay. In Fig. 4.11 we show this super-Ohmic conductance scaling for the WTI phase of the class-D and class-DIII Hamiltonians (4.3) and (4.4).

4.4 Kitaev chain versus Kitaev edge

The absence of localization at the edge of the anisotropic p-wave superconductor is puzzling if one tries to understand it starting from the limit

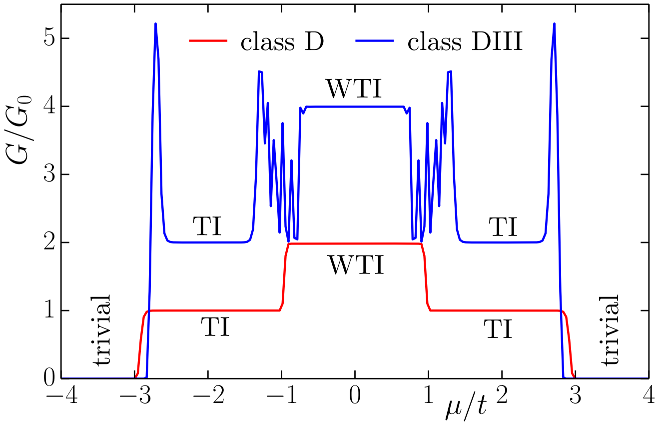

Figure 4.10. Thermal conductance without disorder in class D and DIII. The geometry is that of Fig. 4.2*b* with dimensions $L_x = L_y = 50$ and hard-wall boundaries in the x-direction. Parameters are $\Delta = t$, $\alpha = 1/2$, and $K = 0.35\,t$. The transition from the TI to the WTI phase is marked by a doubling of the edge conductance in the absence of backscattering. In class DIII the transition occurs via an intermediate region of thermal conduction through the gapless bulk.

$\alpha \to 0$ of strong anisotropy. Then the system can be thought of as an array of weakly coupled nanowires with overlapping Majorana zero-modes at the end points, a so-called Kitaev ladder [181, 178, 49]. The effective edge Hamiltonian is the Kitaev Hamiltonian [90] in class D, or two time-reversed copies of it in class DIII. The disordered one-dimensional Kitaev model, called the Kitaev chain, is known to be an insulator [108, 24, 25, 71] — so how do the Kitaev edge modes avoid localization?

To clarify the situation we contrast the two class-D systems. (Class DIII is similar.) The Kitaev Hamiltonian

$$H_{\rm K} = \sum_{n=1}^{2N} i\kappa_n\gamma_n\gamma_{n+1} \qquad (4.17)$$

describes the nearest-neigbor coupling (coupling strength κ_n) of $2N$ Majorana fermion operators γ_n. These are Hermitian operators, $\gamma_n = \gamma_n^\dagger$, with anti-commutation relation $\gamma_n\gamma_m + \gamma_m\gamma_n = 2\delta_{nm}$. To obtain a closed system the Majorana's are assumed to lie on a ring, so that κ_{2N} couples γ_{2N} to $\gamma_{2N+1} \equiv \gamma_1$.

This one-dimensional system in symmetry class D has a $\mathbb{Z}_2$ topological

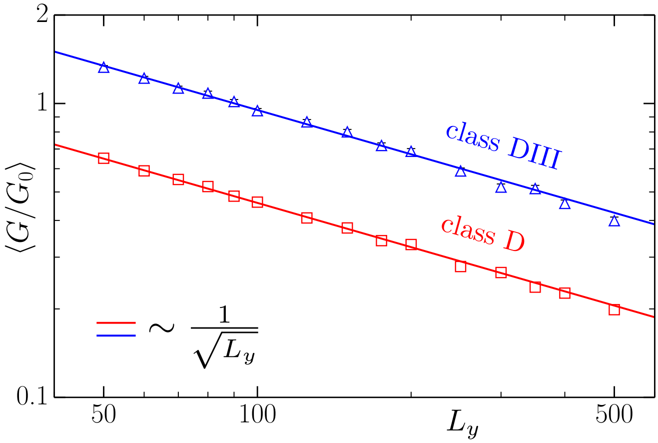

Figure 4.11. Disorder-averaged thermal conductance in the WTI phase of class D and DIII, at fixed $L_x = 50$ and varying L_y. Data points are averaged over 4000 disorder realizations, for $\mu = 0$, $\delta = 1.5\,t$, other parameters as in Fig. 4.10. Solid lines show the expected $L_y^{-1/2}$ scaling in the log-log plot.

invariant [90],

$$Q_{\rm K} = \text{sign}\,(\text{Pf}\,A^+)(\text{Pf}\,A^-), \tag{4.18}$$

determined by the Pfaffians of a pair of real antisymmetric matrices $A^\pm$, having nonzero matrix elements

$$A^\pm_{n,n+1} = -A^\pm_{n+1,n} = \kappa_n, \quad 1 \leq n \leq 2N-1, \tag{4.19a}$$
$$A^\pm_{2N,1} = -A^\pm_{1,2N} = \pm\kappa_{2N}. \tag{4.19b}$$

Evaluation of the Pfaffians gives

$$Q_{\rm K} = \text{sign}\left(\prod_{n=1}^{N} \kappa^2_{2n-1} - \prod_{n=1}^{N} \kappa^2_{2n}\right). \tag{4.20}$$

Translational invariance of the disorder ensemble means two completely different things for the Kitaev edge and for the Kitaev chain. For the Kitaev edge it means that the coupling strengths κ_n between adjacent Majorana's all have the same distribution. The disorder average $\langle Q_{\rm K}\rangle$ of the topological invariant then vanishes, which is why the Kitaev edge is called a *critical* WTI [68]. In contrast, as illustrated in Fig. 4.1, for the Kitaev chain translational invariance means that the κ_n's with n even or those with n odd have the same distribution, but the distributions of κ_{2n} and κ_{2n-1} are unrelated. The topological invariant is then nonzero on average, so the Kitaev chain is *not critical* [108, 71].

The implication for the transmission probability T follows if we remove the coupling between γ_{2N} and γ_1, so that we can introduce transmission and reflection amplitudes $t = 1/\cosh\alpha$, $r = \tanh\alpha$. The Lyapunov exponent α determines both T and $Q_{\rm K}$,

$$Q_{\rm K} = \operatorname{sign}\alpha, \;\; T = 1/\cosh^2\alpha, \tag{4.21}$$

and has a Gaussian distribution $P(\alpha)$ [23, 71]. The variance $\operatorname{Var}\alpha = L/\ell$ is determined by the mean free path ℓ for backscattering along the edge, of length $L \gg \ell$. The mean $\langle\alpha\rangle = L/\xi$ defines the localization length ξ. A vanishing $\langle Q_{\rm K}\rangle$ implies that the median of $P(\alpha)$ is zero, and since it's Gaussian also $\langle\alpha\rangle = 0 \Rightarrow \xi = \infty$.

For the Kitaev chain $\langle Q_{\rm K}\rangle \neq 0$ and hence ξ is finite, so the transmission probability has a log-normal distribution peaked at $T = e^{-2L/\xi}$, with an exponentially decaying average transmission [108, 71]. In contrast, for the Kitaev edge $\langle Q_{\rm K}\rangle = 0 \Rightarrow \langle\alpha\rangle = 0 \Rightarrow \xi = \infty$. The Gaussian distribution of the Lyapunov exponent then produces a *bimodal* distribution of the transmission probability for $L \gg \ell$,

$$\begin{aligned} P(T) &= \int_{-\infty}^{\infty} d\alpha\, \delta(T - 1/\cosh^2\alpha)(2\pi L/\ell)^{-1/2} e^{-\alpha^2\ell/2L} \\ &= (\ell/2\pi L)^{1/2}\, T^{-1}(1-T)^{-1/2} \\ &\qquad \times \exp\bigl[-(\ell/2L)\operatorname{arcosh}^2(T^{-1/2})\bigr], \end{aligned} \tag{4.22}$$

peaked near $T = 0$ and $T = 1$, with average decaying algebraically as $\langle T\rangle = \sqrt{2\ell/\pi L}$.

We have tested the result (4.22) in a computer simulation of the anisotropic p-wave superconductor, with class-D Hamiltonian (4.3). In the geometry of Fig. 4.2*b* both edges at $x = 0$ and $x = L_x$ contribute to the thermal conductance in the WTI phase, but one edge can be removed by reducing the width of the contacts to the interval $0 \le x \le L_x/2$. Results are shown in Fig. 4.12. With the mean free path ℓ as a single fit parameter, the transition from a uni-modal distribution to a bimodal distribution upon increasing L/ℓ is well-described by Eq. (4.22).

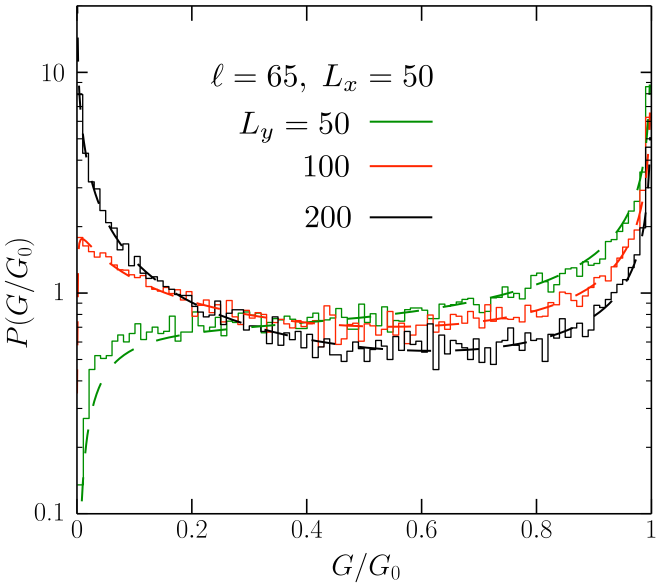

Figure 4.12. Disorder-induced thermal conductance distribution of a single edge in the WTI phase of the anisotropic p-wave superconductor in symmetry class D, for fixed $L_x = 50$ and varying L_y. The histograms are calculated numerically ($\delta = t$, other parameters as in Fig. 4.11). Dashed lines show the analytical result (4.22) for $T \equiv G/G_0$, $L \equiv L_y$, with the mean free path $\ell = 65$ as single fit parameter.

4.5 Electrical detection of Kitaev edge modes

So far we considered thermal conduction as the probe of edge state transport. Electrical detection would be more convenient experimentally, and this is possible by adapting the nanowire setup of Ref. [3]. All contacts are now at the same temperature T_0, the superconductor is grounded as well as one of the metal contacts (number 2), and the other contact (number 1) is biased at voltage V_1. The electrical current into the grounded contact 2 fluctuates in time with noise power P_{12}. This is dominated by shot noise, at low temperatures when thermal noise can be neglected ($k_B T_0 \ll eV_1$).

The noise power is given in terms of the transmission matrix by [8]

$$\begin{aligned} P_{12}/P_0 &= \mathrm{Tr}\,(t_{ee}^\dagger t_{ee} + t_{he}^\dagger t_{he}) - \mathrm{Tr}\,(t_{ee}^\dagger t_{ee} - t_{he}^\dagger t_{he})^2 \\ &= \tfrac{1}{2}\,\mathrm{Tr}\,t^\dagger t - \tfrac{1}{2}\,\mathrm{Tr}\,(\tau_z t^\dagger \tau_z t)^2, \end{aligned} \tag{4.23}$$

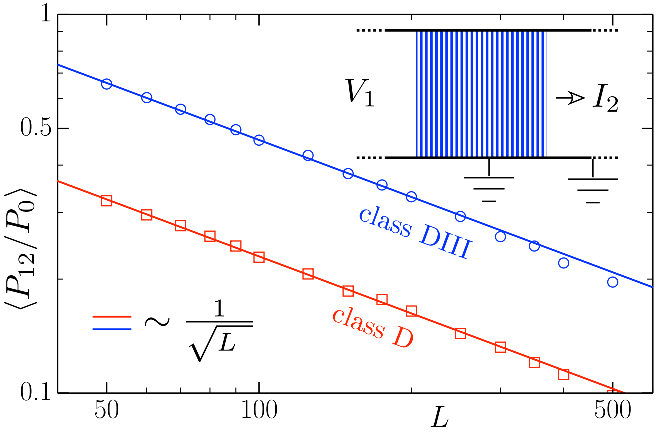

Figure 4.13. Disorder-averaged electrical shot noise power (4.23) in the WTI phase of class D and DIII, for parameters as in Fig. 4.11. Data points are averaged over 10^4 disorder realizations. The solid lines show that this electrical transport property obeys the same $L^{-1/2}$ scaling as the thermal transport property of Fig. 4.11. The inset shows the geometry, with one metal contact biased at voltage V_1 and both the superconductor and the second metal contact grounded. The electrical current I_2 into this second contact fluctuates in time with noise power $P_{12} = \int_{-\infty}^{\infty} dt\, \langle \delta I_2(0) \delta I_2(t) \rangle$.

with $P_0 = e^3 V_1/h$. The subscripts e, h indicate transmission from electron to electron (t_{ee}) or from electron to hole (t_{he}), and we used electron-hole symmetry in the second equation to rewrite the whole expression in terms of the full transmission matrix t.

As derived in Ref. [3], when the transmission is via an unpaired Majorana mode, the second trace in Eq. (4.23) vanishes identically so the electrical shot noise is directly related to the thermal conductance: $P_{12}/P_0 = \frac{1}{2} G/G_0$. This applies to symmetry class D. More generally, in both symmetry classes D and DIII the two quantities P_{12} and G have the same $1/\sqrt{L}$ scaling in the WTI phase[2], compare Figs. 4.11 and 4.13.

---

[2] The first trace in Eq. (4.23) is proportional to the transmission probability T, while the second trace is proportional to T^2. Because of the bimodal distribution (4.22), the averages of T and T^2 scale with the same power of L: $\langle T^2 \rangle = \frac{2}{3} \langle T \rangle \propto \sqrt{1/L}$. Incidentally, we note that this also implies that the "thermal Fano factor" $F = \langle T(1-T) \rangle \langle T \rangle^{-1}$ has the same L-independent value 1/3 as the electrical Fano factor of a metallic diffusive conductor — even though the conductance in that system has a Gaussian rather than bimodal distribution.

4.6 Conclusion

The Kitaev model [90] is paradigmatic for topological superconductivity and Majorana zero-modes, and for that reason has been studied extensively [91, 6]. Here we have shown that the realization of this model at the edge of a two-dimensional system (what we have called the “Kitaev edge”) is fundamentally different from its strictly one-dimensional counterpart, the Kitaev chain. The difference, summarized in Fig. 4.1, manifests itself in the different distribution of the thermal conductance, peaked at exponentially small value in the Kitaev chain [108, 24, 25, 71] while the Kitaev edge has a second peak at the conductance quantum.

As a possible physical realization of Kitaev edge modes we have studied in some detail a model of an anisotropic two-dimensional chiral p-wave superconductor [9, 68, 152, 27], as well as its time-reversally symmetric (helical) counterpart. Both can produce weak topological insulators (WTI) with Kitaev edge modes, but while they appear at any amount of anisotropy for chiral p-wave pairing, the helical p-wave pairing requires a threshold anisotropy (compare Figs. 4.3 and 4.6). We have demonstrated the robustness of the WTI phase to disorder by numerical simulations, in good agreement with analytical calculations of the phase boundaries in self-consistent Born approximation (Figs. 4.4 and 4.7).

Experimentally the transition into the WTI phase can be detected, on length scales below the mean free path, via the doubling of the thermal conductance (Fig. 4.10), and on larger length scales via the super-Ohmic scaling (Fig. 4.11). Because of the complexity of thermal transport measurements at low temperatures, we have proposed an alternative fully electrical method of detection, using the electrical shot noise power (Fig. 4.13).

4.7 Appendix

4.7.1 Calculation of the phase boundaries in self-consistent Born approximation

We calculate the phase diagram in the presence of electrostatic disorder (strength δ as defined in the main text) using the self-consistent Born approximation (SCBA). Below we provide details of the calculation for the class-DIII Hamiltonian (4.4). The corresponding results for the class-D Hamiltonian (4.3) are simply obtained by taking the vanishing coupling

$K \to 0$ limit and are summarized at the end of this Appendix.

We calculate the disorder-averaged density of states from the self-energy Σ, defined by

$$\frac{1}{E + i0^+ - H_{\text{DIII}} - \Sigma} = \left\langle \frac{1}{E + i0^+ - H_{\text{DIII}} - H_{\text{disorder}}} \right\rangle . \tag{4.24}$$

The SCBA self-energy at the Fermi level ($E = 0$) is given by

$$\Sigma = \tfrac{1}{3}\delta^2 \sum_{\boldsymbol{k}} \tau_z \frac{1}{i0^+ - H_{\text{DIII}}(\boldsymbol{k}) - \Sigma} \tau_z . \tag{4.25}$$

The sum over $\boldsymbol{k}$ ranges over the first Brillouin zone and in the continuum limit

$$\sum_{\boldsymbol{k}} \mapsto \frac{1}{4\pi^2} \int_{-\pi}^{\pi} dk_x \int_{-\pi}^{\pi} dk_y . \tag{4.26}$$

The SCBA self-energy is a $\boldsymbol{k}$-independent 4×4 matrix with spin and electron-hole degrees of freedom

$$\Sigma = (\sigma_0 \otimes \tau_z)\delta\mu - (\sigma_y \otimes \tau_y)\delta K - (\sigma_0 \otimes \tau_0) i\gamma . \tag{4.27}$$

The terms $\delta\mu$ and δK renormalize the chemical potential and coupling respectively. Both terms account for a disorder induced shift of the phase boundaries between the trivial insulator, TI, WTI, and thermal metal. The term γ produces a finite density of states, induced by the disorder. Such a finite density of states may indicate a thermal metal or a trivial Anderson insulator, but it cannot distinguish between the two.

We substitute the self-energy (4.27) into Eq. (4.25) and observe that the right-hand-side depends only on the renormalized chemical potential $\tilde{\mu} = \mu - \delta\mu$ and coupling $\tilde{K} = K - \delta K$. Denoting the renormalized Hamiltonian by $\tilde{H}_{\text{DIII}}(\boldsymbol{k}) \equiv H_{\text{DIII}}(\boldsymbol{k}) + (\sigma_0 \otimes \tau_z)\delta\mu - (\sigma_y \otimes \tau_y)\delta K$ we can write the following identity:

$$\begin{aligned} \Big(i\gamma - \tilde{H}_{\text{DIII}}(\boldsymbol{k})\Big)^{-1} &= \Big(i\gamma + \tilde{H}_{\text{DIII}}(\boldsymbol{k})\Big) \\ &\cdot \Big(\gamma^2 + f_{\tilde{\mu},\tilde{K}}(\boldsymbol{k}) - 2\tilde{K}(\Delta_x \sin k_x\, \sigma_z \tau_z + \Delta_y \sin k_y\, \sigma_y)\Big) \\ &\cdot \left(4\tilde{K}^2 g(\boldsymbol{k}) - \Big(\gamma^2 + f_{\tilde{\mu},\tilde{K}}(\boldsymbol{k})\Big)^2\right)^{-1} , \end{aligned} \tag{4.28}$$

where

$$g(\boldsymbol{k}) = \Delta_x^2 \sin^2 k_x + \Delta_y^2 \sin^2 k_y, \tag{4.29a}$$

$$f_{\tilde{\mu},\tilde{K}}(\boldsymbol{k}) = \epsilon_{\tilde{\mu}}(\boldsymbol{k})^2 + \tilde{K}^2 + g(\boldsymbol{k}). \tag{4.29b}$$

Because of symmetry only terms even in $\boldsymbol{k}$ contribute to $\sum_{\boldsymbol{k}}$. We find from Eq. (4.25) three coupled equations for the parameters $\delta\mu$, δK, and γ, which completely determine the SCBA self-energy:

$$\delta\mu = \tfrac{1}{3}\delta^2 \sum_{\boldsymbol{k}} \frac{\epsilon_{\tilde{\mu}}(\boldsymbol{k})(\gamma^2 + f_{\tilde{\mu},\tilde{K}}(\boldsymbol{k}))}{4\tilde{K}^2 g(\boldsymbol{k}) - (\gamma^2 + f_{\tilde{\mu},\tilde{K}}(\boldsymbol{k}))^2}, \tag{4.30a}$$

$$\delta K = \tfrac{1}{3}\delta^2 \sum_{\boldsymbol{k}} \tilde{K} \frac{\gamma^2 + f_{\tilde{\mu},\tilde{K}}(\boldsymbol{k}) - 2g(\boldsymbol{k})}{4\tilde{K}^2 g(\boldsymbol{k}) - (\gamma^2 + f_{\tilde{\mu},\tilde{K}}(\boldsymbol{k}))^2}, \tag{4.30b}$$

$$\gamma = \tfrac{1}{3}\delta^2 \sum_{\boldsymbol{k}} \frac{-\gamma(\gamma^2 + f_{\tilde{\mu},\tilde{K}}(\boldsymbol{k}))}{4\tilde{K}^2 g(\boldsymbol{k}) - (\gamma^2 + f_{\tilde{\mu},\tilde{K}}(\boldsymbol{k}))^2}. \tag{4.30c}$$

We address first the shift of phase boundaries in the weak disorder case. To this end we set $\gamma = 0$ assuming that the disorder is too weak to induce a finite density of states. We are looking for solutions of the clean system gap closing conditions Eqs. (4.11), (4.13), (4.14) expressed in terms of the renormalized parameters $\mu \to \tilde{\mu}$, $K \to \tilde{K}$. The gap closing condition defines the phase boundary and can be expressed as $\tilde{K} = \tilde{K}(\tilde{\mu})$ (with a different function $\tilde{K}(\tilde{\mu})$ for each boundary). We rewrite the SCBA equations (4.30) with $\gamma = 0$ in the form

$$\mu = \tfrac{1}{3}\delta^2 F(\tilde{\mu}, \tilde{K}) + \tilde{\mu}, \tag{4.31a}$$

$$\delta^2 = 3(K - \tilde{K}) \Big(G(\tilde{\mu}, \tilde{K})\Big)^{-1}, \tag{4.31b}$$

where

$$F(\tilde{\mu}, \tilde{K}) = \sum_{\boldsymbol{k}} \frac{\epsilon_{\tilde{\mu}}(\boldsymbol{k}) f_{\tilde{\mu},\tilde{K}}(\boldsymbol{k})}{4\tilde{K}^2 g(\boldsymbol{k}) - f^2_{\tilde{\mu},\tilde{K}}(\boldsymbol{k})}, \tag{4.32}$$

$$G(\tilde{\mu}, \tilde{K}) = \sum_{\boldsymbol{k}} \tilde{K} \frac{f_{\tilde{\mu},\tilde{K}}(\boldsymbol{k}) - 2g(\boldsymbol{k})}{4\tilde{K}^2 g(\boldsymbol{k}) - f^2_{\tilde{\mu},\tilde{K}}(\boldsymbol{k})}. \tag{4.33}$$

In this way we obtain the parametric solution for the disorder strength $\delta^2[\tilde{\mu}, \tilde{K}(\tilde{\mu})]$ and the gap parameter $\mu[\tilde{\mu}, \delta^2(\tilde{\mu})]$ along the phase boundary.

We vary the parameter $\tilde{\mu}$ away from the clean system solution μ at $\delta = 0$. The sums over the Brillouin zone are computed numerically in the continuum limit. The resulting parametric phase boundaries $[\mu(\tilde{\mu}), \delta(\tilde{\mu})]$ separate insulating and gapless phases at low to moderate disorder.

For sufficiently large disorder $\delta > \delta_c$ the SCBA equations (4.30) may support solutions with non-zero γ indicating the onset of a finite density of states at zero energy. This marks the transitions from the strong and weak topological insulators to the thermal metal at strong disorder. The δ_c dependence on μ and K follows from solutions of the SCBA equations at infinitesimal $\gamma \neq 0$

$$\begin{aligned} 1 &= \frac{\delta_c^2}{3} \sum_{\boldsymbol{k}} \frac{f_{\tilde{\mu},\tilde{K}}(\boldsymbol{k})}{f^2_{\tilde{\mu},\tilde{K}}(\boldsymbol{k}) - 4\tilde{K}^2 g(\boldsymbol{k})} \equiv \frac{\delta_c^2}{3} H(\tilde{\mu}, \tilde{K}), && \text{(4.34a)} \\ \tilde{\mu} &= -\tfrac{1}{3}\delta_c^2 F(\tilde{\mu}, \tilde{K}) + \mu, && \text{(4.34b)} \\ \tilde{K} &= -\tfrac{1}{3}\delta_c^2 G(\tilde{\mu}, \tilde{K}) + K. && \text{(4.34c)} \end{aligned}$$

To determine δ_c we first search numerically (using Steffensen iteration) for fixed point solutions of Eqs. (4.34b), (4.34c),

$$\begin{pmatrix} \tilde{\mu} \\ \tilde{K} \end{pmatrix} = \frac{-1}{H(\tilde{\mu}, \tilde{K})} \begin{pmatrix} F(\tilde{\mu}, \tilde{K}) \\ G(\tilde{\mu}, \tilde{K}) \end{pmatrix} + \begin{pmatrix} \mu \\ K \end{pmatrix}, \tag{4.35}$$

for a given value of the chemical potential μ and coupling K. Finally we compute δ_c from (4.34a) for the obtained solutions $(\tilde{\mu}, \tilde{K})$.

Both the parametric solutions to the renormalized gap closing conditions and the computed μ-dependence (for fixed K) of the critical disorder δ_c are shown as white dashed lines in Fig. 4.7.

This was all for class DIII. The formulas for class D correspond to the $K \to 0$ limit. Denoting by $E_\mu(\boldsymbol{k})$ the excitation spectrum of the class-D Hamiltonian (4.3) we find

$$E^2_\mu(\boldsymbol{k}) = f_{\mu,K\to 0}(\boldsymbol{k}) = \epsilon^2_\mu(\boldsymbol{k}) + \Delta_x^2 \sin^2 k_x + \Delta_y^2 \sin^2 k_y. \tag{4.36}$$

The shift of the phase boundaries at low disorder is obtained by imposing the gap closing conditions for the renormalized chemical potential $\tilde{\mu} = \pm 2t(1 \pm \alpha)$. From Eq. (4.31a) we directly obtain the boundary position as a function of the disorder strength

$$\mu = \left[-\tfrac{1}{3}\delta^2 \sum_{\boldsymbol{k}} \frac{\epsilon_{\tilde{\mu}}(\boldsymbol{k})}{E^2_{\tilde{\mu}}(\boldsymbol{k})} + \tilde{\mu} \right]\Bigg|_{\tilde{\mu} = \pm 2t(1\pm\alpha)}. \tag{4.37}$$

For the isotropic case $\alpha = 1$ the central $\mu = 0$ transition separating the two TI phases is not renormalized by disorder. The transitions separating the TI phases from the trivial insulator phase are shifted according to $\mu = \pm(4t + 0.130\,\delta^2)$. For $\alpha = 1/2$ the transition line between the WTI and TI phases is given by $\mu = \pm(3t + 0.039\,\delta^2)$ and the transition between TI and the trivial phase by $\mu = \pm(t + 0.180\,\delta^2)$. These phase boundaries are shown as dashed lines in Fig. 4.4.

The critical disorder lines separating the TI and WTI phases from the thermal metal at large disorder can be found from the SCBA solutions Eqs. (4.34a), (4.34b) at infinitesimal $\gamma \neq 0$. In class-D we can directly parametrize such solutions by the renormalized chemical potential $\tilde{\mu}$. We obtain

$$\delta_c^2(\tilde{\mu}) = 3\left(\sum_{\boldsymbol{k}} \frac{1}{E_{\tilde{\mu}}^2(\boldsymbol{k})}\right)^{-1}, \tag{4.38}$$

$$\mu\left[\tilde{\mu}, \delta_c(\tilde{\mu})\right] = \tilde{\mu} - \tfrac{1}{3}\delta_c^2(\tilde{\mu}) \sum_{\boldsymbol{k}} \frac{\epsilon_{\tilde{\mu}}(\boldsymbol{k})}{E_{\tilde{\mu}}^2(\boldsymbol{k})}. \tag{4.39}$$

The parametric dependence for $\tilde{\mu} \in [-4, 4]$ calculated from the above equations is also included in Fig. 4.4.

Chapter 5

Extended topological group structure due to average reflection symmetry

5.1 Introduction

Topological insulators (TI) are states of matter in which the bulk is gapped, but which host protected gapless edge states [73, 127]. This behavior was first studied in connection to the quantum Hall effect [72, 28], a two-dimensional system, and later generalized to include arbitrary dimensions, as well as boundary states protected by the fundamental symmetries of the system: time-reversal $\mathcal{T}$, particle-hole $\mathcal{P}$, and chiral symmetry $\mathcal{C}$ [92, 148]. In each case, the gapless nature of boundary states is a consequence of the system's bulk properties. This enables obtaining topological invariants, quantities determined from the bulk which count the number of protected states at a termination of the system. For single-particle systems, the group structure of topological invariants ($\mathbb{Z}$ or $\mathbb{Z}_2$) is listed in the so-called periodic table of topological insulators, which shows that in any dimension 5 out of the 10 Altland-Zirnbauer [7] (AZ) symmetry classes can be topologically non-trivial. As long as the protecting symmetries are not broken, the invariant cannot change without closing the bulk gap, explaining the robustness of the boundary states to perturbations such as disorder.

Topologically non-trivial behavior can occur also due to symmetries of the underlying lattice. This enables weak and crystalline topologi-

Table 5.1. Group structure of single-particle topological invariants in the ten AZ symmetry classes, with average reflection symmetry preserved along all directions. The strong invariants of the original TI table are shown in blue and those protected by ARS in black.

Symmetry class	Dimension		
	1	2	3
A		$\mathbb{Z}$	${\mathbb{Z}_2}^3$
AIII	$\mathbb{Z}$	${\mathbb{Z}_2}^2$	$\mathbb{Z}\times{\mathbb{Z}_2}^3$
AI			
BDI	$\mathbb{Z}$	${\mathbb{Z}_2}^2$	${\mathbb{Z}_2}^3$
D	$\mathbb{Z}_2$	$\mathbb{Z}\times{\mathbb{Z}_2}^2$	${\mathbb{Z}_2}^6$
DIII	$\mathbb{Z}_2$	$\mathbb{Z}_2\times{\mathbb{Z}_2}^2$	$\mathbb{Z}\times{\mathbb{Z}_2}^6$
AII		$\mathbb{Z}_2$	$\mathbb{Z}_2\times{\mathbb{Z}_2}^3$
CII	$\mathbb{Z}$	${\mathbb{Z}_2}^2$	$\mathbb{Z}_2\times{\mathbb{Z}_2}^3$
C		$\mathbb{Z}$	${\mathbb{Z}_2}^3$
CI			$\mathbb{Z}$

cal insulators in the presence of translational symmetry, or point group symmetries (rotation, reflection, etc.) [106, 136, 59, 63, 77]. Many generalizations of the periodic table have been considered by examining the interplay between $\mathcal{T}$, $\mathcal{P}$, $\mathcal{C}$, and different lattice symmetries [157, 79, 37, 4, 164, 191, 14, 107, 38].

Disorder breaks all symmetries of the lattice, leading to a distinction between *strong* and *weak* topological insulators (WTI) and their associated invariants. Despite owing their protection to lattice symmetries, the boundary states of some WTIs may still survive disorder. This was first shown for a stack of quantum spin-Hall layers [135, 105, 64], a three-dimensional WTI belonging to symmetry class AII in the AZ classification, and later generalized to systems of different dimensionality and symmetry class, dubbed statistical topological insulators [68]. Here, protection is not given by an exact symmetry, but by one which only holds on average. Whereas the original invariants belong to $\mathbb{Z}$ or $\mathbb{Z}_2$, those stabilized by average symmetries only have a $\mathbb{Z}_2$ group structure.

Motivated by the robustness of boundary states in statistical topological insulators, we study how the classification of TIs and topological defects are extended by average symmetries. For concreteness, we will focus on disordered systems which preserve average reflection symmetry (ARS), a situation which occurs in many condensed matter systems [162, 50, 188]. Each element of the disordered ensemble of Hamiltonians, H, appears with equal probability as its reflected counter part, $\mathcal{R}_j^{-1} H \mathcal{R}_j$, with $\mathcal{R}_j$ a unitary reflection operator about the j-direction. Oblique reflection gives the same physics as the ordinary one, thus in the examples we will consider only the ordinary one. For us the relevant cases are when the reflection plane passes through a lattice site of the system, such that the symmetry can be broken by staggering the strength of consecutive hopping amplitudes.

We find that the group structure of topological invariants is exponentially enlarged by ARS, since weak invariants of all dimensions $d > 0$ contribute simultaneously and independently to the classification presented in Table 5.1. Some of the physical consequences of this extension include the possibility of disordered topological phase transitions governed only by a change in the weak invariant. We find a particularly interesting situation when the system possesses a nonzero strong index on both sides of such a transition. Then the conductance of the boundary is non-trivial and identical in both phases, while at the transition the bulk gap must close in the presence of ARS. Additionally, we show that the extended classification applies also to topological defects [163]. It allows us to define a new class of gapless *statistical topological defects*, which are robust to disorder but can only exist in the presence of average symmetries.

In the following, we begin our discussion by motivating the need for an extended topological classification with some concrete examples. In Section 5.2 we introduce a model for a two-dimensional (2d) topological superconductor in symmetry class D, exhibiting disordered phase transitions across which the strong invariant remains constant, and only a weak index changes. To show how this behavior escalates in higher dimensions, we consider a three-dimensional topological superconductor (class DIII) in Section 5.3. Its disordered phases are distinguished by a second generation weak index, *i.e.* one which is two dimensions lower than the system dimension, even if the strong and 2d weak invariants don't change. We generalize these results to arbitrary dimension and symmetry class in Section 5.4 showing that ARS enlarges the topological classification of both bulk Hamiltonians and topological defects alike. We conclude in Section 5.5.

5.2 Topological superconductor in class D

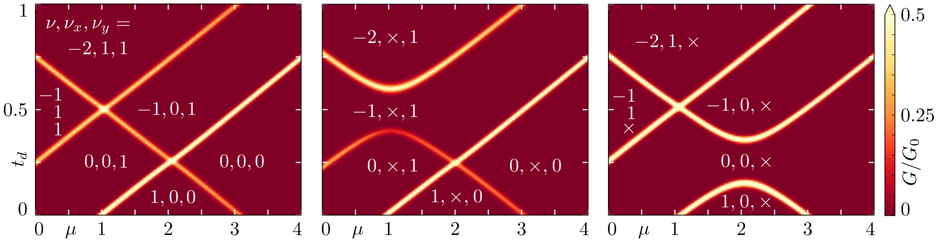

Figure 5.1. Bulk thermal conductance of a disordered system with Hamiltonian (5.2) as a function of μ and t_d. Parameters are $t_x = 1$, $t_y = 1/2$, $\Delta_x = 2$, $\Delta_y = 1$, and disorder strength $U = 1$. Each phase is labeled according to its strong and weak topological invariants: ν, ν_x, ν_y. With average reflection symmetry (left panel) the crossings are protected by the weak invariants. Breaking ARS in either the x- or the y-directions destroys the corresponding invariant (marked with $\times$) and leads to an anticrossing, as shown in the middle and right panels. In the middle panel the staggering strength in the x-direction is $s_x = 0.2$, while in the right panel the y-direction hoppings are staggered with $s_y = 0.4$.

5.2.1 Model Hamiltonian

Two-dimensional superconductors with broken time-reversal as well as spin-rotation symmetry belong to symmetry class D in the AZ classification. The minimal topological model is a 2×2 Bogoliubov-De Gennes Hamiltonian describing spinless fermions in the presence of a p-wave order parameter, $\Delta(\mathbf{k}) \sim \mathbf{k}$. The only constraint is provided by the particle-hole symmetry, and reads:

$$\tau_x H(\mathbf{k}) \tau_x = -H^*(-\mathbf{k}), \tag{5.1}$$

in terms of the Pauli matrices τ_i acting on the particle-hole degree of freedom.

We use a tight binding Hamiltonian of the form

$$H(\mathbf{k}) = \varepsilon(\mathbf{k})\tau_z + \Delta_x \tau_x \sin(k_x) + \Delta_y \tau_y \sin(k_y), \tag{5.2}$$

with

$$\begin{aligned} \varepsilon(\mathbf{k}) \quad = \quad & -2t_x \cos(k_x) - 2t_y \cos(k_y) - \mu \\ & -2t_d \cos(k_x + k_y) - 2t_d \cos(k_x - k_y). \end{aligned} \tag{5.3}$$

Here, $\Delta_{x,y}$ is the strength of the p-wave pair potential, $t_{x,y}$ are the anisotropic hopping amplitudes in the x- and y-directions, and μ is the chemical potential. The Hamiltonian (5.2) is discretized on a square lattice of $L_x \times L_y = 50 \times 50$ sites (lattice constant $a = 1$), with the last two terms of Eq. (5.3) leading to next nearest neighbor hoppings, parametrized by the diagonal hopping amplitude t_d. Disorder is modeled by random variations of the chemical potential, drawn independently for each site from the uniform distribution $[\mu - U, \mu + U]$. In the following we set $t_x = 1$ and express all other Hamiltonian parameters relative to this energy scale. All tight binding simulations are performed using the Kwant code [70].

5.2.2 Group structure of phases distinguished by strong and weak invariants

We attach disorder free leads at $x = 0, L_x$ connecting the system to reservoirs at temperatures T_0 and $T_0 + \delta T$. The Fermi level ($E = 0$) scattering matrix,

$$S = \begin{pmatrix} r & t \\ t' & r' \end{pmatrix}, \tag{5.4}$$

enables us to compute the thermal conductance $G = G_0 \operatorname{Tr} t^\dagger t$, $G_0 = \pi^2 k_{\mathrm{B}}^2 T_0 / 6h$, in the low-temperature, linear response regime, as well as the topological invariants of the system. The Chern number, the strong topological invariant of the system, reads [66, 65]

$$\nu = \frac{1}{2\pi i} \int_0^{2\pi} d\phi \, \frac{d}{d\phi} \ln \det r(\phi), \tag{5.5}$$

while the weak $\mathbb{Z}_2$ invariants are given by

$$(-1)^{\nu_y} = \operatorname{sign} \det r(\phi = 0). \tag{5.6}$$

In Eqs. (5.5) and (5.6) $r(\phi)$ is the reflection block of the scattering matrix in the presence of twisted boundary conditions applied to the states in the y direction: $\psi(x, 0) = e^{i\phi} \psi(x, L_y)$. The weak invariant in the x-direction is evaluated in a similar fashion, by attaching leads in the y-direction and using periodic boundary conditions ($\phi = 0$) along x. Both the strong and the weak invariant is defined such that ν, $\nu_y = 0$ is trivial, while phases with non-zero invariants are non-trivial, either in the strong or weak sense.

As a function of μ and t_d, the system shows a variety of topological phases separated by phase transitions at which the bulk gap closes (see Fig. 5.1, left panel). The phases are strong topological insulators whenever the Chern number is nonzero, with chiral Majorana zero modes on all edges. When $\nu = 0$, we also find weak topological insulators, where two out of four edges avoid localization in the presence of disorder, hosting counter-propagating Majorana edge modes – so-called Kitaev edges [48].

While typically the Chern number changes across a phase transition, in the model (5.2) there are also transitions across which the strong invariant remains constant, and only the weak invariants change. They are the crossings in Fig. 5.1, occurring at $(\mu, t_d) = (1, 1/2)$ and $(2, 1/4)$. At $t_d = 1/4$, varying the chemical potential causes a change of the weak invariant ν_y, while the other weak invariant, ν_x, is responsible for the phase transition at $t_d = 1/2$. The bulk gap is closed at $(\mu, t_d) = (2, 1/4)$ even though there are the same number of chiral Majorana edge modes with the same chirality both for $\mu < 2$ and $\mu > 2$.

In the clean case ($U = 0$) these anomalous topological phase transitions are protected by the exact reflection symmetry of the system. We find in our simulations that they persist when disorder is added, up to values of U comparable to the bulk gap, when a thermal metal phase develops [150, 51, 103]. Note that in Fig. 5.1 we plot the bulk thermal conductance of a *single* system at strong disorder, showing that at large enough system sizes ARS can protect not only the properties of the disordered ensemble as a whole, but its individual elements as well. The presence of crossings in the disordered phase diagram of Hamiltonian (5.2) shows that the Chern number, a $\mathbb{Z}$ index, is insufficient to describe class D two-dimensional disordered superconductors with ARS. The full topological classification is in fact $\mathbb{Z} \times {\mathbb{Z}_2}^2$.

We verify this group structure by selectively removing average symmetries from the system. This is done by staggering the x- and/or y-direction hoppings as $t_{x,y} \to t_{x,y}(1 + (-1)^{x,y} s_{x,y})$. For $s \neq 0$, consecutive hoppings in the same direction have alternating strength, such that ARS no longer holds. Breaking either of the average symmetries removes the protection of the associated weak invariant, and therefore splits the corresponding crossing, as shown in the middle and right panels of Fig. 5.1. This signals that the two average symmetries act independently, justifying the extended $\mathbb{Z} \times {\mathbb{Z}_2}^2$ group structure.

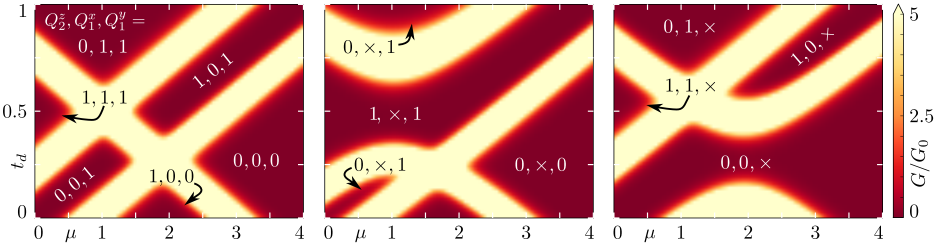

Figure 5.2. Bulk thermal conductance of a single disordered system with Hamiltonian (5.7) as a function of μ and t_d. Parameters are $t_x = 1$, $t_y = 1/2$, $t_z = 0.05$, $\Delta_x = 3$, $\Delta_y = 1.5$, $\Delta_z = 0.15$, $K = 0.2$, and disorder strength $U = 1$. Phases are labeled by their topological invariants Q_2^z, Q_1^x, and Q_1^y, with × marking an invariant destroyed by breaking ARS. In the absence of staggering, phases are distinguished by both first and second generation weak invariants (left panel). Staggering in the x- and y-directions are set to $s_x = 0.25$ in the middle panel and $s_y = 0.5$ in the right panel, respectively.

5.3 Topological superconductor in class DIII

5.3.1 Model Hamiltonian

To demonstrate the protection of an insulating phase by a second generation weak invariant, *i.e.* an invariant two dimensions lower than the system dimension, we choose a model in symmetry class DIII, with Hamiltonian

$$\begin{aligned} H(\boldsymbol{k}) = \varepsilon(\boldsymbol{k})\sigma_0 \otimes \tau_z + K\sigma_y \otimes \tau_y + \Delta_x \sin(k_x)\sigma_z \otimes \tau_x \\ + \Delta_y \sin(k_y)\sigma_o \otimes \tau_y + \Delta_z \sin(k_z)\sigma_x \otimes \tau_x, \end{aligned} \tag{5.7}$$

where

$$\begin{aligned} \varepsilon(\boldsymbol{k}) = -2t_x \cos(k_x) - 2t_y \cos(k_y) - 2t_z \cos(k_z) \\ - 2t_d \cos(k_x + k_y) - 2t_d \cos(k_x - k_y). \end{aligned} \tag{5.8}$$

The Pauli matrices τ_i and σ_i act on the particle-hole and time-reversal degree of freedom, respectively. Here, $t_{x,y,z}$ and $\Delta_{x,y,z}$ are the anisotropic hopping amplitudes and the p-wave pairing amplitudes in the x-, y-, and z-directions (as before, we set $t_x = 1$). The chemical potential is μ, while K models an s-wave order parameter coupling the two spin blocks. The model is constrained by particle-hole and time-reversal symmetry:

$$\tau_x H(\boldsymbol{k})\tau_x = -H^*(-\boldsymbol{k}), \tag{5.9}$$

$$\sigma_y H(\boldsymbol{k})\sigma_y = H^*(-\boldsymbol{k}). \tag{5.10}$$

5.3.2 Group structure of phases distinguished by first and second generation weak invariants

Like in the previous model, we introduce disorder by random spatial variations of the chemical potential, with disorder strength U. We discretize the Hamiltonian (5.7) on a cubic lattice of linear size $L_{x,y,z} = 16$. Ideal leads are attached along one direction, and twisted boundary conditions are imposed in the other two, as $\psi(0, y, z) = e^{i\phi_x}\psi(L_x, y, z)$, $\psi(x, 0, z) = e^{i\phi_y}\psi(x, L_y, z)$, or $\psi(x, y, 0) = e^{i\phi_z}\psi(x, y, L_z)$. In each case the reflection matrix is a function of two out of the three twist angles $\phi_{x,y,z}$. Owing to time-reversal symmetry, the reflection block can be brought to an antisymmetric form whenever the twist angles are 0 or π (periodic or antiperiodic boundary conditions), making its Pfaffian, $\mathrm{Pf}\, r$, well defined. As in the class D model, the system shows different disordered topological phases as a function of μ and t_d, protected by 1d or 2d weak invariants (see Fig. 5.2). The relevant two-dimensional weak index reads [66, 65]

$$\begin{aligned}(-1)^{Q_2^z} = \mathrm{sign}\,[&\mathrm{Pf}\, r(\phi_y = 0, \phi_z = 0) \times \\ &\mathrm{Pf}\, r(\phi_y = \pi, \phi_z = 0)]\,,\end{aligned} \tag{5.11}$$

and is responsible for gapless modes on all side surfaces, *i.e.* surfaces parallel to the z-direction. Non-trivial 1d weak invariants appearing in Fig. 5.2 are

$$(-1)^{Q_1^x} = \mathrm{sign}\,[\mathrm{Pf}\, ir(\phi_x = 0, \phi_z = 0)]\,, \tag{5.12}$$

and

$$(-1)^{Q_1^y} = \mathrm{sign}\,[\mathrm{Pf}\, ir(\phi_y = 0, \phi_z = 0)]\,, \tag{5.13}$$

leading to protected gapless modes on side surfaces parallel to the x- and y-directions, respectively. Three-dimensional class DIII systems also allow for a strong invariant, but this one remains zero throughout the phase diagram of Fig. 5.2, since the top and bottom surfaces are insulating whenever the bulk is gapped.

Unlike the two-dimensional model of Section 5.2, in which topologically different phases were separated by insulator-to-insulator phase transitions, the three dimensional Hamiltonian (5.7) has finite-extent metallic regions [67]. Nevertheless, insulating phases are not connected in the presence of ARS. We find that the weak 1d and 2d invariants are robust, leading to surfaces which do not localize once disorder is added. Breaking average reflection symmetry by staggering consecutive hoppings in the x- or y-directions destroys the corresponding invariants, connecting the phases as shown in the middle and right panels of Fig. 5.2. Note that staggering in the z-direction destroys all of the invariants of Eqs. (5.11), (5.12), and (5.13), turning the entire phase diagram into a topologically trivial insulator.

5.4 Extended topological classification

In the previous Sections we have presented models showing topological phase transitions protected by average reflection symmetry, which we dub statistical topological phase transitions, following nomenclature of Ref. [68]. Since the strong index remains constant across these transitions, we need to extend the topological group structure of the periodic TI table in order to properly label the protected phases. In this Section, we discuss this extension in the context of the models presented above, and show how it applies to systems of any dimensionality and symmetry class.

5.4.1 Topological protection in 2d, class D

The phase diagram of the 2d system, Fig. 5.1, has two statistical topological phase transitions. The lower one, $\mu = 2$ and $t_d = 1/4$, happens at a vanishing Chern number, $\nu = 0$. The corresponding phases are a trivial system ($\nu = \nu_y = 0$), $\mu > 2$, and a WTI ($\nu_y = 1$) for $\mu < 2$. As such, its robustness to disorder can be understood in the language of Ref. [68], namely in terms of the different edge localization properties of the two phases. In the trivial phase the edge is localized: its thermal conductance $G \sim \exp(-L/\xi)$ decays exponentially as a function of system size L, with the localization length ξ. The WTI on the other hand has edge states which avoid localization even in the presence of disorder. They form so-called Kitaev edges [48], characterized by a super-Ohmic conductance $G \sim \sqrt{l/L}$ (with l the mean free path), which scales in a way typical for disordered one-dimensional systems at a critical point [23, 24, 108, 71]. Due to bulk-boundary correspondence, the difference in edge localization

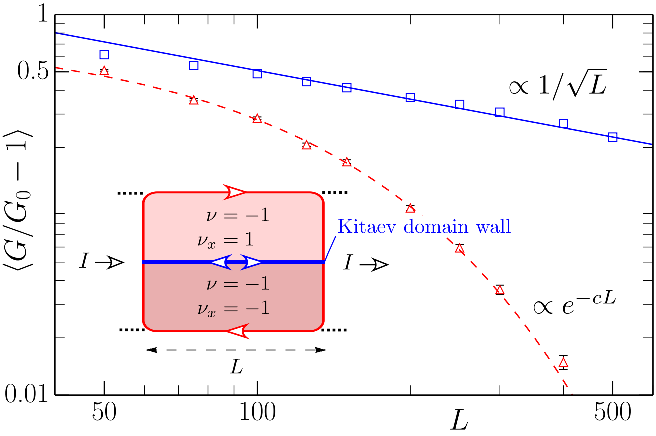

Figure 5.3. Conductance through a Kitaev domain wall as a function of its length, with and without average reflection symmetry (blue solid and red dashed, respectively). The inset shows the measurement setup, in which conductance flows both through the domain wall and the chiral Majorana edge modes. The quantized edge mode contribution has been subtracted from the plot (vertical axis label). Both the top and bottom halves are described by Eq. (5.2), using $\mu_{\text{top}} = 1.5$ and $\mu_{\text{bottom}} = 0.5$, and keeping all other parameters the same as in Fig. 5.1.

properties implies that the two phases are topologically distinct, explaining the phase transition's robustness to disorder.

The situation is different for the upper crossing in Fig. 5.1, at $\mu = 1$ and $t_d = 1/2$. On both sides the strong topological invariant is $\nu = -1$, and as such all edge states avoid localization in both phases. In fact, the thermal conductance of the edge is identical in both systems, $G = |\nu|G_0 = G_0$, so the above argument cannot be applied.

Instead, we look at the localization properties of an interface formed between them. Consider a one-dimensional domain wall formed between systems in the two phases ($t_d = 1/2$, $\mu < 1$ and $\mu > 1$). The key observation is that if one of the weak indices differs, the corresponding interface between two strong TIs will behave like the edge of a WTI – in this case a Kitaev edge, or rather, a *Kitaev domain wall*. Since the index ν_x changes, the interface parallel to the x-direction avoids localization as long as average reflection symmetry is preserved (see Fig. 5.3). The mobility gap must close along this interface, showing that the two phases are topologically distinct. Therefore, ARS protects weak invariants also when the strong index is nonzero, leading to a $\mathbb{Z} \times {\mathbb{Z}_2}^2$ classification for disordered class D systems in two dimensions.

5.4.2 Topological protection in 3d, class DIII

The situation is similar for the 3d model in class DIII, whose phase diagram is shown in Fig. 5.2. At $t_d = 1/4$, the systems goes from a WTI with $Q_1^y = 1$ to a trivial insulator as a function of μ, so the different surface localization properties of the two disordered phases imply they are topologically distinct. At $t_d = 1/2$ on the other hand, the effect of 1d invariants is obscured by the 2d non-trivial invariant Q_2^z, which makes all side surfaces delocalized. As before, robustness of the topological phases on either side of the crossing can be determined by considering an interface between them. Our simulations indicate that in this case the interface avoids localization, such that the two phases cannot be continuously connected without closing the mobility gap.

5.4.3 Generalized topological protection by average symmetry

In general, strong and multiple generations of weak invariants may affect the localization properties of states at the same boundary. However, contributions of different indices can always be isolated by forming an interface between two phases with only one index changed. This is, in fact, analogous to studying the boundaries of a system which is only non-trivial with respect to that particular invariant (see Fig. 5.4).

For a d-dimensional Hamiltonian H, the robustness of one of its topological indices can be determined by studying an auxiliary Hamiltonian in the same symmetry class [163, 182]:

$$\widetilde{H} = H \oplus H'_{\mathrm{R}} \equiv \begin{pmatrix} H & \Lambda \\ \Lambda^\dagger & H'_{\mathrm{R}} \end{pmatrix}, \tag{5.14}$$

with Λ a symmetry preserving coupling matrix. Choosing H'_{R} such that only one nonzero index of H is also nonzero in $\widetilde{H}$, with all others trivial, allows us to use the results of Ref. [68] to show its boundaries avoid localization in the presence of average symmetries.

For example, if H is given by Eq. (5.2) with $\nu = -1$, $\nu_x = 1$, as happens for $\mu = 0$ and $t_d = 1/2$, one can choose H'_{R} to have $\nu = 1$, $\nu_x = 0$,

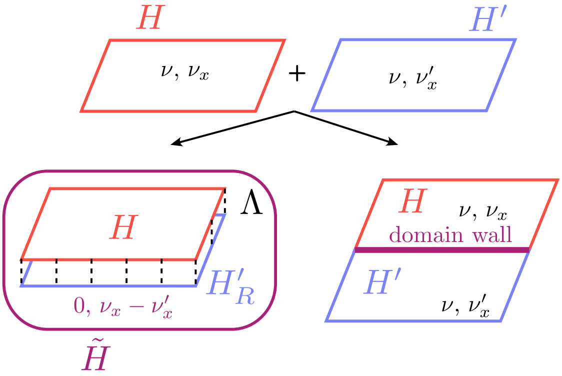

Figure 5.4. We consider two systems with the same strong indices ν, but different weak indices ν_x and ν'_x corresponding to the Hamiltonians H and H'. We combine them in one of two ways: on the left we invert the invariants of the second system to H'_R with indices $-\nu$ and $-\nu'_x$ and combine it with the first system using Eq. (5.14). We make the coupling matrix Λ local and having support throughout the bulk of both systems. The combined system has indices 0 and $\nu_x - \nu'_x$ making it non-trivial only in the weak sense. On the right we put the two systems together with a coupling only over their common edge. Then a weak domain wall is formed with gapless states protected by the non-zero difference $\nu_x - \nu'_x$. This is the generalization of the Kitaev domain wall introduced earlier.

making the combined system [163, 182, 129] a WTI only with respect to ν_x. The connection between the Kitaev domain wall formed at the interface between two strong TIs and the auxiliary Hamiltonian introduced in Eq. (5.14) is summarized in Fig. 5.4. The combined Hamiltonian can be visualized as the system in the inset of Fig. 5.3, where the two halves touching at the domain wall have been folded on top of each other. The Majorana edge modes become counter-propagating after folding, such that $\nu = 0$, and the domain wall in the original setup becomes the boundary of the folded system. As such, in the following we will restrict ourselves to boundary localization properties, with the understanding that the same results will be reached when multiple non-trivial invariants coexist, either by considering interface properties, or auxiliary Hamiltonians of the form (5.14).

Before proceeding to extend the table of topological insulators to the case where average reflection symmetry is preserved, we shortly review the results of Ref. [68]. We give here only a brief summary, expressed in

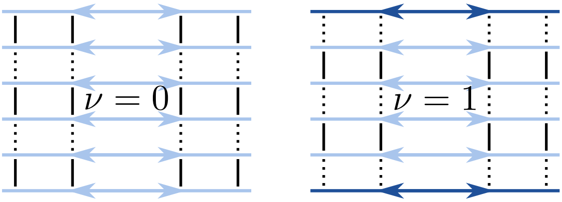

Figure 5.5. Surface of a stack of quantum spin Hall layers. Horizontal arrows denote the helical edge modes of each layer, and solid/dotted lines indicate strong/weak inter-layer coupling. Reflection symmetry about one layer can be broken in two different ways (left/right panels), leading to different surface invariants ν. On the left the surface is gapped and trivial, whereas on the right the reflected configuration of inter-layer coupling leaves helical edge modes on the surface boundaries (dark color), signaling a non-trivial surface invariant $\nu = 1$.

the language of a concrete physical example, and refer the reader to that paper for the full, detailed derrivation. This discussion is necessary in order to distinguish between $\mathbb{Z}$ and $\mathbb{Z}_2$ weak invariants.

In the absence of disorder, WTIs have gapless boundary states. They can be thought of as systems formed of weakly coupled layers, where each one caries a strong lower dimensional invariant. Depending on whether the layer index is $\mathbb{Z}$ or $\mathbb{Z}_2$, we consider two constructions: adjacent layers can either have the same value of a $\mathbb{Z}_2$ index, or opposite $\mathbb{Z}$ invariants, Q and $-Q$. A 3d example of the former is a stack of weakly coupled quantum spin Hall systems [135], while the latter is an anti-ferromagnetic stack of quantum Hall systems [104, 10]. In each case, dimerization of the layers can gap out the boundary states, but this is forbidden by exact reflection symmetry.

Note that one can also consider stacked systems in which each layer has the same value of a $\mathbb{Z}$ invariant. In this construction however, the boundary cannot be gapped irrespective of lattice symmetries, so we will not discuss it in the following.

When disorder is added, reflection symmetry is explicitly broken, becoming instead an average symmetry of the disordered ensemble. Let us use the stack of coupled quantum spin Hall systems as an example, and assume that the gapless surfaces protected by exact reflection symmetry do indeed become gapped once disorder is introduced. In the presence of a surface gap, we can define surface topological invariants for all elements of the disordered ensemble. Since in 2d (and in general in all dimensions

$d \geq 1$) the topological invariant is a self-averaging quantity, it should have the same value for any surface as it does for its reflected counterpart. However, there are two distinct ways of breaking reflection symmetry on the surfaces of a stack of quantum spin Hall layers, with surface invariants that differ by an odd amount, as shown in Fig. 5.5. Disorder which respects ARS is equally likely to break reflection symmetry in either of the two ways, seemingly contradicting the self-averaging nature of the topological index. The only resolution to this apparent paradox is to invalidate the original assumption, that of a gapped surface.

Ref. [68] showed that boundary states avoid localization whenever the average symmetry changes surface invariants by an odd amount, resulting in a new class of topological phases: statistical topological insulators. With average reflection symmetry, this happens for layered systems in which each layer has a strong $\mathbb{Z}_2$ index, since a change of a $\mathbb{Z}_2$ number can only be odd. Additionally, it was shown this happens for layers with an alternating $\mathbb{Z}$ index $\pm Q$, whenever Q itself is odd. As such, both cases lead to a weak invariant of the disordered bulk system which is $\mathbb{Z}_2$.

The weak invariants found to survive disorder thanks to the above arguments can then be used iteratively to extend the classification to higher dimensional systems. This is done by studying a system in the same symmetry class but one higher dimension, and considering odd changes in the *weak* surface invariants. Then, the same procedure leads to second generation statistical topological insulators, such as the phase appearing at $\mu = t_d = 0$ in the DIII model (Fig. 5.2). The simultaneous presence of two independent average reflection symmetries is required in this case: one guarantees the existence of a weak surface invariant, while the second one changes the value of this weak invariant by an odd amount. Therefore, each strong index, $\mathbb{Z}$ or $\mathbb{Z}_2$, gives rise to infinitely many higher dimensional $\mathbb{Z}_2$ statistical topological insulators in the same symmetry class, which require a larger number of average symmetries for larger dimensionality of the system.

5.4.4 Extended topological group structure

So much for the summary of Ref. [68]. We extend its conclusions to the case when multiple invariants coexist. For a d-dimensional system in any symmetry class, the classification due to the strong invariant, if any, is extended by each non-trivial invariant of lower dimension, $d' = d - k$, as

$$\mathbb{Z}_2{}^{\alpha}, \qquad \alpha = \binom{N}{k}, \tag{5.15}$$

where α is a binomial coefficient and $N \leq d$ is the total number of average reflection symmetries. The binomial coefficient in Eq. (5.15) is reminiscent of that found for systems in the absence of disorder [92, 182], with some important differences. First, it does not go up to the full dimension of the system, but rather to the number of average reflection symmetries which protect the invariants. Second, only $\mathbb{Z}_2$ groups appear, irrespective of whether the lower dimensional index is $\mathbb{Z}$ or $\mathbb{Z}_2$. Lastly, the extension only involves invariants in dimensions $d > d' > 0$, since in zero dimensions the topological invariant is not a self-averaging quantity, making the results of Ref. [68] inapplicable.

We assemble the resulting classification into a new table of topological insulators, which is now no longer periodic, but shows an exponential enlargement of groups with the number of spatial dimensions (see Table 5.1). In two dimensions we recover the result of Section 5.2 for class D, with a group structure $\mathbb{Z}\times\mathbb{Z}_2{}^2$. In 3d class DIII (Section 5.3), the group is $\mathbb{Z}\times\mathbb{Z}_2{}^6$ with ARS along all directions: there is one integer valued strong index, three 2d weak indices, and three second generation, 1d invariants. If ARS is broken along one direction, by staggering the system for instance, the group becomes $\mathbb{Z} \times \mathbb{Z}_2{}^3$ instead. In that case, only two 2d invariants and one 1d weak index survive.

The extended classification of Table 5.1 applies not only to bulk Hamiltonians, but also to Teo and Kane's classification of topological defects [163], enabling us to distinguish between *strong* and *statistical* topological defects. An example of the latter is in fact shown in Fig. 5.3. It's the Kitaev domain wall, a one-dimensional topological defect protected from localization by ARS.

Since topological defects are classified in terms of the topological properties of Hamiltonians surrounding the defect, they share the same extended group structure as bulk Hamiltonians. Therefore, statistical topological phase transitions in which the strong defect invariant does not change are possible. By using the same interface construction as before, Fig. 5.3, one can understand these transitions in terms of the properties of the Hamiltonians surrounding them. We show an example in Fig. 5.6, where the Hamiltonians surrounding two defects with the same strong in-

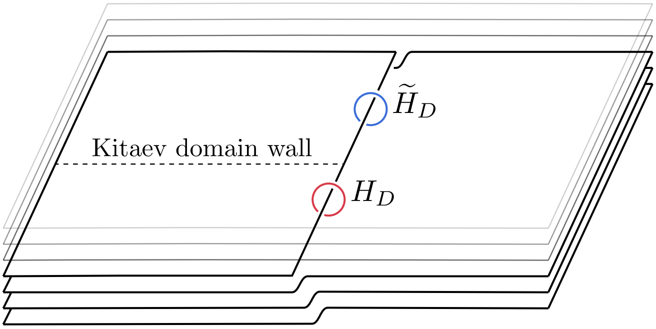

Figure 5.6. One-dimensional topological defect embedded in a three-dimensional bulk, such as the Hamiltonian (5.7) or stacked copies of (5.2). At some point along the defect one of its weak invariants changes, leading to the formation of a Kitaev domain wall. The defect Hamiltonians H_D and $\widetilde{H}_D$ have the same strong invariant, but cannot be deformed into each other without closing a gap, due to the presence of ARS.

variant cannot be adiabatically deformed into each other, since they differ in one of their weak invariants.

5.5 Conclusion

We have shown how the topological structure of single-particle systems is enhanced by the presence of average symmetries. For concreteness, we have focused on protection due to average reflection symmetry in the presence of disorder, a situation which occurs naturally in many condensed matter systems. We have found that all weak invariants of lower dimensions $d \geq 1$ contribute to the classification at the same time, leading to a group structure which grows exponentially with the number of dimensions.

In general, when multiple invariants affect the localization properties of the same boundaries, the effect of average symmetries can be treated with the construction of Eq. (5.14), or by forming interfaces between systems. This enables the robustness of each invariant to be studied independently of the others.

Since we focus on the effects of disorder, our classification scheme is different from, and applies also to existing works which generalize the periodic TI table. The same arguments can be applied to any symmetry compatible with the criterion of Ref. [68]. In particular, one may consider instead rotational symmetry, which has also been shown to lead to topologically non-trivial phases and defects [79, 164, 14]. Here too the inclusion of disorder would result in an average rotational symmetry, extending the topological group structure in a similar fashion. This opens possibilities for numerous theoretical studies and widens the possibilities for the experimental observation of the suggested effects.

We have also discussed some of the physical consequences of the extended classification. It can lead to statistical topological phase transitions, governed only by a change in one of the weak invariants. In the presence of average symmetries the bulk gap must close at the transition, even if the topological insulators on either side have the same boundary conductance. Additionally, the extended classification can lead to statistical topological defects, which host gapless modes that are robust to disorder, but which could not exist in the absence of average symmetries.

Chapter 6

Emergence of massless Dirac fermions in graphene's Hofstadter butterfly at switches of the quantum Hall phase connectivity

6.1 Introduction

The quantum Hall effect in a two-dimensional periodic potential has a phase diagram with a fractal structure called the "Hofstadter butterfly" [75, 119]. In a 2013 breakthrough, three groups reported [124, 45, 78] the observation of this elusive structure in a graphene superlattice, produced by the moiré effect when graphene is deposited on a boron nitride substrate with an almost commensurate hexagonal lattice structure. It was found that the magnetic minibands repeat in a self-similar way at rational values $\Phi/\Phi_0 = p/q$ of the flux Φ through the superlattice unit cell, with p, q integers and $\Phi_0 = h/e$ the flux quantum.

A central theme of studies of the Hofstadter butterfly is the search for flux-induced massless Dirac fermions [128, 76, 69, 46, 133]. It turns out that in the graphene superlattice only the zero-field Dirac cones are approximately gapless [140, 118, 189, 89], while the flux-induced Dirac cones are gapped [35]. Generically, Dirac fermions in the Hofstadter butterfly

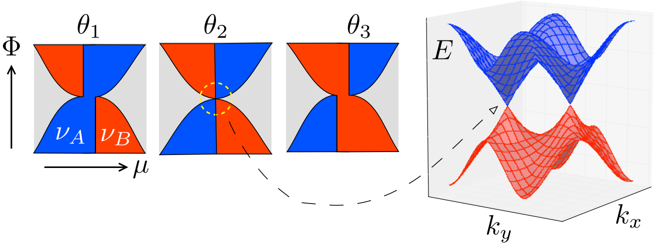

Figure 6.1. Schematic illustration of a connectivity switch in the quantum Hall phase diagram. Upon variation of a control parameter θ the connected component switches from topological quantum number ν_A to ν_B. At the transition a singular point appears in the phase boundary (encircled), associated with gapless Dirac cones in the Brillouin zone (right-most panel).

are massive.

Here we show that massless Dirac fermions do appear at singular points in the quantum Hall phase diagram, associated with a switch of the phase connectivity upon variation of some control parameter. (See Fig. 6.1.) Any experimentally accessible quantity that couples to the superlattice potential can play the role of control parameter, in what follows we will consider the angle θ of crystallographic alignment between graphene and substrate. We find that the phase boundaries separating regions of distinct Hall conductance $\sigma_{xy} = \nu e^2/h$ rearrange their connectivity upon variation of θ, switching the connected component of the phase diagram from ν to $\nu \pm 2q$. In the magnetic Brillouin zone this transition produces a pair of q-fold degenerate conical singularities (Dirac points), with massless Dirac fermions as low-energy excitations.

6.2 Low energy model of the moiré superlattice

We base our analysis on the moiré superlattice Hamiltonian of Wallbank *et al.* [179]. Starting point is the Dirac Hamiltonian of graphene [31, 87],

$$H_0 = v[\boldsymbol{p} - e\boldsymbol{A}(\boldsymbol{r})] \cdot \boldsymbol{\sigma} + V(\boldsymbol{r}), \tag{6.1}$$

for conduction electrons near each of two opposite corners (valleys) of the hexagonal Brillouin zone[1]. The Fermi velocity is $v = 10^6$ m/s and the lat-

---

[1] The valley-isotropic Dirac Hamiltonian (6.1) acts on the spinor $(\Psi_\mathrm{A}, \Psi_\mathrm{B})$ in valley K and $(\Psi_\mathrm{B}, -\Psi_\mathrm{A})$ in valley K', where $\Psi_\mathrm{A}, \Psi_\mathrm{B}$ are the wave amplitudes on the two triangular sublattices that form the hexagonal lattice of graphene.

tice constant of the hexagonal lattice of carbon atoms is $a = 2.46\,\text{Å}$. The momentum $\boldsymbol{p} = -i\hbar\nabla$ in the $\boldsymbol{r} = (x, y)$ plane is coupled to pseudospin Pauli matrices σ_x and σ_y acting on the sublattice degree of freedom. The real spin plays no role and is ignored[2], only the orbital effect of a perpendicular magnetic field $\boldsymbol{B} = B\hat{z}$ is included (via the vector potential $\boldsymbol{A}$). The electrostatic potential V is adjustable via a gate voltage. For simplicity we assume that the mean free path for impurity scattering is sufficiently large that disorder effects can be neglected.

The moiré effect from a substrate of hexagonal boron nitride (hBN, lattice constant $(1 + \delta)a$, $\delta = 0.018$, misaligned by $\theta \ll 1$) adds superlattice terms to the Dirac Hamiltonian. The terms that break inversion symmetry are small and we neglect them, following Ref. [1]. Three terms remain [179],

$$\begin{aligned} H = {} & H_0 + \hbar v b U_1 f_+(\boldsymbol{r}) + i\xi\hbar v b U_2 \sigma_z f_-(\boldsymbol{r}) \\ & + i\xi\hbar v U_3 \left(\sigma_y \partial f_-/\partial x - \sigma_x \partial f_-/\partial y\right), \end{aligned} \tag{6.2}$$

where $\xi = \pm 1$ in the two valleys and

$$f_\pm(\boldsymbol{r}) = \sum_{m=0}^{5} (\pm 1)^m e^{i\boldsymbol{b}_m \boldsymbol{r}} = \pm f_\pm(-\boldsymbol{r}), \tag{6.3}$$

$$\boldsymbol{b}_m = \frac{4\pi}{\sqrt{3}a} \hat{R}_{\pi m/3} \left[1 - (1 + \delta)^{-1} \hat{R}_\theta\right] \begin{pmatrix} 0 \\ 1 \end{pmatrix}. \tag{6.4}$$

The reciprocal lattice vectors $\boldsymbol{b}_m$ have length $b \equiv |\boldsymbol{b}_0| \approx (4\pi/\sqrt{3}a)\sqrt{\delta^2 + \theta^2}$ and are rotated by the matrix

$$\hat{R}_\theta = \begin{pmatrix} \cos\theta & -\sin\theta \\ \sin\theta & \cos\theta \end{pmatrix}. \tag{6.5}$$

The periodicity of the superlattice is $\lambda = 4\pi/\sqrt{3}b \approx a/\sqrt{\delta^2 + \theta^2}$.

The terms U_1 and U_2 in the Hamiltonian (6.2) represent a potential modulation, while the term U_3 is a modulation of the hopping amplitudes. The coefficients are related by [89, 179]

$$\{U_1, U_2, U_3\} = \frac{E_0}{\hbar v b} \left\{\tfrac{1}{2}, -\tfrac{1}{2}\sqrt{3}, -(1 + \theta^2/\delta^2)^{-1/2}\right\}, \tag{6.6}$$

---

[2] Because the spin degree of freedom is not counted, the conductance quantum is e^2/h rather than $2e^2/h$.

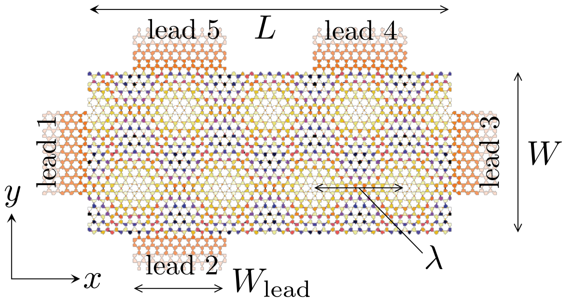

Figure 6.2. Five-terminal geometry used to calculate the Hall conductivity (6.7). The two-dimensional hexagonal lattice of the tight-binding model is shown, with the superlattice potential indicated by colored sites and bonds (not to scale, the actual lattice is much finer).

where E_0 is an energy scale that sets the coupling strength of graphene to the hBN substrate. We use the estimate $E_0 = 17\,\text{meV}$ from Ref. [1], corresponding to a ratio $E_0/\hbar vb = 0.05\,(1+\theta^2/\delta^2)^{-1/2}$.

6.3 Numerical results for the Hall conductivity

We study electrical conduction in the five-terminal Hall bar geometry of Fig. 6.2, where a current I flows from source 1 to drain 3 while contacts 2, 4, and 5 draw no current. The voltages V_n at these contacts determine the Hall conductivity,

$$\sigma_{xy} = \frac{(V_5 - V_2)I}{(V_5 - V_2)^2 + (W/L)^2(V_5 - V_4)^2}. \tag{6.7}$$

In linear response and at zero temperature the voltage differences are obtained from the scattering matrix $S(E)$ at the Fermi level $E_\text{F} = 0$, which we calculate by discretizing the Hamiltonian (6.2) on a tight-binding lattice (hexagonal symmetry, lattice constant $a_\text{TB} = \lambda/20$). The metallic contacts are modeled by heavily doped graphene leads (infinite length, width $W_\text{lead} = 5\lambda$, potential $V_\text{lead} = 2\,\hbar vb$), without the superlattice ($E_0 = 0$ in the leads) and without magnetic field. In the superlattice region (length $L = 20\lambda$, width $W = 5\sqrt{3}\lambda$) we set $V = -\mu$. (The sign of μ is chosen such that the Fermi level lies in the conduction band of graphene for $\mu > 0$ and in the valence band for $\mu < 0$.) We calculate σ_{xy} as a function of Φ and μ using the KWANT tight-binding code [70][3]. Results are shown in Fig. 6.3.

Panel 6.3*a* shows the known spectral features of the graphene superlattice [124, 45, 78, 35]: A parabolic fan of Landau levels emerging from the primary zero-field Dirac cone of graphene; secondary zero-field Dirac cones centered at $\mu = \pm\hbar vb/2$; and gapped tertiary Dirac cones at flux $\Phi/\Phi_0 = p/q$ in a region near $\mu = -\hbar vb/2$ (in the valence band only, electron-hole symmetry is strongly broken by the superlattice potential). The phases that meet at these rational flux values have Hall conductance differing by $2qe^2/h$ — reflecting a two-fold valley degeneracy and a q-fold degeneracy of the magnetic minibands. (We are not counting spin.)

Panels 6.3*b*–*d* show how the connectivity switches from Fig. 6.1 appear in the numerical simulation when we slightly misalign the hBN lattice relative to the graphene lattice. Each switch in the connected component of the phase diagram is associated with the closing and reopening of the Dirac cones in the magnetic Brillouin zone. (The gap closing at $\Phi = \Phi_0$ is the one shown in Fig. 6.1.)

6.4 Transport signatures of massless Dirac fermions

We will now demonstrate that transport properties near these connectivity switches have the characteristics of massless Dirac fermions [11]. The effects we consider are the scale-invariant (pseudodiffusive) two-terminal conductivity and sub-Poissonian shot noise at the Dirac point [85, 171], and Klein tunneling through a potential step [86, 34].

6.4.1 Scale-invariant conductivity and sub-Poissonian shot noise

To search for scale invariance we take an infinitely long graphene strip of width W, with the potential profile shown in Fig. 6.4*a*. The superlattice potential is imposed over a length L (where $V = -\mu$), while the leads have no superlattice ($V_{\text{lead}} = \hbar vb$). The two-terminal conductivity σ and Fano factor F (ratio of noise power and current) are obtained from the transmission eigenvalues T_n,

$$\sigma = \frac{L}{W}\frac{e^2}{h}\sum_n T_n, \quad F = \frac{\sum_n T_n(1-T_n)}{\sum_n T_n}. \tag{6.8}$$

---

[3] Details of the calculation are given in the Appendix.

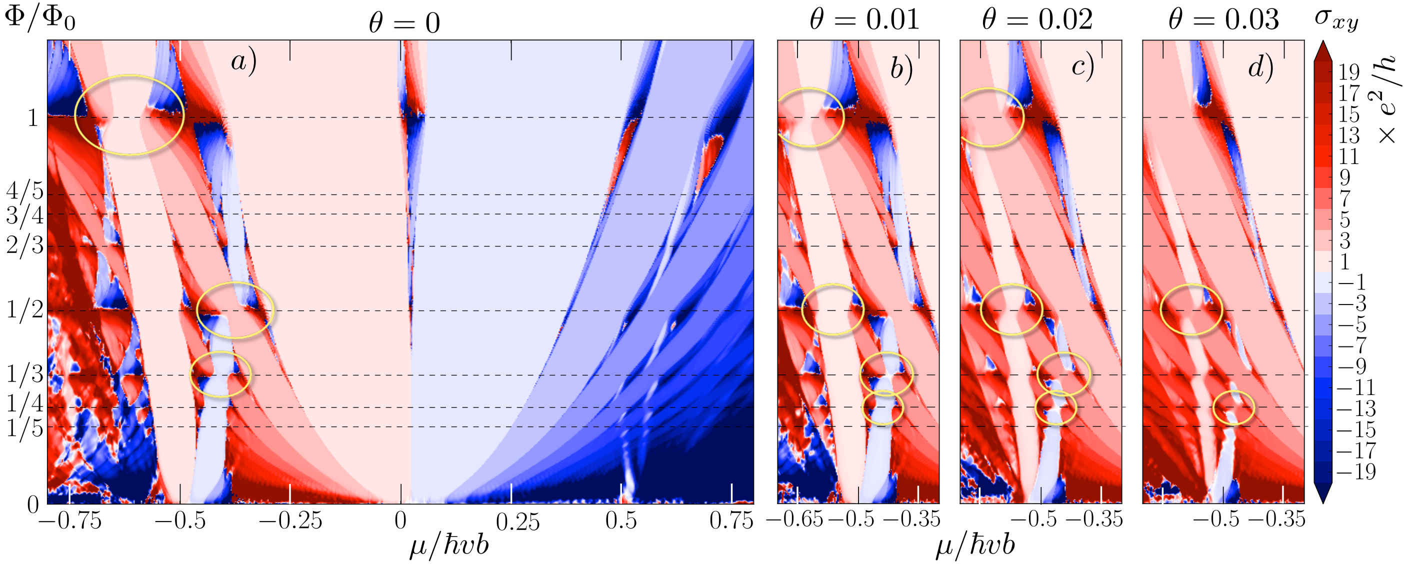

Figure 6.3. Numerical results for the Hall conductivity of graphene on hBN, calculated in the Hall bar geometry of Fig. 6.2 for the superlattice Hamiltonian (6.2). Panel *a* is for a perfectly aligned substrate, when the flux-induced Dirac cones (encircled) are all gapped. Panels *b*,*c*,*d* show the connectivity switches induced by a slight crystallographic misalignment of the substrate (angle θ in radians).

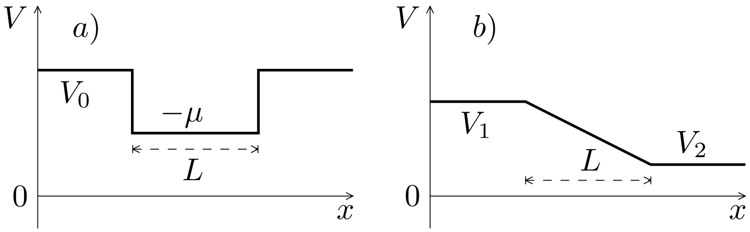

Figure 6.4. Electrostatic potential profile in a graphene strip, used to study the scale invariant conductivity (panel *a*, $V_0/\hbar vb = 1$, varying μ) and Klein tunneling (panel *b*, $V_1/\hbar vb = 0.645$, $V_2/\hbar vb = 0.613$). The Fermi level $E_F = 0$ lines up with the flux-induced Dirac point when $V \approx 0.63\,\hbar vb$.

For $2q$ gapless Dirac cones we expect at the Dirac point the scale invariant values [85, 171]

$$\sigma_D = 2qe^2/\pi h, \quad F_D = 1/3. \tag{6.9}$$

We vary W at fixed aspect ratio W/L to search for this scale invariance. We have examined several flux values, here we show representative results for $\Phi = \Phi_0$ (so $q = 1$). From Fig. 6.3 we infer that the connectivity switch at this flux value happens near $\theta = 0.01$ and $\mu = -0.6\,\hbar vb$. Indeed, in Fig. 6.5 both σ and F become approximately independent of sample size near these parameter values. The limiting Fano factor is close to the expected 1/3; the limiting conductivity is a bit larger than the expected value, which we attribute to an additional contribution of order $(L/W)e^2/h$ from edge states. These are zero-temperature calculations, but the characteristic temperature scale can be quite large for a sample of the size shown in Fig. 6.5, where the required energy resolution is of order $0.01\,\hbar vb \simeq 40\,\mathrm{K}$.

6.4.2 Klein tunneling

Klein tunneling is the transmission with unit probability at normal incidence on a potential step that crosses the Dirac point. It is a direct manifestation of the chirality of massless Dirac fermions [86]. We search for this effect using the potential profile of Fig. 6.4*b*, which for $\Phi = \Phi_0$ and $\theta = 0.01$ is symmetrically arranged around the flux-induced Dirac point. In order to avoid spurious reflections from the leads we now apply the superlattice potential and the magnetic field to an unbounded graphene plane. We calculate the transmission probability $T(k_y)$ as a function of transverse wave vector k_y in the magnetic Brillouin zone.

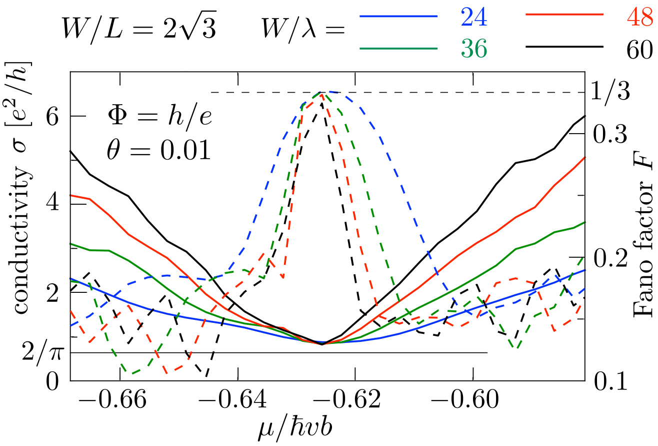

Figure 6.5. Conductivity (solid curves, left axis) and Fano factor (dashed curves, right axis) calculated in the two-terminal graphene strip of Fig. 6.4*a*, for different system sizes at fixed aspect ratio W/L. The scale invariance at $\mu \approx -0.63\,\hbar v b$ signals the appearance of massless Dirac fermions at flux $\Phi = h/e$ through the superlattice unit cell. The horizontal solid and dashed lines indicate the limits (6.9) expected from the Dirac equation.

The dependence on the angle of incidence ϕ of the transmission probability of massless Dirac fermions depends exponentially on the step length L [34],

$$T(\phi) = \exp(-\pi\hbar^{-1}p_{\rm F}L\sin^2\phi), \tag{6.10}$$

for a symmetric junction with the same Fermi momentum $p_{\rm F}$ at both sides of the potential step. (The step should be smooth on the scale of the lattice constant, so $L \gg \lambda$ is assumed.) The transverse momentum appearing in the Dirac equation is measured from the Dirac point, $p_y = \hbar(k_y - K_y)$. (The flux $\Phi = \Phi_0$ creates two Dirac cones, both with the same value of K_y.) Inspection of the band structure gives $K_y = 1.723/\lambda$ and Fermi velocity $v_{\rm F} = 2.04\,v$, nearly twice the native Fermi velocity v of graphene. The angle of incidence then follows from $\sin\phi = p_y/p_{\rm F}$, with $p_{\rm F} = 0.23\,\hbar/\lambda$, so we expect a transmission peak described by

$$T(k_y) = \exp(-\pi\hbar L(k_y - K_y)^2/p_{\rm F}). \tag{6.11}$$

The resulting curves are shown in Fig. 6.6 (dashed curves), for different values of L. There is a good agreement with the numerical simulations (solid curves).

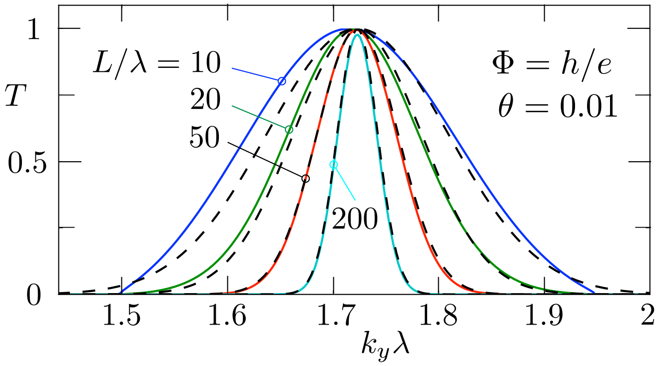

Figure 6.6. Transmission probability T through the potential step of Fig. 6.4b, as a function of transverse wave vector k_y for different step lengths L. The flux-induced Dirac point is at $k_y = 1.723/\lambda$. The solid curves result from the numerical simulation of the graphene superlattice at $\Phi = \Phi_0$, $\theta = 0.01$, the dashed curves are the analytical prediction (6.11) for Klein tunneling of massless Dirac fermions. (There is no fit parameter in this comparison.)

The angle-resolved detection in these simulations is convenient to directly access the strongly peaked transmission profile (6.11). Experimentally this signature of Klein tunneling can be observed without requiring angular resolution in a double potential step geometry [190].

6.5 Conclusion

In summary, we have identified a mechanism for the production of massless Dirac fermions in the Hofstadter butterfly spectrum of a moiré superlattice. Generically, the flux-induced clones of the zero-field Dirac cones are gapped, but the gap closes at a switch in the connected component of the quantum Hall phase diagram. We have presented a model calculation for graphene on an hexagonal boron nitride surface that exhibits these connectivity switches upon variation of the crystallographic misalignment. Only a slight misalignment is needed, on the order of 1°, comparable to what has been realized in experiments [124, 45, 78, 187]. Numerical simulations of transport properties at unit flux through the superlattice unit cell reveal the scale invariant conductivity and Klein tunneling that are the characteristic signatures of ballistic transport of massless Dirac fermions. These should be observable in small samples, in larger samples the effects of disorder remain as an interesting problem for further research.

6.6 Appendix

6.6.1 Derivation of the tight-binding Hamiltonian for the moiré superlattice

Our numerical simulations are based on a tight-binding discretization of the moiré superlattice Hamiltonian (6.2) for graphene on an hexagonal substrate. Here we provide a derivation of the tight-binding Hamiltonian, arriving at Eq. (6.28). This is not quite straightforward, because of the need to accomodate two lattices, of graphene and of the substrate, in a single discretization. We start with zero magnetic field ($\boldsymbol{A} = 0$).

In order to achieve a commensurate discretization of the bare graphene Hamiltonian (6.1) and the moiré superlattice defined by reciprocal lattice vectors $\boldsymbol{b}_m(\theta)$, for arbitrary alignment angle θ, we make use of the invariance of H_0 under a simultaneous rotation of space and pseudospin (sublattice degree of freedom). A rotation by

$$-\phi = -\arctan\left(\frac{\sin\theta}{\cos\theta - (1+\delta)}\right) \tag{6.12}$$

leaves H_0 invariant,

$$v\boldsymbol{p}\cdot\boldsymbol{\sigma} + V(\boldsymbol{r}) \mapsto v\tilde{\boldsymbol{p}}\cdot\tilde{\boldsymbol{\sigma}} + \tilde{V}(\tilde{\boldsymbol{r}}), \tag{6.13}$$

while bringing the reciprocal lattice vectors in alignment with $\boldsymbol{b}_m(\theta = 0)$.

The first two terms of the moiré modulation transform into

$$\begin{aligned} &\hbar v b U_1 f_+[\boldsymbol{r}(\tilde{x},\tilde{y})] + i\xi\hbar v b U_2 f_-[\boldsymbol{r}(\tilde{x},\tilde{y})]\sigma_z \\ &\qquad = \hbar v b U_1 \tilde{f}_+(\tilde{\boldsymbol{r}}) + i\xi\hbar v b U_2 \tilde{f}_-(\tilde{\boldsymbol{r}})\tilde{\sigma}_z, && (6.14)\\ &\tfrac{1}{2}\tilde{f}_+(\tilde{\boldsymbol{r}}) = \cos(\boldsymbol{g}_1\tilde{\boldsymbol{r}}) + \cos(\boldsymbol{g}_3\tilde{\boldsymbol{r}}) + \cos(\boldsymbol{g}_5\tilde{\boldsymbol{r}}), && (6.15)\\ &\tfrac{1}{2}i\tilde{f}_-(\tilde{\boldsymbol{r}}) = \sin(\boldsymbol{g}_1\tilde{\boldsymbol{r}}) + \sin(\boldsymbol{g}_3\tilde{\boldsymbol{r}}) + \sin(\boldsymbol{g}_5\tilde{\boldsymbol{r}}). && (6.16) \end{aligned}$$

The rotated reciprocal superlattice vectors

$$\boldsymbol{g}_1 = \frac{b}{2}\begin{pmatrix}-\sqrt{3}\\ 1\end{pmatrix},\ \boldsymbol{g}_3 = b\begin{pmatrix}0\\ -1\end{pmatrix},\ \boldsymbol{g}_5 = \frac{b}{2}\begin{pmatrix}\sqrt{3}\\ 1\end{pmatrix}, \tag{6.17}$$

depend on θ only in their length $b = (4\pi/\sqrt{3}a)\sqrt{\delta^2+\theta^2}$, but unlike $\boldsymbol{b}_m$ not in their direction.

The third term of the moiré modulation transforms into

$$\begin{aligned} i\xi\hbar v U_3 \Bigg[& -\frac{f_-[\boldsymbol{r}(\tilde{x},\tilde{y})]}{\partial\tilde{y}}\frac{\partial y}{\partial\tilde{y}}\left(\tilde{\sigma}_x\cos\phi-\tilde{\sigma}_y\sin\phi\right) \\ & + \frac{f_-[\boldsymbol{r}(\tilde{x},\tilde{y})]}{\partial\tilde{x}}\frac{\partial x}{\partial\tilde{x}}\left(\tilde{\sigma}_y\cos\phi+\tilde{\sigma}_x\sin\phi\right)\Bigg] = \xi\mathcal{A}_x(\tilde{\boldsymbol{r}})\tilde{\sigma}_x+\xi\mathcal{A}_y(\tilde{\boldsymbol{r}})\tilde{\sigma}_y . \end{aligned} \tag{6.18}$$

We have introduced the fictitious vector potential

$$\boldsymbol{\mathcal{A}}(\tilde{\boldsymbol{r}}) = \begin{pmatrix} \mathcal{A}_x(\tilde{\boldsymbol{r}}) \\ \mathcal{A}_y(\tilde{\boldsymbol{r}}) \end{pmatrix} = -\hbar v b U_3 \begin{pmatrix} \cos(\boldsymbol{g}_1\tilde{\boldsymbol{r}})+\cos(\boldsymbol{g}_5\tilde{\boldsymbol{r}})-2\cos(\boldsymbol{g}_3\tilde{\boldsymbol{r}}) \\ \sqrt{3}[\cos(\boldsymbol{g}_1\tilde{\boldsymbol{r}})-\cos(\boldsymbol{g}_5\tilde{\boldsymbol{r}})] \end{pmatrix} . \tag{6.19}$$

The full Hamiltonian in the rotated basis reads

$$\begin{aligned} \tilde{H} = {} & v\tilde{\boldsymbol{p}}\cdot\tilde{\boldsymbol{\sigma}}+\tilde{V}(\tilde{\boldsymbol{r}})+\xi\hbar v b U_1\tilde{f}_+(\tilde{\boldsymbol{r}})+i\xi\hbar v b U_2\tilde{f}_-(\tilde{\boldsymbol{r}})\tilde{\sigma}_z \\ & +\xi\boldsymbol{\mathcal{A}}(\tilde{\boldsymbol{r}})\cdot\tilde{\boldsymbol{\sigma}} \ . \end{aligned} \tag{6.20}$$

In the following we will work in this rotated basis, but in favor of a simple notation we will drop the tilde ˜.

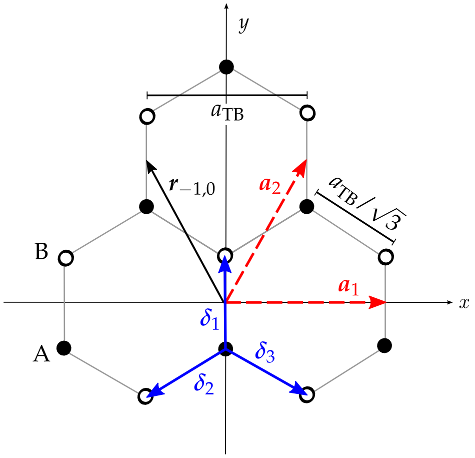

Figure 6.7. Hexagonal lattice of the tight-binding model, with lattice vectors $\boldsymbol{a}_1$, $\boldsymbol{a}_2$ and nearest-neighbor displacement vectors $\boldsymbol{\delta}_1$, $\boldsymbol{\delta}_2$, $\boldsymbol{\delta}_3$. The two sublattices have sites labeled A (filled dots) and B (open dots). The vector $\boldsymbol{r}_{ij} = i\boldsymbol{a}_1 + j\boldsymbol{a}_2$ denotes the center of unit cell (i, j).

We discretize the Hamiltonian (6.20) in the rotated basis on the hexagonal lattice, defined by the lattice vectors

$$\boldsymbol{a}_1 = a_{\rm TB}\begin{pmatrix}1\\0\end{pmatrix}\ ,\ \boldsymbol{a}_2 = \tfrac{1}{2}a_{\rm TB}\begin{pmatrix}1\\\sqrt{3}\end{pmatrix}\ , \tag{6.21}$$

and the three nearest neighbor displacement vectors

$$\begin{aligned}\boldsymbol{\delta}_1 &= a_{\rm TB}\begin{pmatrix}0\\1/\sqrt{3}\end{pmatrix}\ ,\ \boldsymbol{\delta}_2 = \tfrac{1}{2}a_{\rm TB}\begin{pmatrix}-1\\-1/\sqrt{3}\end{pmatrix},\\ \boldsymbol{\delta}_3 &= \tfrac{1}{2}a_{\rm TB}\begin{pmatrix}1\\-1/\sqrt{3}\end{pmatrix}\ .\end{aligned} \tag{6.22}$$

The vector $\boldsymbol{r}_{ij} = i\boldsymbol{a}_1 + j\boldsymbol{a}_2$, with i, j integer, denotes the center of unit cell (i, j). As shown in Fig. 6.7 we put the sites belonging to the A(B)-sublattice at $\boldsymbol{r}_{ij} - (+)\boldsymbol{\delta}_1/2$ to have inversion symmetry about the origin.

To ensure that the discretization (lattice constant $a_{\rm TB}$) is commensurate with the moiré superlattice (lattice constant λ), we take an integer ratio $\lambda/a_{\rm TB} = \Lambda$, so

$$a_{\rm TB} = \frac{\lambda}{\Lambda} = \frac{a}{\Lambda\sqrt{\delta^2+\theta^2}}. \tag{6.23}$$

The accuracy of the discretization is improved by increasing Λ. (In the simulations we take $\Lambda = 20$.)

The bare graphene Hamiltonian (6.13) is produced by nearest-neighbor hopping on the hexagonal lattice,

$$\tilde{H}_0 = -\sum_{i,j}\sum_{\alpha=1}^{3} t\left[a^\dagger(\boldsymbol{r}_{ij}^{\rm A})b(\boldsymbol{r}_{ij}^{\rm A}+\boldsymbol{\delta}_\alpha) + {\rm H.c.}\right] + \sum_{i,j}\tilde{V}(\boldsymbol{r}_{ij}). \tag{6.24}$$

Here $\boldsymbol{r}_{ij}^{\rm A}$ denotes the positions of sites on sublattice A, $a^\dagger$ and $b^\dagger$ are creation operators on the A and B sites, and t is the hopping amplitude,

$$t = \frac{2v}{\sqrt{3}a_{\rm TB}} = \frac{2v}{\sqrt{3}a}\Lambda\sqrt{\delta^2+\theta^2}\,. \tag{6.25}$$

The superlattice term U_1 in Eq. (6.14) corresponds to a periodic spatial modulation of the on-site energy, the same for A and B sites, while the term U_2 has an additional staggering — acting on A and B sites with opposite sign. To maintain the spatial inversion symmetry of the continuum model we evaluate both terms at the center of each unit cell. The resulting terms are given in Eqs. (6.29) and (6.30).

The superlattice term U_3 with the fictitious vector potential in Eq. (6.18) represents a periodic spatial modulation of the nearest-neighbor hopping amplitudes in the tight-binding Hamiltonian (6.24). The replacement $t \mapsto t + \delta t_\alpha(\boldsymbol{r}_{ij})$ produces in the continuum limit the vector potential [31]

$$\mathcal{A}(\boldsymbol{r}) = \sum_{\alpha=1}^{3} \delta t_\alpha(\boldsymbol{r}) e^{-i\boldsymbol{K}\boldsymbol{\delta}_\alpha} = \mathcal{A}_x(\boldsymbol{r}) + i\mathcal{A}_y(\boldsymbol{r})\,. \tag{6.26}$$

The vectors $\boldsymbol{K} = (4\pi/3a_{\mathrm{TB}})\hat{x}$ and $-\boldsymbol{K}$ locate the two Dirac cones (valleys) in the hexagonal Brillouin zone. We seek to discretize a given fictitious vector potential on the lattice, in other words we need to invert (6.26). The complex field $\mathcal{A}$ is constructed from three real hoppings, so we have some freedom in choosing the δt_α. We take

$$\begin{aligned} &\delta t_1 = 2\mathcal{A}_x/3\ ,\ \delta t_2 = \mathcal{A}_y/\sqrt{3} - \mathcal{A}_x/3, \\ &\delta t_3 = -\mathcal{A}_y/\sqrt{3} - \mathcal{A}_x/3\,. \end{aligned} \tag{6.27}$$

To avoid a spurious breaking of inversion symmetry we evaluate $\mathcal{A}$ in the middle of each bond, rather than on the lattice site.

Collecting results, we arrive at the tight-binding Hamiltonian

$$\begin{aligned} H = &\sum_{i,j} \left[(\epsilon_+^{i,j} + \epsilon_-^{i,j} + \tilde{V}(\boldsymbol{r}_{i,j})) a_{i,j}^\dagger a_{i,j} + (\epsilon_+^{i,j} - \epsilon_-^{i,j} + \tilde{V}(\boldsymbol{r}_{i,j})) b_{i,j}^\dagger b_{i,j} \right] \\ &- \sum_{i,j} \left[t_1^{i,j} a_{i,j}^\dagger b_{i,j} + t_2^{i,j} a_{i,j}^\dagger b_{i,j-1} + t_3^{i,j} a_{i,j}^\dagger b_{i+1,j-1} + \mathrm{H.c.} \right]. \end{aligned} \tag{6.28}$$

The energies

$$\epsilon_+^{i,j} = \frac{E_0}{\hbar v b} \frac{\delta}{\sqrt{\delta^2+\theta^2}} \frac{2\pi}{\Lambda} \left[\cos(\boldsymbol{g}_1 \boldsymbol{r}_{i,j}) + \cos(\boldsymbol{g}_3 \boldsymbol{r}_{i,j}) + \cos(\boldsymbol{g}_5 \boldsymbol{r}_{i,j}) \right]\ , \tag{6.29}$$

$$\epsilon_-^{i,j} = \frac{E_0}{\hbar v b} \frac{-\sqrt{3}\delta}{\sqrt{\delta^2+\theta^2}} \frac{2\pi}{\Lambda} \left[\sin(\boldsymbol{g}_1 \boldsymbol{r}_{i,j}) + \sin(\boldsymbol{g}_3 \boldsymbol{r}_{i,j}) + \sin(\boldsymbol{g}_5 \boldsymbol{r}_{i,j}) \right], \tag{6.30}$$

correspond to the periodic on-site contributions of the moiré super-lattice potential which are symmetric ($\epsilon_+^{i,j}$) and antisymmetrc ($\epsilon_-^{i,j}$) with respect to a swap of the A and B sublattice. The hoppings

$$\begin{aligned} t_1^{i,j} &= t - 2\mathcal{A}_x(r_{i,j})/3, && \text{(6.31a)} \\ t_2^{i,j} &= t - \mathcal{A}_y(r_{i,j} - \delta_1/2 + \delta_2/2)/\sqrt{3} \\ &\quad + \mathcal{A}_x(r_{i,j} - \delta_1/2 + \delta_2/2)/3, && \text{(6.31b)} \\ t_3^{i,j} &= t + \mathcal{A}_y(r_{i,j} - \delta_1/2 + \delta_3/2)/\sqrt{3} \\ &\quad + \mathcal{A}_x(r_{i,j} - \delta_1/2 + \delta_3/2)/3, && \text{(6.31c)} \end{aligned}$$

include both the isotropic contribution t of native graphene and the periodic modulation from the moiré superlattice, produced by the fictitious vector potential

$$\begin{aligned} \boldsymbol{\mathcal{A}}(\boldsymbol{r}) = \begin{pmatrix} \mathcal{A}_x(\boldsymbol{r}) \\ \mathcal{A}_y(\boldsymbol{r}) \end{pmatrix} &= \frac{E_0}{\hbar v b} \frac{-\delta^2}{\delta^2 + \theta^2} \frac{2\pi}{\Lambda} \\ &\times \begin{pmatrix} \cos(\boldsymbol{g}_1 \boldsymbol{r}) + \cos(\boldsymbol{g}_5 \boldsymbol{r}) - 2\cos(\boldsymbol{g}_3 \boldsymbol{r}) \\ \sqrt{3}[\cos(\boldsymbol{g}_1 \boldsymbol{r}) - \cos(\boldsymbol{g}_5 \boldsymbol{r})] \end{pmatrix} . \end{aligned} \tag{6.32}$$

Finally, the orbital effect of the magnetic field $\boldsymbol{B} = B\hat{z}$ is included by adding a Peierls phase $2\pi(\Phi/\Phi_0)\Lambda^{-2}\boldsymbol{r}_{i,j} \cdot \hat{x}$ to the hopping amplitude $t_1^{i,j}$, where Φ is the flux through the superlattice unit cell.

Chapter 7

Giant negative magnetoresistance driven by spin-orbit coupling at the $LaAlO_3/SrTiO_3$ interface

7.1 Introduction

The mobile electrons at the $LaAlO_3/SrTiO_3$ (LAO/STO) interface [116] display an exotic combination of superconductivity [132, 32] and magnetic order [22, 18, 95, 82]. The onset of superconductivity at sub-Kelvin temperatures appears in an interval of electron densities where the effect of Rashba spin-orbit coupling on the band structure at the Fermi level is strongest [153, 33], but whether this correlation implies causation remains unclear.

Transport experiments above the superconducting transition temperature have revealed a very large ("giant") drop in the sheet resistance of the LAO/STO interface upon application of a parallel magnetic field [15, 180, 80, 81]. An explanation has been proposed [81, 137] in terms of the Kondo effect: Variation of the electron density or magnetic field drives a quantum phase transition between a high-resistance correlated electronic phase with screened magnetic impurities and a low-resistance phase of polarized impurity moments. The relevance of spin-orbit coupling for magnetotransport is widely appreciated [15, 170, 57, 52, 137, 30, 26], but it was generally believed to be too weak an effect to provide a single-particle explanation of the giant magnetoresistance.

In this work we provide experimental data (combining magnetic field, gate voltage, and temperature profiles for the resistance of the LAO/STO interface) and theoretical calculations that support an explanation fully within the single-particle context of Boltzmann transport. The key ingredients are the combination of spin-orbit coupling, band anisotropy, and finite-range electrostatic impurity scattering. The thermal insensitivity of the giant magnetoresistance [15, 180], in combination with a striking correspondence that we have observed between the gate voltage and temperature dependence of the effect, are features that are difficult to reconcile with the thermally fragile Kondo interpretation — but fit naturally in the semiclassical Boltzmann description.

7.2 Experimental results

We first present the experimental data and then turn to the theoretical description. Devices were fabricated by using amorphous LAO (a-LAO) as a hard mask and epitaxially depositing a thin (12 u. c.) film of LAO on top of a $\mathrm{TiO_2}$-terminated (0 0 1)STO single crystal substrate. The film was grown by pulsed laser deposition at 770 °C in $\mathrm{O_2}$ at a pressure of 6×10^{-5} mbar. The laser fluence was $1\,\mathrm{J\,cm^{-2}}$ and the repetition rate was 1 Hz. The growth of the film was monitored *in-situ* using reflection high energy electron diffraction (RHEED), and layer-by-layer growth was confirmed. After deposition, the sample was annealed for 1 h at 600 °C in 300 mbar of $\mathrm{O_2}$. Finally, the sample was cooled down to room temperature in the same atmosphere. Magnetotransport measurements were performed in a four-probe Hall bar geometry and in a field-effect configuration (Fig. 7.1a, inset) established with a homogeneous metallic back gate. The magnetic field B is applied in-plane and perpendicular to the current. The longitudinal sheet resistance $\rho_{xx}(B)$ determines the dimensionless magnetoresistance

$$\mathrm{MR}(B) = \rho_{xx}(B)/\rho_{xx}(0) - 1. \tag{7.1}$$

The left panel of Fig. 7.1a shows the measured magnetoresistance as a function of magnetic field, recorded at 1.4 K, for gate voltages V_G ranging from 0 V to 50 V. In general, we observe the magnetoresistance to remain mainly flat up to some characteristic value of the magnetic field. For larger values, the magnetoresistance drops sharply. At even higher magnetic fields, the magnetoresistance begins to saturate, producing an overall bell-like curve. At the highest voltage $V_\mathrm{G} = 50\,\mathrm{V}$, a very large negative magnetoresistance is observed (a drop of 70%) over a magnetic field range from 0 T to 12 T. As V_G is decreased, the overall magnitude of the magnetoresistance drop is suppressed, as the curves flatten out and the characteristic field progressively moves to higher B. At $V_\mathrm{G} = 10\,\mathrm{V}$, the maximum magnetoresistance variation is less than 5%.

The right panel of Fig. 7.1a shows the measured magnetoresistance at a fixed gate voltage of $\mathrm{V_G} = 50\,\mathrm{V}$, for different temperatures ranging from 1.4 K to 20 K. The correspondence between the bell-shaped magnetoresistance profiles as a function of temperature and gate voltage is striking. As T increases or V_G decreases, both the magnitude of the magnetoresistance and steepness of $\partial\mathrm{MR}/\partial\mathrm{B}$ decrease. Although the negative magnetoresistance is progressively suppressed as the temperature is raised, it is still clearly visible at 20 K, in agreement with previous experiments [15, 180]. Notice that the characteristic field scale of the resistance drop increases with temperature.

7.3 Boltzmann equation of the three-band model

For the theoretical description we use a three-band model of the $t_{2\mathrm{g}}$ conduction electrons at the LAO/STO interface [80], with Hamiltonian

$$H = \sum_{\boldsymbol{k},l,l',\sigma,\sigma'} c^\dagger_{\boldsymbol{k},l,\sigma} \left(H_\mathrm{L} + H_\mathrm{SO} + H_\mathrm{Z} + H_\mathrm{B}\right) c_{\boldsymbol{k},l',\sigma'}. \tag{7.2}$$

The operators $c^\dagger_{\boldsymbol{k},l,\sigma}$ create electrons of spin σ and momentum $\boldsymbol{k}$ (measured in units of the lattice constant $a = 0.4\,\mathrm{nm}$), in orbitals $l = d_{xy}, d_{xz}, d_{yz}$ of the Ti atoms close to the interface. We describe the various terms in this three-band Hamiltonian, with parameter values from the literature [80, 102, 142, 192, 173, 29, 144, 123, 53, 141] that we will use in our calculations. (Further details are given in the Appendix.)

The lobes of the d_{xy} orbital are in plane, producing two equivalent hopping integrals $t_l = 340\,\mathrm{meV}$. For the two other orbitals, the x-lobe or y-lobe is in plane and the z-lobe is out of plane, giving rise to one large and one small hopping element t_l and $t_h = 12.5\,\mathrm{meV}$, respectively. The d_{xz} and d_{yz} orbitals are hybridized by a diagonal hopping $t_d = t_h$. Confinement lowers the d_{xy} orbital in energy by $\Delta_E = 60\,\mathrm{meV}$. All this

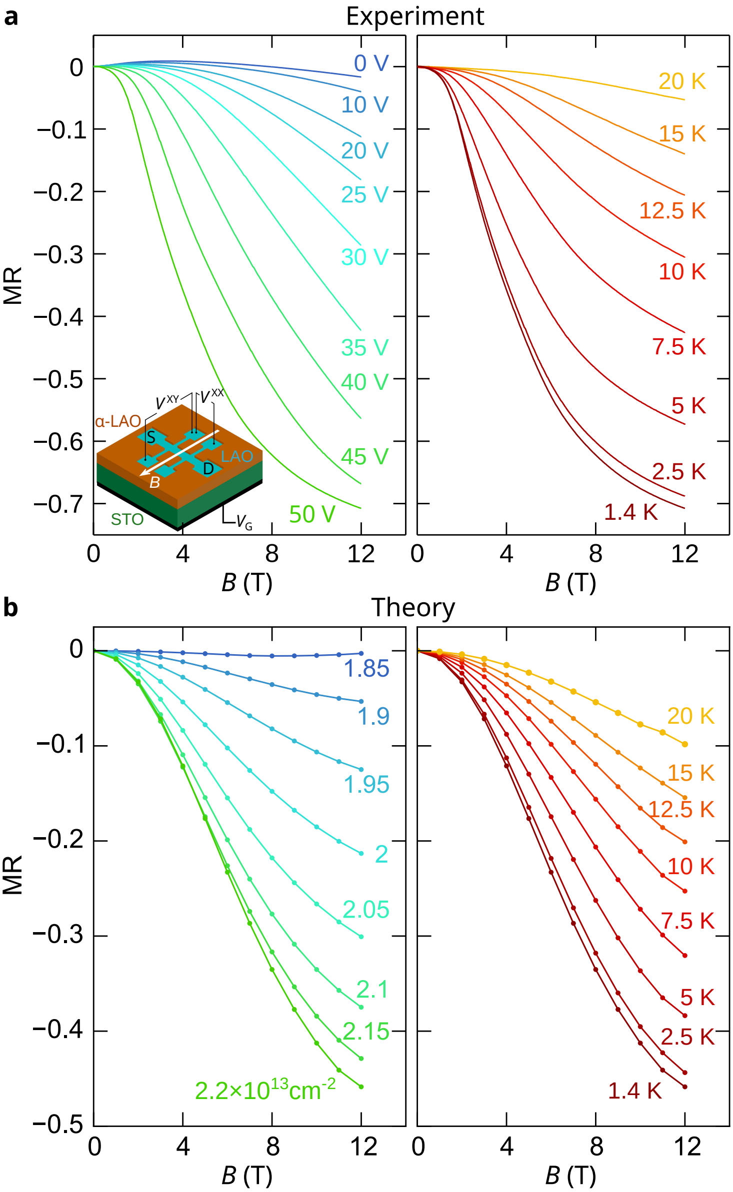

Figure 7.1. (a) Measured magnetoresistance at $T = 1.4\,\mathrm{K}$ for different gate voltages (left panel) and at $V_\mathrm{G} = 50\,\mathrm{V}$ for various temperatures (right panel). Inset: Schematic drawing of the device in a Hall bar geometry (in-plane field perpendicular to current direction), showing the source S, drain D, longitudinal voltage V^xx, transverse voltage V^xy and gate voltage V_G.
(b) Magnetoresistance calculated from the Boltzmann equation, at fixed $T = 1.4\,\mathrm{K}$ (left panel) and at fixed $n = 2.2 \times 10^{13}\,\mathrm{cm}^{-2}$ (right panel).

information is encoded in

$$H_{\mathrm{L}} = \begin{pmatrix} \epsilon_{xy}(k) - \Delta_{\mathrm{E}} & 0 & 0 \\ 0 & \epsilon_{xz}(k) & \delta(k) \\ 0 & \delta(k) & \epsilon_{yz}(k) \end{pmatrix} \otimes \hat{\sigma}_0, \tag{7.3}$$

$$\begin{aligned} \epsilon_{xy}(k) &= 2t_l(2 - \cos k_x - \cos k_y), \\ \epsilon_{xz}(k) &= 2t_l(1 - \cos k_x) + 2t_h(1 - \cos k_y), \\ \epsilon_{yz}(k) &= 2t_h(1 - \cos k_x) + 2t_l(1 - \cos k_y), \\ \delta(k) &= 2t_d \sin k_x \sin k_y. \end{aligned} \tag{7.4}$$

We use $\hat{\sigma}_{x,y,z}$ and $\hat{\sigma}_0$ to denote the Pauli-matrices and the identity acting on the electron spin.

The intrinsic electric field at the interface breaks inversion symmetry and produces the term

$$H_{\mathrm{Z}} = \Delta_{\mathrm{Z}} \begin{pmatrix} 0 & i \sin k_y & i \sin k_x \\ -i \sin k_y & 0 & 0 \\ -i \sin k_x & 0 & 0 \end{pmatrix} \otimes \hat{\sigma}_0, \tag{7.5}$$

with $\Delta_Z = 15\,\mathrm{meV}$. Atomic spin-orbit coupling gives

$$H_{\mathrm{SO}} = \frac{\Delta_{\mathrm{SO}}}{2} \begin{pmatrix} 0 & i\hat{\sigma}_x & -i\hat{\sigma}_y \\ -i\hat{\sigma}_x & 0 & i\hat{\sigma}_z \\ i\hat{\sigma}_y & -i\hat{\sigma}_z & 0 \end{pmatrix}, \tag{7.6}$$

with an amplitude $\Delta_{\mathrm{SO}} = 5\,\mathrm{meV}$. Together, H_{Z} and H_{SO} cause a Rashba-type splitting of the bands, coupling the d_{xy} orbital with the $d_{xz/yz}$ orbitals above the Lifshitz point at the bottom of the $d_{xz/yz}$ bands.

The term $H_{\mathrm{B}} = \mu_{\mathrm{B}}(\boldsymbol{L} + g\boldsymbol{S}) \cdot \boldsymbol{B}/\hbar$, with $g = 5$ [53], describes the coupling of the applied magnetic field to the spin and orbital angular momentum of the electrons, where $\boldsymbol{S} = \hbar\hat{\boldsymbol{\sigma}}/2$ and

$$L_x = \hbar\begin{pmatrix} 0 & i & 0 \\ -i & 0 & 0 \\ 0 & 0 & 0 \end{pmatrix},\ L_y = \hbar\begin{pmatrix} 0 & 0 & -i \\ 0 & 0 & 0 \\ i & 0 & 0 \end{pmatrix},\ L_z = \hbar\begin{pmatrix} 0 & 0 & 0 \\ 0 & 0 & i \\ 0 & -i & 0 \end{pmatrix}. \tag{7.7}$$

The resulting highly anisotropic band structure is shown in Fig. 7.2. Notice the unusually close relevant energy scales: When measured from the bottom of the upper, anisotropic bands, the Fermi energy, spin-orbit coupling induced spin-splitting, Zeeman energy (10 T) and temperature (10 K) all are on the order of 1 meV.

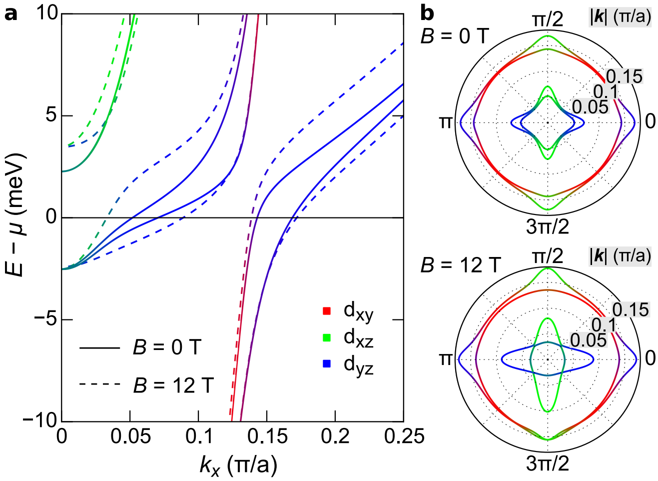

Figure 7.2. (a) Dispersion relation for the mobile electrons at the $\mathrm{LaAlO_3/SrTiO_3}$ interface, calculated from the model Hamiltonian (7.2) for $n = 2.2 \times 10^{13}\,\mathrm{cm}^{-2}$ at $B = 0\,\mathrm{T}$ (solid line) and $B = 12\,\mathrm{T}$ (dashed line). Colors indicate the orbital character of the bands. (b) Corresponding Fermi surfaces when the chemical potential is located at the "sweet spot" above the Lifshitz point where the system becomes very sensitve to changes in carrier density and magnetic field.

We calculate the magnetoresistance from the model Hamiltonian (7.2) using the semiclassical Boltzmann transport equation for the momentum $\boldsymbol{k}$ and band index ν-dependent distribution function $f_{\boldsymbol{k},\nu} = f_0(\epsilon_{\boldsymbol{k},\nu}) + g_{\boldsymbol{k},\nu}$. We linearize around the equilibrium Fermi-Dirac distribution f_0, at temperature T and chemical potential μ (determined self-consistently to obtain a prescribed carrier density n). In this way we find the conductivity tensor

$$\sigma_{ij} = e \sum_{\boldsymbol{k},\nu} (\boldsymbol{v}_{\boldsymbol{k},\nu})_i \partial g_{\boldsymbol{k},\nu} / \partial E_j \tag{7.8}$$

in linear response to the electric field $\boldsymbol{E}$. The longitudinal resistivity ρ_{xx} then follows upon inversion of the $\boldsymbol{\sigma}$-tensor. The band structure determines the velocity $\boldsymbol{v}_{\boldsymbol{k},\nu} = \hbar^{-1} \nabla_{\boldsymbol{k}} \epsilon_{\boldsymbol{k},\nu}$, which is not parallel to the momentum $\hbar\boldsymbol{k}$ because of the anisotropic Fermi surface.

Calculations of this type are routinely simplified using Ziman's relaxation-time approximation [193, 194], but the combination of finite-range scattering and anisotropic band structure renders this approximation unreliable [122]. We have therefore resorted to a numerical solution of the full partial differential equation:

$$
\begin{aligned}
-\, e(\boldsymbol{v}_{\boldsymbol{k},\nu} \cdot \boldsymbol{E})\partial f_0/\partial\epsilon_{\boldsymbol{k},\nu} &= (e/\hbar)(\boldsymbol{v}_{\boldsymbol{k},\nu} \times \boldsymbol{B}) \cdot \nabla_{\boldsymbol{k}} g_{\boldsymbol{k},\nu} \\
&+ \sum_{\boldsymbol{k}',\nu'} (g_{\boldsymbol{k},\nu} - g_{\boldsymbol{k}',\nu'}) q_{\boldsymbol{k}\nu,\boldsymbol{k}'\nu'} \delta(\epsilon_{\boldsymbol{k},\nu} - \epsilon_{\boldsymbol{k}',\nu'}). \qquad (7.9)
\end{aligned}
$$

Elastic impurity scattering enters with a rate

$$
q_{\boldsymbol{k}\nu,\boldsymbol{k}'\nu'} = \tfrac{2}{3}\pi\hbar^{-1}\delta^2\xi^4 n_{\mathrm{imp}}\, e^{-\xi^2|\boldsymbol{k}-\boldsymbol{k}'|^2/2} |\langle u_{\boldsymbol{k}\nu}|u_{\boldsymbol{k}'\nu'}\rangle|^2. \qquad (7.10)
$$

The impurity density n_{imp} and scattering amplitude δ drop out of the magnetoresistance (7.1), so they need not be specified. The scattering potential has correlation length ξ, for which we take $2\,\mathrm{nm} \simeq 5$ lattice constants, consistent with experiments on scattering by dislocations [168]. (We will discuss the role of this finite correlation length later on.) Both intraband and interband scattering are included via the structure factor $|\langle u_{\boldsymbol{k}\nu}|u_{\boldsymbol{k}'\nu'}\rangle|^2$, which takes into account the finite overlap $\langle\psi_\nu(\boldsymbol{k})|V(\boldsymbol{r})|\psi_{\nu'}(\boldsymbol{k}')\rangle$ of the Bloch states $\psi_\nu(\boldsymbol{k}) = u_{\boldsymbol{k}\nu}(\boldsymbol{r})e^{i\boldsymbol{k}\cdot\boldsymbol{r}}$ and $\psi_{\nu'}(\boldsymbol{k}') = u_{\boldsymbol{k}'\nu'}(\boldsymbol{r})e^{i\boldsymbol{k}'\cdot\boldsymbol{r}}$. [1]

7.4 Discussion of the numerical results and comparison with the experimental data

The in-plane magnetoresistance resulting from the Boltzmann equation is shown in Fig. 7.1b. The similarity in the bell-shaped magnetoresistance curves, with a corresponding dependence on carrier density and temperature, is clear and remarkable in view of the simplicity of the theoretical model. We conclude that a semiclassical single-particle description can produce a “giant” magnetoresistance, up to 50% for a quite conservative choice of parameter values.

Two main ingredients explain how such a large negative magnetoresistance could follow from a model without electron-electron interactions. The *first ingredient* is the orbital-mixing character of the atomic and inversion-symmetry-breaking spin-orbit coupling terms H_{SO} and H_{Z}. As a result, the spin-orbit splitting is very nonlinear and produces a “sweet spot”, that is, a narrow range of Fermi energies (carrier densities $n^* \simeq$

---

[1] In the presence of strong spin-orbit interactions there can be additional corrections to Eqs. (7.8) and (7.9) [156, 112]. We do not consider these here since we have found that they vanish for in-plane fields, see the Appendix.

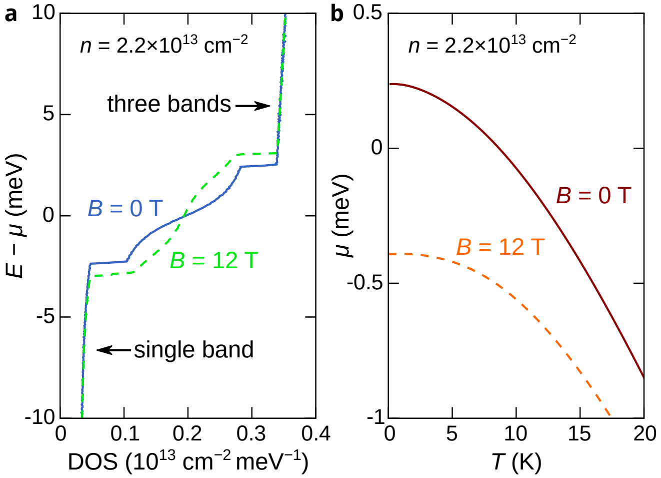

Figure 7.3. Energy-dependent density of states (a) and temperature-dependent chemical potential (b), calculated from the three band Hamiltonian (7.2). Both quantities are shown for the "sweet-spot" carrier density $n = 2.2 \times 10^{13}\,\mathrm{cm}^{-2}$, at $B = 0\,\mathrm{T}$ (solid line) and $B = 12\,\mathrm{T}$ (dashed line).

$2.2 \times 10^{13}/\mathrm{cm}^2$) in which the system becomes sensitive to small changes in the density. If the density (or the corresponding gate voltage) is near the sweet spot, the spin-orbit induced band mixing gives rise to a substantial contribution to the (zero-field) resistance stemming from inter-band scattering. The Zeeman energy in turn favors an alignment of the spin with the magnetic field and drives a highly anisotropic deformation of the Fermi surface into spin-polarized bands (see Fig. 7.2). Inter-band scattering is suppressed which explains the decrease in sheet-resistance. At densities $n < n^*$ only a single band is occupied and spin-orbit coupling is well described by a conventional Rashba term $\alpha_{\mathrm{SO}}(\hat{\boldsymbol{\sigma}} \times \boldsymbol{p})$ [33, 192, 56] and our calculation gives a vanishingly small magnetoresistance. At densities $n > n^*$ the calculated magnetoresistance starts to saturate and eventually becomes small again.

The *second ingredient* is the finite correlation length ξ of the disorder potential. The resulting anisotropic scattering rate (7.10) is largest at small momenta $|\boldsymbol{k} - \boldsymbol{k}'|$. Moderate values of ξ on the order of a few lattice constants suppress back-scattering processes within the outer Fermi surface with large average momentum k_{F}, while still allowing for inter-band scattering. This is accompanied by a quasi-particle lifetime which can be significantly smaller for the inner band (smaller average k_F). The imbalance of band mobilities promotes the importance of inter-band scattering when transport is dominated by quasi-particles in the outer bands which have a larger Fermi velocity and a small intra-band back-scattering rate. In comparison, we have found[2] that the isotropic scattering by a delta-function impurity potential cannot produce a magnetoresistance exceeding 15%.

Our theoretical curves show a smooth dependence on temperature, with the negative magnetoresistance persisting beyond 20 K, and they show a striking correspondence between the temperature dependence of the magnetoresistance for a fixed density and the density dependence for a fixed temperature. This correspondence, a hallmark of our experimental data, can be understood as a consequence of the renormalization of the chemical potential as a function of temperature, see Fig. 7.3. The weak temperature dependence of the Hall resistance point towards a constant carrier density in the range 1–20 K [167]. As shown in Fig 7.3a the density of states increases steeply with band energy in the vicinity of the sweet spot, much more than in conventional semiconductors. To keep the total carrier density fixed with increasing temperature, the chemical potential is lowered by more than 1 meV at 20 K compared to its low temperature limit. This is why increasing the temperature is equivalent to probing the band structure at a lower energy, explaining the similarity in the magnetoresistance curves in the left and right panels of Fig. 7.1.

These are the two key arguments in favor of a single-particle spin-orbit-coupling based mechanism for the giant negative magnetoresistance: Firstly, the persistence of the effect to elevated temperatures, and secondly the corresponding effect of temperature-increase and density-decrease. It seems difficult to incorporate these features of the data in the correlated-electron mechanism [81, 137], based on Kondo-screening of magnetic moments. There is a third noteworthy feature of the data that is not well reproduced by our calculation, and has been interpreted as evidence for a transition into a low-field Kondo phase [81, 137]: A rescaling of the magnetic field $B \to B/B^\star$ by a density-dependent value $B^\star$ collapses the measured magnetoresistance at different densities onto a single curve, see Fig. 7.4a. If we apply this $B/B^\star$ scaling to our numerical results a significant n-dependence remains, see Fig. 7.4b. The experimental scaling law points to some relevant physics that is not yet included in our minimal

---

[2] For further details see the Appendix.

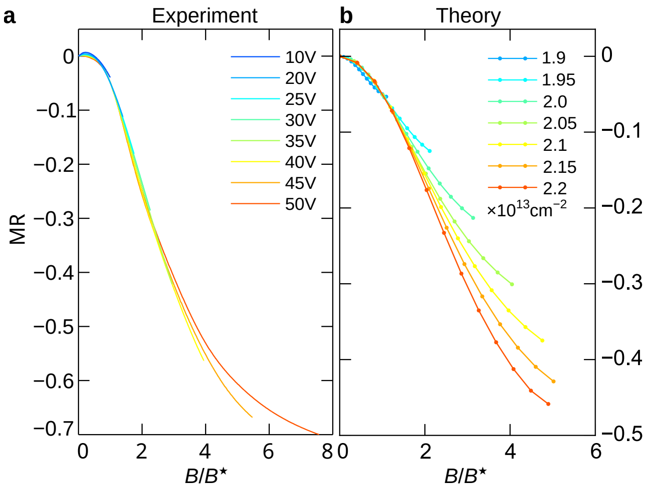

Figure 7.4. Measured (a) and calculated (b) magnetoresistance at 1.4 K for different densities or gate voltages as a function of the rescaled magnetic field $B/B^{\star}$. The characteristic field $B^{\star}$ is chosen such that the rescaled curves all pass through the point with MR $= -0.05$.

model.

7.5 Conclusion

In conclusion, we have presented experimental data and theoretical calculations that support a semiclassical single-particle mechanism for the giant magnetoresistance of the LAO/STO interface. The Boltzman transport equation with spin-orbit coupling, in combination with anisotropy of Fermi surface and scattering rates, suffices to produce a large resistance drop upon application of a magnetic field. The characteristic temperature and carrier-density dependence agree quite well with what is observed experimentally, but the $B/B^{\star}$ scaling will likely require an extension of the simplest three-band model.

Our explanation of the sudden onset of the magnetoresistance when the carrier density approaches a “sweet spot” of amplified spin-orbit coupling has addressed the normal-state transport above the superconducting transition temperature. Since superconductivity happens in the vicinity of the same “sweet spot”, it would be interesting to investigate whether spin-orbit coupling plays a dominant role in that transition as well.

7.6 Appendix

7.6.1 Complete set of experimental data

For completeness, Fig. 7.5 shows the systematic study of magnetoresistance in the $B - T$ space of parameters for gate voltages ranging from 50 V to 0 V. At high gate voltage and low temperature, a very large negative magnetoresistance is observed (up to 70% over a magnetic field range of 12 T). As gate voltage (temperature) is decreased (increased), the overall magnitude of the magnetoresistance drop is suppressed, as the curves flatten out.

7.6.2 Details on the choice of the model parameters

Values for the three-band model parameters found in the theoretical literature vary over a wide range, see for example Refs. [80, 192, 173]. ARPES measurements on the surface of STO [142, 123] and LAO/STO [29] have extracted values for the light and heavy effective masses as well as the confinement splitting Δ_{E}. The values are similar in all of the experiments. We take t_l, t_h according to the effective masses for the d_{xy} and d_{xz}/d_{yz} band in Ref. [123] and Δ_E according to the value found in Ref. [142]. An exact determination of the spin-orbit energies Δ_{SO} and Δ_{Z} is not yet available experimentally. There are, however, clear indications that the spin-orbit energy scale may be above 10 meV [153, 33]. We take moderate values consistent with the theoretical literature [102, 192]. We note that our simulations suggest that experiments are in the regime $\Delta_{\mathrm{Z}} > \Delta_{\mathrm{SO}}$. The calculated magnetoresistance is negative in this regime, while we have found both negative and positive magnetoresistance, depending on the density, for $\Delta_{\mathrm{SO}} > \Delta_{\mathrm{Z}}$.

7.6.3 Estimate of the "sweet-spot" carrier density and the magnetic field sensitive density window.

A central quantity of our proposed model is the "sweet-spot" carrier density n^*. This density corresponds to a position of the Fermi level $E_{\mathrm{F}} = \mu(T = 0) \approx 0$ where band structure is most sensitive to the competition between spin-orbit coupling and magnetic field. Even for the

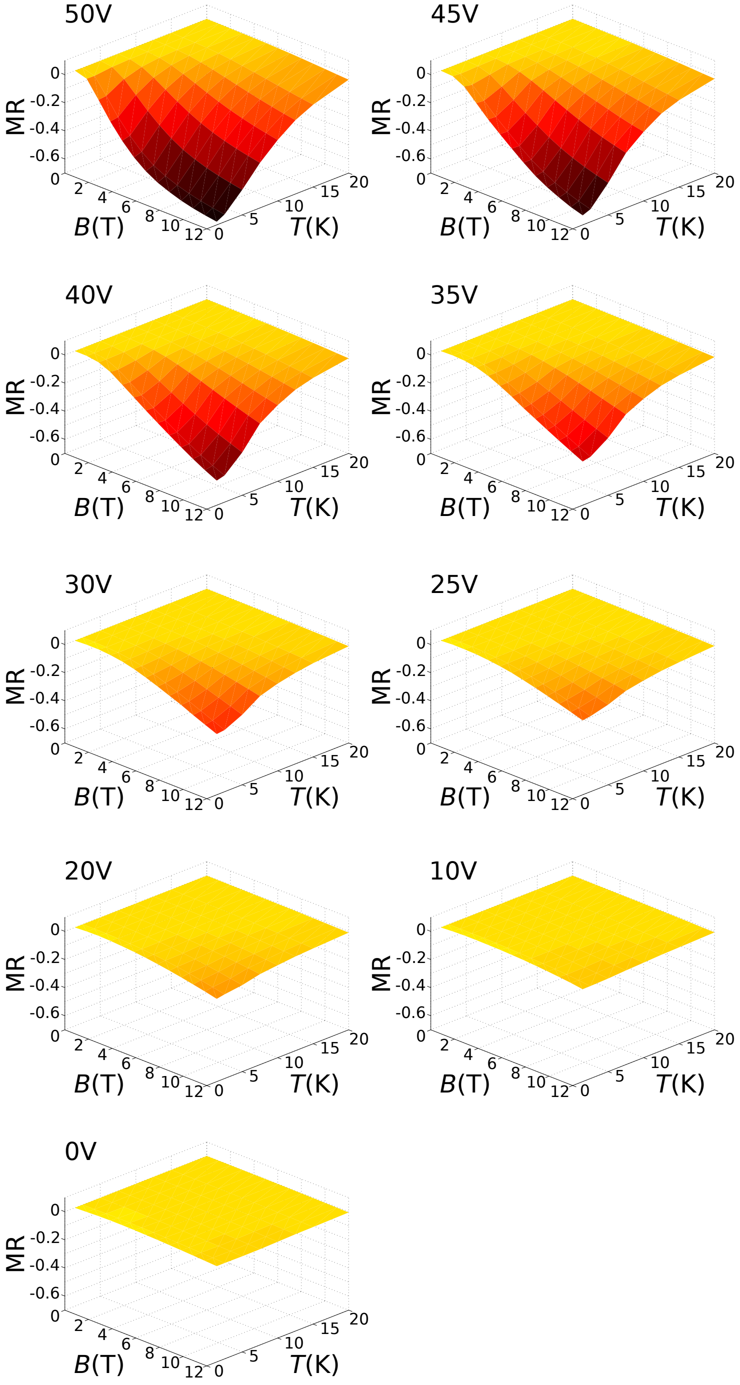

Figure 7.5. Measured magnetoresistance in the $B - T$ space of parameters for gate voltages ranging from 50 V to 0 V.

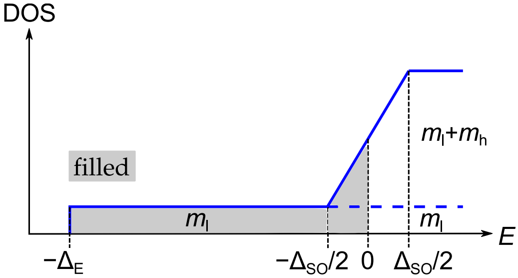

Figure 7.6. Approximate density of states and filling for the "sweet-spot" carrier density at $T = 0$. $m_l = \hbar^2/(2t_l a^2)$ and $m_h = \hbar^2/(2t_h a^2)$ refer to the effective light and heavy electron masses corresponding to a 2d density of states $m_i/\pi\hbar^2 = 1/2\pi t_i a^2$ for $i = l, h$.

mimimal three-band model of Hamiltonian (7.2) the exact value of n^* has a complicated dependence on the model paramters t_l, t_h, t_d, Δ_E, Δ_SO and Δ_Z that can be obtained from integrating the density of states shown in Fig. 7.3. In order to give simple estimate we can approximate the density of states as shown Fig. 7.6. The corresponding estimate for the sweet-spot density is given by

$$n^* a^2 \approx \frac{\Delta_\mathrm{E}}{2\pi t_l} + \frac{\Delta_\mathrm{SO}}{16\pi}\left(\frac{1}{t_l} + \frac{1}{t_h}\right). \tag{7.11}$$

For our choice of parameters $t_l = 340\,\mathrm{meV}$, $t_h = 12.5\,\mathrm{meV}$, $\Delta_\mathrm{E} = 60\,\mathrm{meV}$ and $\Delta_\mathrm{SO} = 5\,\mathrm{meV}$ we obtain $n^* a^2 \approx 0.036$. Numerical integeration of the density of states yields $n^* a^2 = 0.035$.

Due to the fixed in-plane configuration of the applied magnetic field, the carrier densities corresponding to each measured gate voltage in Fig. 7.2a) could not be determined for this sample. (Switching from an in-plane to an out-of-plane Hall configuration required a thermal cycling of the device rendering to obtained Hall densities unreliable.) However, in previous samples with similar geometry and grown under the same conditions, the carrier density modulation resulting from field effect between 0 V and 50 V is about $0.5 \times 10^{13}\,\mathrm{cm}^{-2}$ [32], in good agreement with the carrier density values in our model calculation. The density window for which our minimal model shows a large magnetoresistance is essentially limited to a chemical potential window $\Delta\mu \sim \Delta_\mathrm{SO}$ around the "sweet-spot" density. Both inelastic scattering processes and the presence of additional

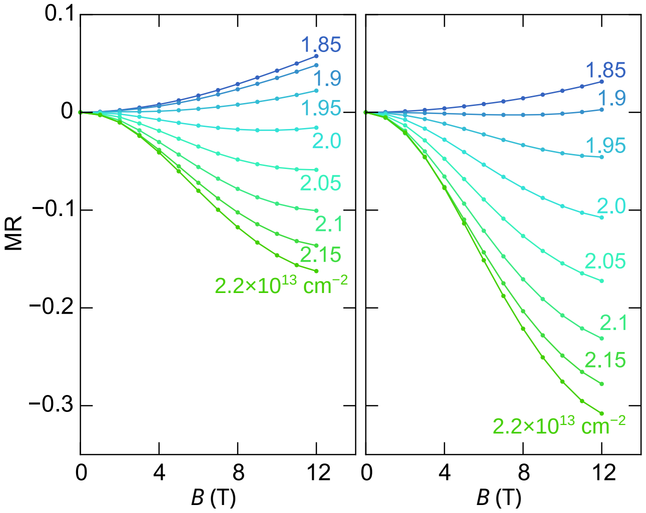

Figure 7.7. Theoretical magnetoresistance for the same model parameters as in Fig. 7.1b, but using point-like uncorrelated disorder $q_{\boldsymbol{k}\nu,\boldsymbol{k}'\nu'} = \text{const.}|\langle u_{\boldsymbol{k}\nu}|u_{\boldsymbol{k}'\nu'}\rangle|^2$ (or $\xi = 0$) (left panel) and same parameters as in Fig. 7.1b but using $q_{\boldsymbol{k}\nu,\boldsymbol{k}'\nu'} \propto |\langle u_{\boldsymbol{k}\nu}|u_{\boldsymbol{k}'\nu'}\rangle|^2(|\boldsymbol{k}-\boldsymbol{k}'|^2 + 1/l^2)^{-1}$ for $l = 5$ lattice constants (right panel).

subbands may extend this energy window, if we go beyond our minimal model.

7.6.4 Theoretical magnetoresistance for point-like and non-Gaussian scatterers

In the main text we discussed how the amplitude of the calculated magnetoresistance drop is larger for disorder with a finite correlation length $\xi > 0$. For comparison, we show in the left panel of Fig. 7.7 the magnetoresistance for the same parameters as in the main text, but point-like, uncorrelated scatterers. Notice that the maximum drop in this case is only about 15%, more than a factor of 3 smaller. Moreover the magnetoresistance is actually positive for a range of densities above the Lifshitz-point ($n_\mathrm{L} = 1.83 \times 10^{13}/\mathrm{cm}^2$), but below the sweet-spot density $n^* = 2.2 \times 10^{13}/\mathrm{cm}^2$.

While it is important that the scattering amplitude has a finite correlation length, it need not necessarily be a Gaussian correlation. For comparison in the right panel of Fig. 7.7 we show results for a scattering

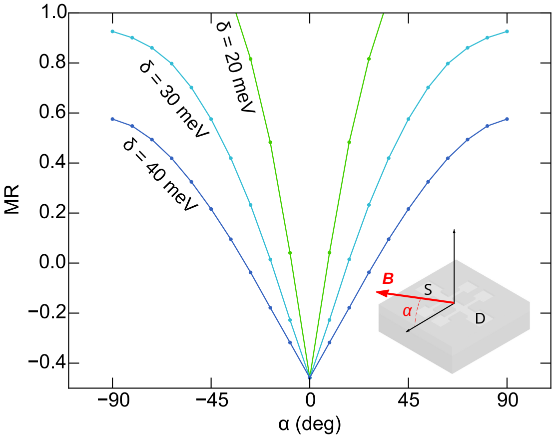

Figure 7.8. Calculated magnetoresistance as a function of the angle α (see inset) between the magnetic field $\boldsymbol{B}$ and the plane of the 2DES. Shown is the dependence for a fixed amplitude $|\boldsymbol{B}| = 12\,\mathrm{T}$ at 1.4 K for the "sweet-spot" carrier density $n = 2.2 \times 10^{13}\,\mathrm{cm}^{-2}$ using the same band parameters as in Fig. 7.2b. In the case of an out-of-plane field the magnetoresistance explicitly depends on the overall scattering amplitude $\delta^2 n_{\mathrm{imp}}$. Here we show three examples for the same impurity density $n_{\mathrm{imp}} = 1/(5\xi) = 1/(25a^2)$. The disorder amplitude δ is chosen such that the calculated zero-field resistance is comparable with our experimental values at high gate voltages, $\rho_0 = 70\,\Omega$, $160\,\Omega$, $275\,\Omega$ for $\delta = 20\,\mathrm{meV}$, $30\,\mathrm{meV}$, $40\,\mathrm{meV}$, respectively.

amplitude proportional to $(|\boldsymbol{k} - \boldsymbol{k}'|^2 + 1/l^2)^{-1}$, like it might be produced by screened Coulomb potentials of charged impurities close to the interface. Contrary to the Gaussian case there is now a significant amount of scattering at large momenta including backscattering. Still we find that for a screening length l of 5 lattice constants the magnetoresistance is already enhanced by a factor of 2 compared to point-like scatterers and the positive magnetoresistance at lower densities is suppressed.

7.6.5 Theoretical magnetoresistance as a function of the alignment between the magnetic field and the plane of the 2DES

Previous experiments (see for example Ref. [15]) have shown that the giant magnetoresistance has a strong out of plane anisotropy. Upon application of an out of plane component to the magnetic-field the negative magnetoresistance quickly decays and turns positive. For a comparison of our model with this characteristic experimental feature we show the calculated magnetoresistance as a function of the angle α between the magnetic field $|\boldsymbol{B}|$ and the plane of the 2DES for the "sweet-spot" carrier density n^* and the same parameters as Fig. 7.2b), left panel, see Fig. 7.8. Our minimal reproduces the general shape of the observed out of plane anisotropy. There is a sharp dip for perfect in-plane alignment. Upon application of an out-of-plane component the negative magnetoresistance signal becomes positive. This anisotropy is a consequence of the planar anisotropy of the spin-orbit coupling in the 3-band Hamiltonian, as well as the absence of orbital effects ($\boldsymbol{B} \times \nabla_{\boldsymbol{k}}$) for the in-plane fields. The resulting magnetoresistance dip explicitly depends on the overall scattering amplitude $\delta^2 n_{\text{imp}}$. Fig. 7.8 shows three examples. The dip is sharpest for small values of the disorder amplitude δ. We note that the longitudinal resistance obtained from the Boltzmann equation at a 12 T perpendicular field is likely to be an overestimate, because at large perpendicular fields additional "skipping"-orbit channels appear from that are missing in the Boltzmann approach. These would cause an increase of the Hall conductivity σ_{xy} and a decrease in the longitudinal resistance.

7.6.6 Spin-orbit corrections to the Boltzmann transport

When the wave functions of the conducting electrons have a non-trivial orbital and spin character, like in multiband spin-orbit coupled materials, new intrinsic and extrinsic mechanisms that are absent in simpler systems show up in determining the transport properties of complex materials. Three different mechanisms that are well known studied in the framework of the anomalous Hall effect can be discussed and systematically included in the Boltzmann transport description [112].

The first correction to Eqs. (7.8) and (7.9) is not dependent on the scattering process, because it follows from an intrinsic property of the band structure. The non-trivial Berry curvature $F_{\boldsymbol{k},\nu}$ of the bands in presence of spin-orbit coupling acts as a magnetic field in the momentum space and couples to the electric field to give an additional velocity $-\boldsymbol{F}_{\boldsymbol{k},\nu} \times e\mathbf{E}$ to the quasi-particle in the state $(\boldsymbol{k}, \nu)$. As said before the topological correction does not depend on the details of the scattering. So it can be dominant or subdominant (with respect to the mechanisms we discuss below) depending on the strength of the disorder and the density of impurities. However, its contribution to the (transversal) conductivity always remains of the order of the conductance quantum. We find that both measured and calculated longitudinal conductivities are much larger than e^2/h. In comparison with the longitudinal magnetoresistance which is of the order of the total resistance it can thus only give rise to small corrections. We do not consider these here.

The two mechanisms that we discuss below instead explicitly depend on the scattering processes. The first correction originates from asymmetric (*skew*) scattering of polarized electrons accelerated by an electric field. As we do in the main text impurity scattering is commonly treated in the lowest Born approximation, where the transition rate is given by the Fermi golden rule $q_{\boldsymbol{k}'\nu',\boldsymbol{k}\nu} = 2\pi|\langle \boldsymbol{k'}\nu'|V|\boldsymbol{k}\nu\rangle|^2/\hbar$. One of the limitations of this approximation is that it does not take into account the skew scattering, because $|V_{\boldsymbol{k}'\nu',\boldsymbol{k}\nu}|^2$ is clearly symmetric upon exchange of the initial and final states. In order to include antisymmetric corrections, the rate must be computed including higher orders in the perturbative expansion of the full scattering T-matrix. The first skew term is proportional to V^3. At this order, the semiclassical equation is still fully consistent compared to a rigorous quantum mechanical calculation. In the weak disorder limit (to linear order in the impurity density n_{imp}) the antisymmetric component of the transition probability is

$$\begin{aligned} q^{sk}_{\boldsymbol{k}'\nu',\boldsymbol{k}\nu} = \quad & -\frac{(2\pi)^2}{\hbar}\sum_{\boldsymbol{q},\nu''} \quad \Bigg[\Im\Big(\langle V_{\boldsymbol{k}'\nu',\boldsymbol{k}\nu}V_{\boldsymbol{k}\nu,\boldsymbol{q}\nu''}V_{\boldsymbol{q}\nu'',\boldsymbol{k}'\nu'}\rangle_{dis}\Big) \\ & \cdot\delta(\epsilon_{\boldsymbol{k},\nu}-\epsilon_{\boldsymbol{q},\nu''})\Bigg], \end{aligned} \tag{7.12}$$

where

$$\begin{aligned} V_{\boldsymbol{k}'\nu',\boldsymbol{k}\nu}V_{\boldsymbol{k}\nu,\boldsymbol{q}\nu''}V_{\boldsymbol{q}\nu'',\boldsymbol{k}'\nu'} \propto \\ \langle u_{\boldsymbol{k}'\nu'}|u_{\boldsymbol{k}\nu}\rangle\langle u_{\boldsymbol{k}\nu}|u_{\boldsymbol{q}\nu''}\rangle\langle u_{\boldsymbol{q}\nu''}|u_{\boldsymbol{k}'\nu'}\rangle \end{aligned} \tag{7.13}$$

where the disorder average has been introduced. Notice that naturally q^{sk} violates the detailed-balance condition, but still an important sum-rule is satisfied.

$$q^{sk}_{\boldsymbol{k}'\nu',\boldsymbol{k}\nu} = -q^{sk}_{\boldsymbol{k}\nu,\boldsymbol{k}'\nu'}, \tag{7.14}$$

$$\textstyle\sum_{\boldsymbol{k}',\nu'} q^{sk}_{\boldsymbol{k}'\nu',\boldsymbol{k}\nu} = \sum_{\boldsymbol{k}',\nu} q^{sk}_{\boldsymbol{k}\nu,\boldsymbol{k}'\nu'} = 0. \tag{7.15}$$

We do not consider further contributions on the order n_{imp}^2, here.

In addition to skew-scattering, the electronic wave packet accelerated by an electric field is subjected to the shift $\delta \boldsymbol{r}_{\boldsymbol{k}',\boldsymbol{k}}$ (*side-jump*) of its center of mass during a scattering event. The gauge-invariant expression for the coordinate shift can be expressed in terms of the Pancharatnam-Berry phase $\Phi_{\boldsymbol{q}\nu'',\boldsymbol{k}\nu,\boldsymbol{k}'\nu'}$ [156],

$$\begin{aligned}\delta \boldsymbol{r}_{\boldsymbol{k}'\nu',\boldsymbol{k}\nu} = &-\Big(\frac{\partial}{\partial \boldsymbol{k}''}\Phi_{\boldsymbol{q}\nu'',\boldsymbol{k}\nu,\boldsymbol{k}'\nu'}\Big)_{\boldsymbol{k}''\to\boldsymbol{k}} \\ &-\Big(\frac{\partial}{\partial \boldsymbol{k}''}\Phi_{\boldsymbol{q}\nu'',\boldsymbol{k}\nu,\boldsymbol{k}'\nu'}\Big)_{\boldsymbol{k}''\to\boldsymbol{k}'}, \end{aligned} \tag{7.16}$$

$$\Phi_{\boldsymbol{q}\nu'',\boldsymbol{k}\nu,\boldsymbol{k}'\nu'} = \arg\left(\langle u_{\boldsymbol{q}\nu''}|u_{\boldsymbol{k}\nu}\rangle\langle u_{\boldsymbol{k}\nu}|u_{\boldsymbol{k}'\nu'}\rangle\langle u_{\boldsymbol{k}'\nu'}|u_{\boldsymbol{q}\nu''}\rangle\right). \tag{7.17}$$

The presence of the side-jump has two effects on the transport. First, the accumulation of coordinate shifts after many scattering events gives (in the lowest Born approximation) a correction to the velocity $\boldsymbol{v}^{sj}_{\boldsymbol{k}\nu} = \sum_{\boldsymbol{k}',\nu'} q_{\boldsymbol{k}'\nu',\boldsymbol{k}\nu}\delta \boldsymbol{r}_{\boldsymbol{k}'\nu',\boldsymbol{k}\nu}$. Second, a particle scattered by an impurity under side-jump acquires a kinetic energy $\Delta\epsilon_{\boldsymbol{k}'\nu',\boldsymbol{k}\nu} = e\boldsymbol{E}\cdot\delta \boldsymbol{r}_{\boldsymbol{k}'\nu',\boldsymbol{k}\nu}$ in order to compensate the change in the potential energy induced by the electric field. As a consequence, the equilibrium distribution f_0 experiences an additional shift:

$$f_0(\epsilon_{\boldsymbol{k},\nu}) - f_0(\epsilon_{\boldsymbol{k}',\nu'}) = -(\partial f_0/\partial\epsilon_{\boldsymbol{k},\nu})\Delta\epsilon_{\boldsymbol{k}'\nu',\boldsymbol{k}\nu}\,. \tag{7.18}$$

Including all the terms, the conductivity tensor is given by

$$\sigma_{ij} = e\sum_{\boldsymbol{k},\nu}(\frac{1}{\hbar}\frac{\partial\epsilon_{\boldsymbol{k},\nu}}{\partial\boldsymbol{k}} + v^{sj}_{\boldsymbol{k},\nu})_i\partial g_{\boldsymbol{k},\nu}/\partial E_j - \varepsilon_{ij}eF^z_{\boldsymbol{k},\nu}f_0(\epsilon_{\boldsymbol{k},\nu}), \tag{7.19}$$

where ε_{ij} is the two-dimensional antisymmetric tensor and $g_{\boldsymbol{k},\nu}$ solves the modified Boltzmann equation [112]

$$\begin{aligned}&-e\Big(\frac{1}{\hbar}\frac{\partial\epsilon_{\boldsymbol{k},\nu}}{\partial\boldsymbol{k}}\cdot\boldsymbol{E}\Big)\frac{\partial f_0}{\partial\epsilon_{\boldsymbol{k},\nu}} = \\ &\sum_{\boldsymbol{k}',\nu'}\Big(q_{\boldsymbol{k}'\nu',\boldsymbol{k}\nu} + q^{sk}_{\boldsymbol{k}'\nu',\boldsymbol{k}\nu}\Big)\Big(g_{\boldsymbol{k},\nu} - g_{\boldsymbol{k}',\nu'} - \frac{\partial f_0}{\partial\epsilon_{\boldsymbol{k},\nu}}\Delta\epsilon_{\boldsymbol{k}'\nu',\boldsymbol{k}\nu}\Big)\delta(\epsilon_{\boldsymbol{k},\nu} - \epsilon_{\boldsymbol{k}',\nu'}).\end{aligned} \tag{7.20}$$

Discarding the intrinsic Berry-curvature correction, we numerically solve equation (7.20) for scattering from correlated impurities where the amplitude of the disorder potential is uniformly distributed in the asymmetric range $\delta[-1+\Delta, 1+\Delta]$ (notice that for a symmetric distribution the Gaussian correlator $\langle V^3 \rangle_{dis}$ appearing in the skew-scattering term automatically vanishes). However, we find that the product of the three overlaps $\langle u_{\boldsymbol{q}\nu''}|u_{\boldsymbol{k}\nu}\rangle\langle u_{\boldsymbol{k}\nu}|u_{\boldsymbol{k}'\nu'}\rangle\langle u_{\boldsymbol{k}'\nu'}|u_{\boldsymbol{q}\nu''}\rangle$ is strictly real for arbitrary momenta and band indices when the magnetic field is applied in the plane of the 2DES. Hence both the skew-scattering (7.13) and the side-jump (7.16) terms turn out to be zero for in-plane field.

Although here we computed the Pancharatnam-Berry phase numerically, it is easy to analytically show the same result but for the simpler case of the Rashba Hamiltonian. In momentum space, the Rashba Hamiltonian has a 2x2 matrix structure. Hence the relevant product of wavefunction overlaps, or more precisely, the argument of this quantity (the Pancharatnam-Berry phase) is equivalent to half the solid angle the Bloch states $u_{\boldsymbol{k}}$, $u_{\boldsymbol{k}'}$, and $u_{\boldsymbol{q}}$ span on the Bloch sphere. Since for an in-plane Zeeman term the Rashba Hamiltonian may be expanded solely in terms of the Pauli matrices $\hat{\sigma}_0$, $\hat{\sigma}_x$, and $\hat{\sigma}_y$, this solid angle vanishes identically. The same phenomenon leads to the vanishing of the side-jump.

If an out-of-plane magnetic field is switched on, all the contributions become finite, but we find them to remain small throughout our simulations. More explicitly, for the same choice of parameters of the calculations in the main text we observe numerically that both skew-scattering and side-jump contributions yield corrections less than 1% of the calculated total magnetoresistance resistance for out-of-plane fields up to 12 T and distributions as asymmetric as $\Delta = 0.5$. We do not show these results here as they are almost invisible on the scale of Fig. 7.8.

Bibliography

[1] D. S. L. Abergel, J. R. Wallbank, X. Chen, M. Mucha-Kruczyński, and V. I. Fal'ko, New J. Phys. **15**, 123009 (2013).

[2] A. R. Akhmerov, J. P. Dahlhaus, F. Hassler, M. Wimmer, and C. W. J. Beenakker, Phys. Rev. Lett. **106**, 057001 (2010).

[3] A. R. Akhmerov, J. P. Dahlhaus, F. Hassler, M. Wimmer, and C. W. J. Beenakker, Phys. Rev. Lett. **106**, 057001 (2011).

[4] A. Alexandradinata, C. Fang, M. J. Gilbert, and B. A. Bernevig, Phys. Rev. Lett. **113**, 116403 (2014).

[5] J. Alicea, Phys. Rev. B **81**, 125318 (2010).

[6] J. Alicea, Rep. Prog. Phys. **75**, 076501 (2012).

[7] A. Altland and M. R. Zirnbauer, Phys. Rev. B **55**, 1142 (1997).

[8] M. P. Anantram and S. Datta, Phys. Rev. B **53**, 16390 (1996).

[9] D. Asahi and N. Nagaosa, Phys. Rev. B **86**, 100504(R) (2012).

[10] P. Baireuther, J. M. Edge, I. C. Fulga, C. W. J. Beenakker, and J. Tworzydlo, Phys. Rev. B **89**, 035410 (2014).

[11] C. W. J. Beenakker, Rev. Mod. Phys. **80**, 1337 (2008).

[12] C. W. J. Beenakker, J. P. Dahlhaus, M. Wimmer, and A. R. Akhmerov, Phys. Rev. B **83**, 085413 (2011).

[13] C. W. J. Beenakker, Annu. Rev. Con. Mat. Phys. **4**, 113 (2013).

[14] W. A. Benalcazar, J. C. Y. Teo, and T. L. Hughes, Phys. Rev. B **89**, 224503 (2014).

[15] M. Ben Shalom, C. W. Tai, Y. Lereah, M. Sachs, E. Levy, D. Rakhmilevitch, A. Palevski, and Y. Dagan Phys. Rev. B **80**, 140403R (2009).

[16] B. Béri, Phys. Rev. B **79**, 245315 (2009).

[17] B. Béri, Phys. Rev. B **85**, 140501(R) (2012).

[18] J. A. Bert, B. Kalisky, C. Bell, M. Kim, Y. Hikita, H.-Y. Hwang, and K. A. Moler, Nat. Phys. **7**, 767 (2011).

[19] N. N. Bogoliubov, Sov. Physics JETP 7, 41 (1958).

[20] O. Bohigas, M.J. Giannoni, and C. Schmit, Phys. Rev. Lett. **52** (1984).

[21] G. Bräunlich, G. M. Graf, and G. Ortelli, Commun. Math. Phys. **295**, 243 (2010).

[22] A. Brinkman, M. Huijben, M. van Zalk, J. Huijben, U. Zeitler, J. C. Maan, W. G. van der Wiel, G. Rijnders, D. H. Blank, and H. Hilgenkamp, Nat. Mater. **6**, 493 (2007).

[23] P. W. Brouwer, A. Furusaki, I. A. Gruzberg, and C. Mudry, Phys. Rev. Lett. **85**, 1064 (2000).

[24] P. W. Brouwer, A. Furusaki, and C. Mudry, Phys. Rev. B **67**, 014530 (2003).

[25] P. W. Brouwer, A. Furusaki, C. Mudry, and S. Ryu, arXiv:cond-mat/0511622.

[26] D. Bucheli, M. Grilli, F. Peronaci, G. Seibold, and S. Caprara, Phys. Rev. B **89**, 195448 (2014).

[27] A. Bühler, N. Lang, C. V. Kraus, G. Möller, S. D. Huber, and H. P. Büchler, Nature Communications **5**, 4504 (2014).

[28] M. Büttiker, Phys. Rev. B **38**, 9375 (1988).

[29] C. Cancellieri, M. L. Reinle-Schmitt, M. Kobayashi, V. N. Strocov, and P. R. Willmott, D. Fontaine, Ph. Ghosez, A. Filippetti, P. Delugas, and V. Fiorentini, Phys. Rev. B **89**, 121412 (2014).

[30] S. Caprara, F. Peronaci, and M. Grilli, Phys. Rev. Lett. **109**, 196401 (2012).

[31] A. H. Castro Neto, F. Guinea, N. M. R. Peres, K. S. Novoselov, and A. K. Geim, Rev. Mod. Phys. **81**, 109 (2009).

[32] A. D. Caviglia, S. Gariglio, N. Reyren, D. Jaccard, T. Schneider, M. Gabay, S. Thiel, G. Hammerl, J. Mannhart, and J.-M. Triscone, Nature **456**, 624 (2008).

[33] A. D. Caviglia, M. Gabay, S. Gariglio, N. Reyren, C. Cancellieri, and J.-M. Triscone, Phys. Rev. Lett., **104**, 126803 (2010).

[34] V. V. Cheianov and V. I. Fal'ko, Phys. Rev. B, **74**, 041403 (2006).

[35] X. Chen, J. R. Wallbank, A. A. Patel, M. Mucha-Kruczyński, E. McCann, and V. I. Fal'ko, Phys. Rev. B **89**, 075401 (2014).

[36] M. Cheng, R. M. Lutchyn, V. Galitski, and S. Das Sarma, Phys. Rev. B **82**, 094504 (2010).

[37] C.-K. Chiu, H. Yao, and S. Ryu, Phys. Rev. B **88**, 075142 (2013).

[38] C.-K. Chiu and A. P. Schnyder, Phys. Rev. B **90**, 205136 (2014).

[39] T.-P. Choy, J. M. Edge, A. R. Akhmerov, and C. W. J. Beenakker, Phys. Rev. B **84**, 195442 (2011).

[40] S. B. Chung, X.-L. Qi, J. Maciejko, and S.-C. Zhang, Phys. Rev. B **83**, 100512(R) (2011).

[41] B. Collins and P. Śniady, Comm. Math. Phys. **264**, 773 (2006).

[42] J. P. Dahlhaus, M. Gibertini, and C. W. J. Beenakker, Phys. Rev. B **86**, 174520 (2012).

[43] A. Das, Y. Ronen, Y. Most, Y. Oreg, M. Heiblum, and H. Shtrikman, Nature Physics **8**, 887 (2012).

[44] P.-G. De Gennes, *Superconductivity of Metals and Alloys* (Benjamin, New York, 1966).

[45] C. R., Dean, L. Wang, P. Maher, C. Forsythe, F. Ghahari, Y. Gao, J. Katoch, M. Ishigami, P. Moon, M. Koshino, T. Taniguchi, K. Watanabe, K. L. Shepard, J. Hone, P. Kim, Nature **497**, 598 (2013).

[46] P. Delplace and G. Montambaux, Phys. Rev. B **82**, 035438 (2010).

[47] Deng, M. T., C. L. Yu, G. Y. Huang, M. Larsson, P. Caroff, and H. Q. Xu, Nano Lett. **12**, 6414 (2012).

[48] M. Diez, I. C. Fulga, D. I. Pikulin, J. Tworzydlo, and C. W. J. Beenakker, New J. Phys. **16**, 063049 (2014).

[49] E. Dumitrescu, T. D. Stanescu, and S. Tewari, Phys. Rev. B **91**, 121413(R) (2015).

[50] P. Dziawa, B. J. Kowalski, K. Dybko, R. Buczko, A. Szczerbakow, M. Szot, E. Lusakowska, T. Balasubramanian, B. M. Wojek, and M. H. Berntsen, Nat. Mater. **11**, 1023 (2012).

[51] F. Evers and A. D. Mirlin, Rev. Mod. Phys. **80**, 1355 (2008).

[52] A. Fête, S. Gariglio, A. D. Caviglia, J.-M. Triscone, and M. Gabay, Phys. Rev. B **86**, 201105R (2012).

[53] A. Fête, S. Gariglio, C. Berthod, D. Li, D. Stornaiuolo, M. Gabay, and J.-M. Triscone, New J. Phys. **16**, 112002 (2014).

[54] L. Fidkowski and A. Kitaev, Phys. Rev. B **81**, 134509 (2010); **83**, 075103 (2011).

[55] L. Fidkowski, R. M. Lutchyn, C. Nayak, and M. P. A. Fisher, Phys. Rev. B **84**, 195436 (2011).

[56] M. H. Fischer, S. Raghu, and E.-A. Kim, New J. Phys. **15**, 023022 (2013).

[57] E. Flekser, M. Ben Shalom, M. Kim, C. Bell, Y. Hikita, H. Y. Hwang, and Y. Dagan, Phys. Rev. B **86**, 121104R (2012).

[58] P. J. Forrester, *Log-Gases and Random Matrices* (Princeton University Press, 2010).

[59] L. Fu, C. Kane, and E. Mele, Phys. Rev. Lett. **98**, 106803 (2007).

[60] L. Fu and C. L. Kane, Phys. Rev. B **76**, 045302 (2007).

[61] L. Fu and C. L. Kane, Phys. Rev. Lett. **100**, 096407 (2008).

[62] L. Fu and C. L. Kane, Phys. Rev. B **79**, 161408(R) (2009).

[63] L. Fu, Phys. Rev. Lett. **106**, 106802 (2011).

[64] L. Fu and C. L. Kane, Phys. Rev. Lett. **109**, 246605 (2012).

[65] I. C. Fulga, F. Hassler, A. R. Akhmerov, and C. W. J. Beenakker, Phys. Rev. B **83**, 155429 (2011).

[66] I. C. Fulga, F. Hassler, and A. R. Akhmerov, Phys. Rev. B **85**, 165409 (2012).

[67] I. C. Fulga, A. R. Akhmerov, J. Tworzydlo, B. Béri, and C. W. J. Beenakker, Phys. Rev. B **86**, 054505 (2012).

[68] I. C. Fulga, B. van Heck, J. M. Edge, and A. R. Akhmerov, Phys. Rev. B **89**, 155424 (2014).

[69] F. Gerbier and J. Dalibard, New J. Phys. **12**, 033007 (2010).

[70] C. W. Groth, M. Wimmer, A. R. Akhmerov, and X. Waintal, New J. Phys. **16**, 063065 (2014).

[71] I. A. Gruzberg, N. Read, and S. Vishveshwara, Phys. Rev. B **71**, 245124 (2005).

[72] B. I. Halperin, Phys. Rev. B **25**, 2185 (1982).

[73] M. Z. Hasan and C. L. Kane, Rev. Mod. Phys. **82**, 3045 (2010).

[74] A. J. Heeger, S. Kivelson, J. R. Schrieffer, and W. P. Su, Rev. Mod. Phys. **60**, 781 (1988).

[75] D. R. Hofstadter, Phys. Rev. B **14**, 2239 (1976).

[76] J.-M. Hou, W.-X. Yang, and X.-J. Liu, Phys. Rev. A **79**, 043621 (2009).

[77] T. H. Hsieh, H. Lin, J. Liu, W. Duan, A. Bansi, and L. Fu, Nat. Commun. **3**, 982 (2012).

[78] B. Hunt, J. D. Sanchez-Yamagishi, A. F. Young, M. Yankowitz, B. J. LeRoy, K. Watanabe, T. Taniguchi, P. Moon, M. Koshino, P. Jarillo-Herrero, R. C. Ashoori, Science **340**, 1427 (2013).

[79] P. Jadaun, D. Xiao, Q. Niu, and S. K. Banerjee, Phys. Rev. B **88**, 085110 (2013).

[80] A. Joshua, S. Pecker, J. Ruhman, E. Altman, and S. Ilani, Nat. Commun. **3**, 1129 (2012).

[81] A. Joshua, J. Ruhman, S. Pecker, E. Altman, and S. Ilani, Proc. Nat. Acad. Sci. **110**, 9633 (2013).

[82] B. Kalisky, J. A. Bert, B. B. Klopfer, C. Bell, H. K. Sato, M. Hosoda, Y. Hikita, H.-Y. Hwang, and K. A. Moler, Nat. Commun. **3**, 922 (2012).

[83] C. Kallin, and A. J. Berlinsky, 164210 (2009).

[84] S. Kashiwaya and Y. Tanaka, Rep. Prog. Phys. **63**, 1641 (2000).

[85] M. I. Katsnelson, Eur. Phys. J. B **51**, 157 (2006).

[86] M. I. Katsnelson, K. S. Novoselov, and A. K. Geim, Nature Phys. **2**, 620 (2006).

[87] M. I. Katsnelson, *Graphene: Carbon in Two Dimensions* (Cambridge University Press, 2012).

[88] G. Kells, D. Meidan, and P. W. Brouwer, Phys. Rev. B **85**, 060507(R) (2012).

[89] M. Kindermann, B. Uchoa, and D. L. Miller, Phys. Rev. B **86**, 115415 (2012).

[90] A. Yu. Kitaev, Phys.-Usp. Suppl. **44**, 131 (2001).

[91] A. Kitaev, in: *Topological phases and quantum computations: Exact Methods in Low-Dimensional Statistical Physics and Quantum Computing*, edited by J. Jacobsen et al. (Oxford University Press, 2010); A. Kitaev and C. Laumann, arXiv:0904.2771.

[92] A. Kitaev, AIP Conf. Proc. **1134**, 22 (2009), Conference date: 22–26 June 2008, Chernogolokova (Russia); Also available as a e-print: arXiv:0901.2686.

[93] P. Krogstrup, N. L. B. Ziino, W. Chang, S. M. Albrecht, M. H. Madsen, E. Johnson, J. Nygård, C. M. Marcus, T. S. Jespersen, Nature Materials **14**, 400 (2015).

[94] K. T. Law, Patrick A. Lee, and T. K. Ng, Phys. Rev. Lett. **103**, 237001 (2009).

[95] L. Li, C. Richter, J. Mannhart, and R. C. Ashoori, Nat. Phys. **7**, 762 (2011).

[96] J. Li, G. Fleury, and M. Büttiker, Phys. Rev. B **85**, 125440 (2012).

[97] C.-X. Liu and B. Trauzettel, Phys. Rev. B **83**, 220510(R) (2011).

[98] R. M. Lutchyn, J. D. Sau, and S. Das Sarma, Phys. Rev. Lett. **105**, 077001 (2010).

[99] R. M. Lutchyn and M. P. A. Fisher, Phys. Rev. B **84**, 214528 (2011).

[100] A. P. Mackenzie, and Y. Maeno, Rev. Mod. Phys. **75**, 657 (2003).

[101] E. Majorana, Nuovo Cimento **5**, 171 (1937). [Soryushiron Kenkyu **63**, 149 (1981)].

[102] L. F. Mattheis, Phys. Rev. B, **6**, 4718 (1972).

[103] M. V. Medvedyeva, J. Tworzydło, and C. W. J. Beenakker, Phys. Rev. B **81**, 214203 (2010).

[104] R. S. K. Mong, A. M. Essin, and J. E. Moore, Phys. Rev. B **81**, 245209 (2010).

[105] R. S. K. Mong, J. H. Bardarson, and J. E. Moore, Phys. Rev. Lett. **108**, 076804 (2012).

[106] J. Moore and L. Balents, Phys. Rev. B **75**, 121306(R) (2007).

[107] T. Morimoto and A. Furusaki, Phys. Rev. B **88**, 125129 (2013).

[108] O. Motrunich, K. Damle, and D. Huse, Phys. Rev. B **63**, 224204 (2001).

[109] V. Mourik, K. Zuo, S. M. Frolov, S. R. Plissard, E. P. A. M. Bakkers, and L. P. Kouwenhoven, Science **336**, 1003 (2012).

[110] S. Nadj-Perge, I. K. Drozdov, B. A. Bernevig, and A. Yazdani, Phys. Rev. B **88**, 020407 (2013).

[111] S. Nadj-Perge, I. Drozdov, J. Li, H. Chen, S. Jeon, J. Seo, A. MacDonald, and B. B. A. Yazdani, Science **346**, 602 (2014).

[112] N. Nagaosa, J. Sinova, S. Onoda, A. H. MacDonald, and N. P. Ong, Rev. Mod. Phys. **82**, 1539 (2010).

[113] Y. Nakamura and Y. Yanase, J. Phys. Soc. Jpn. **82**, 083705 (2013).

[114] R. Nandkishore, L. Levitov, and A. Chubukov, Nature Phys. **8**, 158 (2012).

[115] Y. Niu, S.-B. Chung, C.-H. Hsu, I. Mandal, S. Raghu, and S. Chakravarty, Phys. Rev. B **85**, 035110 (2012).

[116] A. Ohtomo and H.-Y. Hwang, Nature **427**, 423 (2004).

[117] Y. Oreg, G. Refael, and F. von Oppen, Phys. Rev. Lett. **105**, 177002 (2010).

[118] C. Ortix, L. Yang, and J. van den Brink, Phys. Rev. B 86, 081405(R) (2012).

[119] D. Osadchy and J. E. Avron, J. Math. Phys. **42**, 5665 (2001).

[120] Y. Pang, J. Shen, J. Wang, J. Feng, F. Qu, Z. Lyu, J. Fan, G. Liu, Z. Ji, X. Jing, C. Yang, Q. Sun, X. C. Xie, L. Fu, L. Lu, arXiv:1503.00838 (2015).

[121] R. E. Peierls, Z. Phys. **80**, 763 (1933).

[122] D. I. Pikulin, C.-Y. Hou, and C. W. J. Beenakker, Phys. Rev. B **84**, 035133 (2011).

[123] N. C. Plumb, and M. Salluzzo, E. Razzoli, M. Månsson, M. Falub, J. Krempasky, C. E. Matt, J. Chang, M. Schulte, J. Braun, H. Ebert, J. Minár, B. Delley, K.-J. Zhou, T. Schmitt, M. Shi, J. Mesot, L. Patthey, and M. Radović, Phys. Rev. Lett. **113**, 086801 (2014).

[124] L. A. Ponomarenko, R. V. Gorbachev, G. L. Yu, D. C. Elias, R. Jalil, A. A. Patel, A. Mishchenko, A. S. Mayorov, C. R. Woods, J.

R. Wallbank, M. Mucha-Kruczynski, B. A. Piot, M. Potemski, I. V. Grigorieva, K. S. Novoselov, F. Guinea, V. I. Fal'ko, and A. K. Geim, Nature **497**, 594 (2013).

[125] A. C. Potter and P. A. Lee, Phys. Rev. B **85**, 094516 (2012).

[126] X.-L. Qi, T. L. Hughes, S. Raghu, and S.-C. Zhang, Phys. Rev. Lett. **102**, 187001 (2009).

[127] X.-L. Qi and S.-C. Zhang, Rev. Mod. Phys. **83**, 1057 (2011).

[128] R. Rammal, J. Physique **46**, 1345 (1985).

[129] Y. Ran, arXiv:1006.5454 (2010).

[130] N. Read and D. Green, Phys. Rev. B **61**, 10267 (2000).

[131] N. Reyren, S. Thiel, A. D. Caviglia, L. F. Kourkoutis, G. Hammerl, C. Richter, C. W. Schneider, T. Kopp, A.-S. Rüetschi, D. Jaccard, M. Gabay, D. A. Muller, and J.-M. Triscone, Science **317**, 1196 (2007).

[132] N. Reyren, S. Thiel, A. D. Caviglia, L. Fitting Kourkoutis, G. Hammerl, C. Richter, C. W. Schneider, T. Kopp, A.-S. Rüetschi, D. Jaccard, M. Gabay, D. A. Muller, J.-M. Triscone, and J. Mannhart, Science **317**, 1196 (2007).

[133] J.-W. Rhim and K. Park, Phys. Rev. B **86**, 235411 (2012).

[134] M.-T. Rieder, G. Kells, M. Duckheim, D. Meidan and P. W. Brouwer, Phys. Rev. B **86**, 125423 (2012).

[135] Z. Ringel, Y. E. Kraus, and A. Stern, Phys. Rev. B **86**, 045102 (2012).

[136] R. Roy, Phys. Rev. B **79**, 195322 (2009).

[137] J. Ruhman, A. Joshua, S. Ilani, and E. Altman, Phys. Rev. B **90**, 125123 (2014).

[138] S. Ryu, A. Schnyder, A. Furusaki, and A. Ludwig, New J. Phys. **12**, 065010 (2010).

[139] B. Sacépé, J. B. Oostinga, J. Li, A. Ubaldini, N. J. G. Couto, E. Giannini, and A. F. Morpurgo, Nature Comm. **2**, 575 (2011).

[140] B. Sachs, T. O. Wehling, M. I. Katsnelson, and A. I. Lichtenstein, Phys. Rev. B **84**, 195414 (2011).

[141] M. Salluzzo, J. C. Cezar, N. B. Brookes, V. Bisogni, G. M. De Luca, C. Richter, S. Thiel, J. Mannhart, M. Huijben, A. Brinkman, G. Rijnders, and G. Ghiringhelli, Phys. Rev. Lett. **102**, 166804 (2009).

[142] A. F. Santander-Syro, O. Copie, T. Kondo, F. Fortuna, S. Pailheś, R. Weht, X. G. Qiu, F. Bertran, A. Nicolaou, A. Taleb-Ibrahimi, P. Le Fevŕe, G. Herranz, M. Bibes, N. Reyren, Y. Apertet, P. Lecoeur, A. Barthélémy, and M. J. Rozenberg, Nature **469**, 189 (2011).

[143] M. Sato and S. Fujimoto, Phys. Rev. B **79**, 094504 (2009).

[144] K. V. Shanavas, Z. S. Popović, and S. Satpathy, Phys. Rev. B, **90**, 165108 (2014).

[145] J. D. Sau, R. M. Lutchyn, S. Tewari, and S. Das Sarma, Phys. Rev. Lett. **104**, 040502 (2010).

[146] D. V. Savin and H.-J. Sommers, Phys. Rev B **73**, 081307(R) (2006). We make use of the Selberg integral formulas in Eqs. (6) and (7) of this reference, where $n = M$, $b = |Q|+1$, $c = 1$, and $a-1/2 = N-|Q|$ mod 2.

[147] M. Scheid, I. Adagideli, J. Nitta, and K. Richter, Semicond. Sci. Technol. **24**, 064005 (2009).

[148] A. P. Schnyder, S. Ryu, A. Furusaki and A. W. W. Ludwig, AIP Conf. Proc. 1134, 10 (2009), Conference date: 22–26 June 2008, Chernogolokova (Russia); Also available as a e-print: arXiv:0905.2029.

[149] T. Senthil, J. B. Marston, and M. P. A. Fisher, Phys. Rev. B **60**, 4245 (1999).

[150] T. Senthil and M. P. A. Fisher, Phys. Rev. B **61**, 9690 (2000).

[151] I. Serban, B. Béri, A. R. Akhmerov, and C. W. J. Beenakker, Phys. Rev. Lett. **104**, 147001 (2010).

[152] I. Seroussi, E. Berg, and Y. Oreg, Phys. Rev. B **89**, 104523 (2014).

[153] M. Ben Shalom, M. Sachs, D. Rakhmilevitch, A. Palevski, and Y. Dagan, Phys. Rev. Lett. **104**, 126802 (2010).

[154] M. A. Shifman, Physics Reports **209**, 341 (1991).

[155] E. V. Shuryak, Verbaarschot J. J. M., Nucl. Phys. A **560**, 306 (1993)

[156] N. A. Sinitsyn, Q. Niu, and A. H. MacDonald, Phys. Rev B **73**, 075318 (2006).

[157] R.-J. Slager, A. Mesaros, V. Juričić, and J. Zaanen, Nat. Phys. **9**, 98 (2012).

[158] M. Stone and R. Roy, Phys. Rev. B **69**, 184511 (2004).

[159] G. Strübi, W. Belzig, M.-S. Choi, and C. Bruder, Phys. Rev. Lett. **107**, 136403 (2011)

[160] H. Sumiyoshi and S. Fujimoto, J. Phys. Soc. Jpn. **82**, 023602 (2013).

[161] Y. Tanaka, T. Yokoyama, A. V. Balatsky, and N. Nagaosa, Phys. Rev. B **79**, 060505 (2009).

[162] Y. Tanaka, Z. Ren, T. Sato, K. Nakayama, S. Souma, T. Takahashi, K. Segawa, and Y. Ando, Nat. Phys. **8**, 800 (2012).

[163] J. C. Y. Teo and C. L. Kane, Phys. Rev. B **82**, 115120 (2010).

[164] J. C. Y. Teo and T. L. Hughes, Phys. Rev. Lett. **111**, 047006 (2013).

[165] S. Tewari, T. D. Stanescu, J. D. Sau, and S. Das Sarma, Phys. Rev. B. **86**, 024504 (2012).

[166] S. Tewari and J. D. Sau, Phys. Rev. Lett. **109**, 150408 (2012).

[167] S. Thiel, G. Hammerl, A. Schmehl, C. W. Schneider, J. Mannhart, Science **313**, 1942 (2006).

[168] S. Thiel, C. W. Schneider, L. Fitting Kourkoutis, D. A. Muller, N. Reyren, A. D. Caviglia, S. Gariglio, J.-M. Triscone, and J. Mannhart, Phys. Rev. Lett. **102**, 046809 (2009).

[169] D. J. Thouless, M. Kohmoto, M. P. Nightingale, and M. den Nijs, Phys. Rev. Lett. **49**, 405 (1982).

[170] M. Trushin, K. Výborný, P. Moraczewski, A. A. Kovalev, J. Schliemann, and T. Jungwirth Phys. Rev. B **80**, 134405 (2009).

[171] J. Tworzydło, B. Trauzettel, M. Titov, A. Rycerz, and C. W. J. Beenakker, Phys. Rev. Lett. **96**, 246802 (2006).

[172] O. Vafek, A. Melikyan, M. Franz, and Z. Tešanović, Phys. Rev. B **63**, 134509 (2001).

[173] L. W. van Heeringen, G. A. de Wijs, A. McCollam, J. C. Maan, and A. Fasolino, Phys. Rev. B **88**, 205140 (2013).

[174] M. Veldhorst, M. Snelder, M. Hoek, T. Gang, X. L. Wang, V. K. Guduru, U. Zeitler, W. G. van der Wiel, A. A. Golubov, H. Hilgenkamp, and A. Brinkman, Nature Mat. **11**, 417 (2012).

[175] J. J. M. Verbaarschot, Phys. Rev. Lett. **72**, 2531 (1994).

[176] J. J. M. Verbaarschot and T. Wettig, Ann. Rev. Nucl. Part. Sci. **50**, 343 (2000).

[177] G. E. Volovik, JETP Lett. **66**, 522 (1997).

[178] R. Wakatsuki, M. Ezawa, and N. Nagaosa, Phys. Rev. B **89**, 174514 (2014).

[179] J. R. Wallbank, A. A. Patel„ M. Mucha-Kruczyński, A. K. Geim, and V. I. Fal'ko, Phys. Rev. B **87**, 245408 (2013).

[180] X. Wang, W. M. Lü, A. Annadi, Z. Q. Liu, K. Gopinadhan, S. Dhar, T. Venkatesan, and Ariando, Phys. Rev. B **84**, 075312 (2011).

[181] D. Wang, Z. Huang, and C. Wu, Phys. Rev. B **89**, 174510 (2014).

[182] X.-G. Wen, Phys. Rev. B **85**, 085103 (2012).

[183] B. J. Wieder, F. Zhang, and C. L. Kane, Phys. Rev. B 89, 075106 (2014).

[184] J. R. Williams, A. J. Bestwick, P. Gallagher, S. S. Hong, Y. Cui, A. S. Bleich, J. G. Analytis, I. R. Fisher, and D. Goldhaber-Gordon, Phys. Rev. Lett. **109**, 056803 (2012).

[185] M. Wimmer and K. Richter, J. Comp. Phys. **228**, 8548 (2009).

[186] M. Wimmer, A. R. Akhmerov, J. P. Dahlhaus, and C. W. J. Beenakker, New J. Phys. **13**, 053016 (2011).

[187] C. R. Woods, L. Britnell, A. Eckmann, G. L. Yu, R. V. Gorbachev, A. V. Kretinin, J. Park, L. A. Ponomarenko, M. I. Katsnelson, Yu. N. Gornostyrev, K. Watanabe, T. Taniguchi, C. Casiraghi, A. K. Geim, and K. S. Novoselov, Nature Physics **10**, 451 (2014).

[188] S.-Y. Xu, C. Liu, N. Alidoust, M. Neupane, D. Qian, I. Belopolski, J. Denlinger, Y. Wang, H. Lin, and L. Wray, Nat. Commun. **3**, 1192 (2012).

[189] M. Yankowitz, J. Xue, D. Cormode, J. D. Sanchez-Yamagishi, K. Watanabe, T. Taniguchi, P. Jarillo-Herrero, P. Jacquod, and B. J. LeRoy, Nature Phys. **8**, 382 (2012).

[190] A. F. Young and P. Kim, Nature Physics **5**, 222 (2009).

[191] F. Zhang, C. L. Kane, and E. J. Mele, Phys. Rev. Lett. **111**, 056403 (2013).

[192] Z. Zhong, A. Tóth, and K. Held, Phys. Rev. B **87**, 161102 (2013).

[193] J. M. Ziman, Phys. Rev. Lett. **121**, 1320 (1961).

[194] J. M. Ziman, *Principles of the Theory of Solids* (Cambridge University Press, Cambridge, 1972).

[195] M. R. Zirnbauer, Physik Journal 11 **9**, 41 (2012).

Samenvatting

Topologische supergeleiders vormen een nieuw soort supergeleiders met Majorana deeltjes aan het oppervlak. Deze deeltjes zijn in een superpositie van elektron en gat, en dus hun eigen anti-deeltje. Er is grote belangstelling voor deze bijzondere deeltjes, zowel van theoretische als van experimentele zijde. De eerste experimentele waarnemingen ondersteunen de theoretische voorspellingen, maar er is nog geen onomstotelijk bewijs voor de Majorana deeltjes gevonden.

Een deel van de experimentele moeilijkheid is dat de Majorana deeltjes, omdat ze elektrisch neutraal zijn, niet eenvoudig via elektrische metingen kunnen worden opgespoord. Theoretisch volgt het bestaan van de Majorana deeltjes uit topologische overwegingen, die volledig gebaseerd zijn op de ruimtelijke dimensionaliteit en op de aanwezigheid van bepaalde symmetrieën. Hierdoor zijn de oppervlaktetoestanden immuun voor wanorde en allerlei onzuiverheden, hetgeen de experimenten zou moeten vereenvoudigen. Majoranadeeltjes kunnen warmte geleiden, maar bij lage temperaturen is het heel lastig om warmtegeleiding nauwkeurig te meten. Een elektrische detectiemethode heeft dan ook sterk de voorkeur. In dit proefschrift onderzoeken we of elektrische detectie mogelijk is, ondanks het feit dat de Majoranadeeltjes zelf elektrisch neutraal zijn. We maken gebruik van verstrooiingstheorie en van toevalsmatrixtheorie om algemene principes uit te werken, die we vervolgens testen met computersimulaties van realistische systemen.

Als de topologische supergeleider de vorm heeft van een draad, dan bevinden de Majoranadeeltjes zich aan de beide uiteinden. Zij veroorzaken een piek van de elektrische geleiding rond spanning nul. De hoogte van die piek is $2e^2/h$ bij lage temperaturen. Men zou kunnen vermoeden dat twee of meer Majoranadeeltjes aan het uiteinde van de draad voor een grotere piekgeleiding zou zorgen, maar in het meest algemene geval stoten Majoranadeeltjes elkaar af en is alleen één enkele Majorana stabiel.

Een grotere piek is mogelijk als er een zogenaamde chirale symmetrie optreedt, die de afstoting van de Majoranadeeltjes onderdrukt. In hoofdstuk twee onderzoeken wij het effect van de chirale symmetrie op het geleidingsvermogen. We leiden een ondergrens af voor de geleidingspiek, die het mogelijk maakt om het aantal Majoranadeeltjes te bepalen. De chirale symmetrie is slechts bij benadering geldig, daarom doen wij computersimulaties aan een realistisch systeem. We concluderen dat deze symmetrie van kracht zou moeten zijn in de bestaande experimenten.

Een draad is een één-dimensionale supergeleider. We vervolgen het proefschrift met het bestuderen van twee-dimensionale topologische supergeleiders. De Majoranadeeltjes bewegen dan langs de rand, hetzij in één enkele richting, hetzij in beide richtingen. In hoofdstuk drie stellen we een experiment voor, gebruikmakend van een schijfgeometrie (Corbinoschijf), waarin het mogelijk is zowel de randtoestanden te detecteren als de bewegingsrichting te meten. We maken hiervoor gebruik van oscillaties van het geleidingsvermogen, gemeten aan de binnen- en buitenrand van de schijf.

De volgende twee hoofdstukken zijn een uitbreiding van onze analyse naar een nieuwe klasse van topologische supergeleiders, zogenaamde “statistische” topologische supergeleiders. Dit betreft materialen waar de symmetrie lokaal gebroken is, maar gemiddeld genomen (statistisch) over grote afstanden nog steeds geldt. Een voorbeeld is een sterk anisotrope topologische supergeleider, gevormd door een groot aantal parallelle draden. De Majoranadeeltjes aan de uiteinden vormen dan een randtoestand die beide richtingen op kan bewegen. Wanorde heeft wel een effect op de beweging, maar kan die niet volledig onderdrukken. (Er treedt geen lokalisatie op.) Zo’n randtoestand noemen we een *Kitaev randtoestand*, omdat het een variatie is op een ouder idee van Alexey Kitaev. We laten zien dat deze randtoestand weliswaar gemiddeld genomen geen elektrische stroom geleidt, maar dat er toch tijdsafhankelijke fluctuaties zijn in de stroom, die als hagelruis gedetecteerd kunnen worden. De Kitaev randtoestand kan ook midden in het materiaal optreden, bij een domeinwand, zoals we in hoofdstuk vijf laten zien.

In de laatste twee hoofdstukken verlaten we het centrale thema van de topologische supergeleiders. We laten ons motiveren door enkele recente experimentele doorbraken. In hoofdstuk zes onderzoeken we het effect van een sterk magneetveld op grafeen (een koolstof monolaag), als dit magneetveld gecombineerd wordt met een periodiek elektrisch veld. Er treedt dan in de bandstructuur een patroon op dat iets weg heeft van een vlinder, en naar de ontdekker de Hofstadtervlinder genoemd wordt. In hoofdstuk zeven brengen we verslag uit van een samenwerking met de experimentele groep in Delft, waar de twee-dimensionale beweging van elektronen is onderzocht in een grenslaag tussen twee oxides ($LaAlO_3$ en $SrTiO_3$). Het elektrische geleidingsvermogen is sterk afhankelijk van een parallel aangebracht magnetisch veld, hetgeen wij met een semiklassieke transporttheorie kunnen verklaren.

Summary

Topological superconductors are a novel type of superconductors that carry Majorana particles at their boundary. These surface states are equal superpositions of electrons and holes, and hence are their own anti-particles. There has been a recent surge of theoretical and experimental effort to realize these special particles in the lab. While first observations support the theoretical predictions, fail-safe experimental evidence for Majoranas is still needed.

Part of the challenge is that due to their vanishing charge they are not easily detected electrically. According to theory their existence (which can be proved on topological grounds) only relies on the systems dimensionality and the presence of a few fundamental symmetries. This makes these particular surface states immune to microscopic imperfections like disorder. As a result of this protection one expects equally robust transport signatures. Majorana states can carry heat, but this is very difficult to measure accurately at low temperatures. For this reason electrical probes are much favored. In this thesis we propose and study electrical signatures of Majoranas that are present in spite of their charge neutrality. By applying scattering and random matrix theory we first examine their generic properties. With the tool of numerical simulations we then put our predictions to test on realistic systems.

If the topological superconductor has the form of a wire, a Majorana particle can be found at each end. Its presence causes a peak of the electrical conductance around zero voltage. At low temperatures this peak has a universal height of $2e^2/h$. One may expect a higher conductance peak if there are multiple Majoranas at the wire end. Generically, however, this cannot happen because multiple Majoranas repel each other and only single Majorana end states are stable. The symmetry that suppresses this repulsion is called chiral symmetry. In chapter two we investigate the effect of chiral symmetry on the wire's conductance. We derive a lower bound

for the electrical conductance that allows one to determine the number of Majorana end states. In reality the chiral symmetry is only approximate, which is why we perform a numerical test on a realistic model. We find that the symmetry still holds in current experiments.

Wires are one dimensional. The thesis continues with a study of two dimensional topological superconductors. Here, the Majorana particles move along the edge of the system, either only in one or (protected by time-reversal symmetry) in both directions. In chapter three we propose an experiment with the geometry of a Corbino-disk, for which it is possible to detect and distinguish the two modes of movement. For this purpose we use oscillations of the electrical conductance that can be observed at the inner and outer edge of the disk.

In the following two chapters we extend our analysis to, so called, *statistical* topological superconductors. This extension is concerned with cases where some symmetries are broken locally but still exist in an average sense over long length scales. An example is a stack of superconducting wires that naturally experiences a strong anisotropy along vs across the direction of the wires. Majorana particles can move in both directions along the coupled wire ends. Disorder hinders their movement but it cannot completely suppress it. (The edge states avoid what is called localization.) In analogy to an earlier idea by Alexey Kitaev we refer to such edge states as *Kitaev edge states*. Although the edge states are again charge neutral we show that a measurement of time-dependent charge fluctuations can detect them in the electrical shot noise. As we show in the fifth chapter, Kitaev edge states also appear along domain walls in the middle of a topological superconductor.

The last two chapters of this thesis step out of the context of topological superconductivity. Instead these chapters are motivated by recent experimental advances in two fields. In chapter six we study the effect of large magnetic fields on electrons in graphene (a single atomic layer of graphite) when the material is also subject to a periodic electrical field. One finds an electronic band structure reminiscent of a butterfly that after its discoverer is named Hofstadter's butterfly. In the seventh chapter we present results of a collaboration with an experimental group in Delft, where we investigate electrons at the interface between two oxides ($LaAlO_3$ and $SrTiO_3$). The electrical resistance of this system strongly decreases when a magnetic field is applied parallel to the interface. Using semiclassical transport theory we are able to explain this behavior.

Curriculum Vitæ

I was born in Karlsruhe, Germany, on November 28th 1985. After moving to Pliezhausen, a small village near Reutlingen, I attended primary school there. My secondary education I received first at the Gymnasium Bildungszentrum Nord (1996-2000) and then at the Isolode-Kurz-Gymnasium (2000-2005), both in Reutlingen.

After graduating in 2005 I completed nine months of civilian service at the agency for conservation of nature in Reutlingen. In Fall 2006 I started studying physics at the University of Constance. During the course of my studies – from September 2009 to March 2010 – I spent a research internship at the University of Southern California in Los Angeles where I published my first scientific paper in the group of Prof. Dr. Stephan Haas. In Constance I wrote my diploma thesis on “Spin relaxation of mobile electrons in graphene” under the guidance of Prof. Dr. Guido Burkhard.

After my graduation I continued research in condensed matter physics by joining the group of Prof. Dr. Carlo Beenakker in Leiden. I became a PhD student at the Instituut Lorentz, where I was employed by the Foundation for Fundamental Research on Matter (FOM). My work here benefited very much from the unusually open and interactive atmosphere as well as from the close collaboration between the Leiden Institute of Physics and the Kavli Institute of Nanoscience in Delft.

During my time as a PhD student I was a teaching assistant in electrodynamics. I attended many schools, workshops, and conferences. I presented my work in the Netherlands, Germany, France, Denmark, the United States, and Israel.

List of Publications

1. *Local quenches in frustrated quantum spin chains: global vs. subsystem equilibration*, M. Diez, N. Chancellor, S. Haas, L. C. Venuti, P. Zanardi, Phys. Rev. A **82**, 032113 (2010).

2. *Bias-dependent D'yakonov-Perel' spin relaxation in bilayer graphene*, M. Diez, G. Burkard, Phys. Rev. B **85**, 195412 (2012).

3. *Andreev reflection from a topological superconductor with chiral symmetry*, M. Diez, J. P. Dahlhaus, M. Wimmer, C. W. J. Beenakker, Phys. Rev. B **86**, 094501 (2012). [Chapter 2]

4. *Phase-locked magnetoconductance oscillations as a probe of Majorana edge states*, M. Diez, I. C. Fulga, D. I. Pikulin, M. Wimmer, A. R. Akhmerov, C. W. J. Beenakker, Phys. Rev. B **87**, 125406 (2013), Editors' Suggestion. [Chapter 3]

5. *Emergence of massless Dirac fermions in graphene's Hofstadter butterfly at switches of the quantum Hall phase connectivity*, M. Diez, J. P. Dahlhaus, M. Wimmer, C. W. J. Beenakker, Phys. Rev. Lett. **112**, 196602 (2014). [Chapter 6]

6. *Bimodal conductance distribution of Kitaev edge modes in topological superconductors*, M. Diez, I. C. Fulga, D. I. Pikulin, J. Tworzydło, C. W. J. Beenakker, New J. Phys. **16**, 063049 (2014). [Chapter 4]

7. *Extended topological group structure due to average reflection symmetry*, M. Diez, D. I. Pikulin, I. C. Fulga, J. Tworzydło, New J. Phys. **17**, 043014 (2015). [Chapter 5]

8. *Giant negative magnetoresistance driven by spin-orbit coupling at the LAO/STO interface*, M. Diez, A.M.R.V.L. Monteiro, G. Mattoni, E. Cobanera, T. Hyart, E. Mulazimoglu, N. Bovenzi, C.W.J.

Beenakker, A.D. Caviglia, Phys. Rev. Lett. **115**, 016803 (2015). [Chapter 7]

9. *Ballistic Josephson junctions in edge-contacted graphene*, V. E. Calado, S. Goswami, G. Nanda, M. Diez, A. R. Akhmerov, K. Watanabe, T. Taniguchi, T. M. Klapwijk, L. M. K. Vandersypen, arXiv:-1501.06817.

10. *Topologically protected charge transfer along the edge of a chiral p-wave superconductor*, N. V. Gnezdilov, B. van Heck, M. Diez, Jimmy A. Hutasoit, C. W. J. Beenakker, arXiv:1505.06744.

Stellingen

behorende bij het proefschrift
On electronic signatures of topological superconductivity

1. Sufficiently narrow superconducting wires can support more than a single Majorana bound state at each end.
   Chapter 2

2. If the pair potential of a superconductor depends on the momentum, then for p-wave pairing this is the *canonical* momentum while for d-wave pairing it is the *covariant* momentum.
   Chapter 3

3. Massless chiral Dirac fermions can exist at 40 Tesla.
   Chapter 6

4. The giant magnetoresistance at the lanthanum aluminate/strontium titanate interface has a single-electron explanation.
   Chapter 7

5. To observe the chiral magnetic effect of a Weyl semimetal in a *finite* system one should periodically break inversion symmetry rather than oscillate the magnetic field, as in Chen's study of an *infinite* system.
   Y. Chen et al., Phys. Rev. B **88**, 125105 (2013).

6. The quantized electrical shot noise of a single Majorana edge mode in a chiral p-wave superconductor found by Gnezdilov et al. does not survive in the presence of multiple edge modes.
   N. V. Gnezdilov et al., arXiv:1505.06744.

7. The peak of a Majorana zero mode in the differential conductance, measured by a *superconducting* tunneling probe, should be at voltage V equal to the gap, instead of at $V = 0$ as reported by Pawlak et al.
   R. Pawlak et al., arXiv:1505.06078.

8. If one of the superconductors in the device of Tarasinski et al. is biased at a small voltage, the DC conductance to ground via a single-mode point contact is quantized in units of $2e^2/h$.
   B. Tarasinski et al., arXiv:1503.04207.

9. Topological insulators are the opposite of a "kroket". Both have surface states of a topological origin, but for the topological insulator it is the surface rather than the bulk that is compressible.

Mathias Diez
8 september 2015